

**SOLID STATE NMR CHARACTERIZATION OF CONDUCTIVE POLYANILINES**

---

**A dissertation**

**Presented to**

**The Faculty of the Applied Science Department**

**The College of William and Mary in Virginia**

**In Partial Fulfillment**

**Of the Requirements for the Degree of**

**Doctor of Philosophy**

---

**by**

**Yanina Anatolievna Goddard**

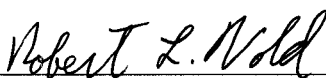
**2004**

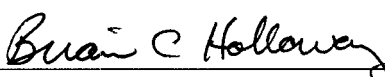
APPROVAL SHEET


This dissertation is submitted in partial fulfillment of  
the requirements for the degree of  
Doctor of Philosophy

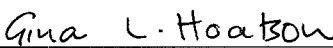
  
\_\_\_\_\_  
Yanina Anatolievna Goddard


Approved by the Committee, March 2004

  
\_\_\_\_\_  
Robert L. Vold, Chair

  
\_\_\_\_\_  
Brian C. Holloway

  
\_\_\_\_\_  
Dennis M. Manos

  
\_\_\_\_\_  
Gina L. Hoatson  
Department of Physics

  
\_\_\_\_\_  
Robert A. Orwoll  
Chemistry Department

To the memory of my grandparents, Zinaida, Vladimir, Tatyana and Sergey

## TABLE OF CONTENTS

	Page
Acknowledgements	vii
List of Tables	viii
List of Figures	ix
Abstract	xiii
Chapter 1. Conductive Polymers	2
1.1 Conductive Polyaniline	3
1.2 Experimental and Theoretical Studies	9
1.3 Clay Nanocomposites	15
Chapter 2. NMR and Conductive Polymers	17
2.1 NMR Background	18
2.1.1 Spin Angular Momentum and Basic Theory of NMR	18
2.1.2 Equation of Motion	20
2.2 Important Interactions	22
2.2.1 Zeeman Interaction	24
2.2.2 Quadrupole Interaction	25
2.2.3 Magnetic Dipolar Interaction	29
2.2.4 Hyperfine Interaction	31
a) Chemical Shielding Interaction	31
b) Electron-Nucleus Spin Interaction	33
2.3 Motion and Relaxation	39
2.3.1 Motion	39

2.3.2	Magic Angle Spinning	45
2.3.3	Relaxation	48
	a) Spin-lattice relaxation	48
	b) Transverse relaxation	50
	c) Redfield theory: a microscopic theory of $T_1$ and $T_2$	50
	d) Characteristic relaxation times for deuteron NMR	52
	e) Relaxation of nuclei in metals	54
2.4	Polarons and Bipolarons	57
Chapter 3.	Experimental Methods	61
3.1	Material Preparation	61
3.2	Material Characterization	65
3.3	NMR Experiments	68
	3.3.1 NMR Spectrometer and Probe	70
	3.3.2 NMR Data Manipulation	76
	3.3.3 Pulse Sequences and Experimental Techniques	78
Chapter 4.	Quadrupole Echo Lineshapes	88
4.1	Experimental Results	88
4.2	Fast 180° jumps	92
4.3	Cone Libration	93
4.4	Libration on an Arc	94
4.5	EXPRESS Lineshape Simulations	96
Chapter 5.	Magic Angle Spinning Experiments	105
5.1	Emeraldine Base	106

5.2	Emeraldine Salts	109
5.2.1	Spin Count Experiments	109
5.2.2	MAS of the Conductive Salts	114
5.3	Pani/Clay Inclusion Compound	126
Chapter 6.	Deuteron Relaxation Time Anisotropy of Polyanilines	129
6.1	Experimental Data	129
6.2	Emeraldine Base Relaxation	132
6.3	Emeraldine Hydrochloride Relaxation	143
Chapter 7.	Conclusions	150
Appendix A.	MAS Line shape Fitting Procedure	154
Appendix B.	$T_2$ Correction for Emeraldine Hydrochloride	158
Appendix C.	Derivation of Cartesian EFG Tensor Dependence on Fast $180^\circ$ Jump Motion	161
	Bibliography	163
	Vita	170

## ACKNOWLEDGEMENTS

I would like to take this opportunity to thank people without whom this work would never have been accomplished.

I am grateful to my dad, Anatoly, for making me love science and to my mom, Alla, for her endless energy and enthusiasm. Thank you for making me study English and pushing me to accomplish more than I thought I could. I am thankful to my husband, Michael, for his encouragement, support, care, friendship and for loaning me his copy of Jackson. I would like to thank my little brother, Vladimir, for making my character stronger. I thank little Anastasiya for making my life brigrter.

Though I will never be able to thank them enough, I will attempt to express my immense gratitude to my advisors, Dr. Vold and Dr. Hoatson. Thank you for sharing your knowledge and experience, for your brilliant ideas without which this work would have gone nowhere, for your patience, encouragement, and especially for your kindness in non-physics related matters (like baby showers). I would like to thank Dr. Klavetter for introducing me to the realm of chemistry. I am grateful to Dr. Orwoll for all the help in the chemistry lab. I appreciate the time all committee members (Dr. Vold, Dr. Hoatson, Dr. Orwoll, Dr. Manos and Dr. Holloway) spent reading this document.

I am forever in debt to my friend, the brilliant scientist Dasha Malyarenko. Thank you for helping me settle in Williamsburg, for helping me in lab and showing me basics of computer-handling, for putting up with me all these years, and for your guidance and care. I am grateful to Donghua for being friendly, always available and eager to help especially with those huge liquid nitrogen cylinders without which no low temperature experiments could have been done. And thank you, Bill Brouwer, for taking over responsibilities in the lab and for your friendship.

I thank all support staff: Amy Wilkerson, Karen Berquist, Patricia Van Zandt, Kirk Jacobs, John Bensel, Marcy Borges, Carol Davanay, and especially Sylvia Stout, for their help.

I would like to acknowledge Dr. Espe for the preparation of conductive samples and for valuable discussions.

## LIST OF TABLES

Table		Page
4.1	Best fit parameters for 180° flips of phenyl rings in polyanilines	98
4.2	Best fit parameters for four-site cone model of rigid component of polyanilines	102
5.1	Bulk conductivity, Crystallinity and <sup>2</sup> H Spin Counts	110
5.2	Best fit parameters for temperature dependent <sup>2</sup> H MAS spectra of emeraldine hydrochloride	116
5.3	Best fit parameters of a spinning sideband of ES/CSA/m-cresol, measured using 17.6 and 7 T magnetic fields	118
5.4	Best fit parameters for temperature dependent <sup>2</sup> H MAS spectra of Pani/Clay	127
A.1	Chi-square comparison of different model functions for emeraldine base, emeraldine salt and Pani/MMT Clay nanocomposite at 223K	157

## LIST OF FIGURES

Figure	Page
1.1. Schematic representation of polyaniline base	4
1.2. Schematic representation of emeraldine hydrochloride	5
2.1. Deuteron energy levels and powder pattern	28
2.2. Motional timescales associated with different phenomena	40
2.2. Illustration of a molecular ionization process energies	58
3.1 Schematic illustration of emeraldine salt synthesis	62
3.2 Schematic illustration of obtaining emeraldine base	62
3.3 Schematic illustration of Polyaniline / Clay synthesis	64
3.4 XRD data for aniline and polyaniline intercalated into MMT clay layers	65
3.5 FTIR measurements of clay and Pani/clay	67
3.6 Block diagram of the NMR spectrometer	71
3.7 Quadrupole echo pulse sequence	80
3.8 Presaturation quadrupole echo sequence	81
3.9 Paramagnetic quadrupole echo sequence	82
3.10 Inversion recovery quadrupole echo sequence	83
3.11 Broadband Jeener – Broekaert (BBJB) pulse sequence	85
3.12 Single pulse magic angle spinning experiment.	86
3.13 Inversion recovery magic angle spinning experiment	87
4.1. $^2\text{H}$ quadrupole echo and spectra presaturation spectra of ring-deuterated emeraldine base and salt at $T = 273$ and $333$ K	89

4.2.	Schematic illustration of a part of polyaniline molecule	92
4.3.	Oriental sites for the simulation of motion in a cone	94
4.4.	Presaturation powder pattern of deuterated emeraldine base at ambient temperature	97
4.5	Comparison of experimental QE spectrum of emeraldine base with EXPRESS simulations for four-site cone model	100
4.6	Comparison of experimental QE spectrum of emeraldine base with EXPRESS simulations for two frame arc libration model	101
4.7	Experimental QE spectra of Pani/Clay at $T = 297\text{K}$ and $333\text{K}$ compared to simulations with the four site cone model	103
5.1	Experimental deuteron MAS spectrum of emeraldine base at 263 K	106
5.2	Temperature dependence of the full widths at half height of two peaks of spinning sidebands of emeraldine base	107
5.3	Schematic representation of two in-plane rings of the conductive polyaniline	112
5.4	Experimental deuteron MAS spectrum of emeraldine hydrochloride	115
5.5	Comparison of representative spinning sidebands of ES/CSA/m-cresol at two field strengths	117
5.6	Temperature dependence of the integrated intensity of the shifted peak of spinning sidebands of ES/HCl	119
5.7	Comparison of individual spinning sidebands of three conductive salts at different temperatures	120

5.8	Temperature dependence of the shift from zero frequency for emeraldine hydrochloride	122
5.9	Experimental deuteron MAS spectrum of Pani/MMT Clay nanocomposite at 263K	126
6.1	Experimental inversion recovery spectra of emeraldine base at ambient temperature as a function of the relaxation delay	130
6.2	Experimental $T_{1Q}$ lineshapes of emeraldine base at ambient temperature as a function of the relaxation delay	131
6.3	Comparison of experimental and unconstrained bi-exponential $T_{1Z}$ recovery curves for emeraldine base	134
6.4	Unconstrained bi-exponential fit for experimental and EXPRESS simulated $T_{1Z}$ and $T_{1Q}$ data for emeraldine base at ambient temperature base	137
6.5	Experimental and EXPRESS simulated $T_{1Z}$ recovery curves for emeraldine base for frequencies higher than $\pm 64$ kHz	138
6.6	Experimental and EXPRESS simulated $T_{1Q}$ recovery curves for emeraldine base	139
6.7	Unconstrained bi-exponential fit to experimental and EXPRESS simulated fast relaxing $T_{1Z}$ component of emeraldine base at ambient temperature	140
6.8	Experimental and EXPRESS simulated $T_{1Z}$ recovery curves for emeraldine base for frequencies lower than $\pm 64$ kHz	142

6.9	Unconstrained bi-exponential fit for experimental and EXPRESS simulated $T_{1Z}$ and $T_{1Q}$ data for emeraldine hydrochloride at ambient temperature	144
6.10	Representative spinning sideband of experimental MAS inversion recovery spectra of ES/CHI at ambient temperature as a function of the relaxation delay	145
6.11	Dependence of $T_{1Z}$ relaxation time from librational angle for the model of discrete jumps in a cone	147
A.1	Comparison of experimental spectrum of a spinning sideband of emeraldine base at 263 K with different fit functions	156
B.1	$T_2$ correction plot for emeraldine hydrochloride for different temperatures	160

## ABSTRACT

Different forms of ring deuterated polyaniline with different conductivity have been characterized by solid state deuteron nuclear magnetic resonance.

Quadrupole echo (QE) spectra of all forms of polyaniline consist of a superposition of lineshapes for nearly rigid aromatic rings and a small fraction of rings which undergo fast 180° flips. The intensity of the fast flipping component is temperature dependent and different for conductive emeraldine salt (ES) and non-conductive emeraldine base (EB). This is a manifestation of the different structure and morphology of these polymers.

Simultaneous measurements of QE lineshapes and the relaxation time anisotropies allowed an accurate description of motion in polyanilines. Slow, small-angle libration in an asymmetric cone provided the best description for the “rigid” fractions of EB and ES. The broadening of deuteron QE lineshapes is consistent with the presence of a distribution of cone angles. Relaxation time measurements also reveal a relatively narrow distribution of librational rates for the EB sample. For ES, the magic angle spinning (MAS) spectra show the existence of two resolved signals with different relaxation rates, which are ascribed to microscopic domains with very different electrical properties. The unexpectedly short relaxation time found for nonconductive domains in ES can be explained by the presence of localized, unpaired electrons.

Spin count experiments proved that in highly conductive ES samples, loss of NMR signal intensity occurs not only because of high RF reflectance but also because of irreversible dephasing before signal acquisition due to interactions of nuclear spins with localized unpaired electrons.

Deuteron MAS spectra provided unique information about small frequency shifts. Compared to non-conductive EB, conductive emeraldine salts have an additional manifold of spinning sidebands, which is shifted ~5.8 ppm towards higher frequencies. These shifted sidebands arise from quasi-metallic regions of the sample, where deuteron spins interact with delocalized electrons (Knight shift). The experimental temperature dependence of the intensity of the shifted peak can be explained using models developed for amorphous semiconductors. The observation of a Knight shift has an important consequence for the theory of electrical conduction in polyaniline: it implies that polarons are the charge carriers.

## SOLID STATE NMR CHARACTERIZATION OF CONDUCTIVE POLYANILINES

## CHAPTER 1

# CONDUCTIVE POLYMERS

The era of conductive polymers, more commonly called “synthetic metals”, commenced in the mid 1970s with the discovery that a film of an organic polymer, polyacetylene, could be “doped” by treatment with gaseous bromine with concomitant increase in conductivity of 10,000,000<sup>1, 2</sup>. Since then, the field of conductive polymers has developed at an unexpectedly rapid rate. It had presented a strong fundamental scientific challenge, which had been taken up by a diverse community of chemists, physicists and material scientists both in academia and industry.

During the past two decades tremendous advances have been made in our understanding of the chemistry and physics of the synthetic metals, which has led to many successful commercial applications. However, despite extensive study, this area of research still has many unexplained or incompletely understood phenomena.

This chapter is intended as a review of basic concepts pertaining to the field of conductive polymers. Fundamental definitions and concepts that are discussed in later

chapters are introduced. In order to show how our study of conductive polyanilines fits into the framework of the research on synthetic metals, relevant literature is summarized.

## 1.1 CONDUCTIVE POLYANILINE

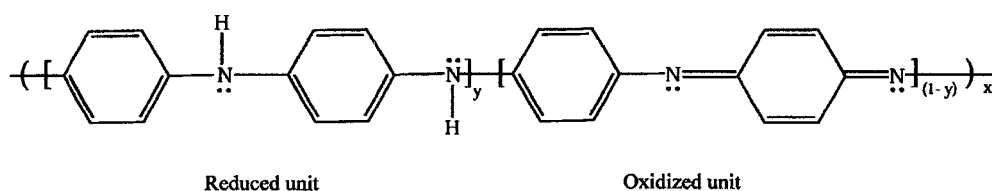
A conductive polymer is defined as an organic polymer that possesses the electrical, electronic, magnetic and optical properties of a metal while retaining the mechanical properties and processibility commonly associated with a conventional polymer. The term is also frequently used to include doped organic polymers having conductivities greater than  $10^{-2}$  S/cm<sup>3</sup>.

All conductive polymers possess a common structural feature – a conjugated backbone. Extended conjugation contributes to electronic conduction in two important ways: (a) carrier mobility – conjugation delocalizes the *p* atomic orbitals into bands of spatially extended molecular orbitals, providing a conduction pathway for electrons, (b) carrier mobility – with increasing degree of conjugation the energy gap between occupied and unoccupied electronic states decreases; the lower this energy gap, the more valence electrons will be promoted into the conduction band.

Polyaniline is one of the oldest known synthetic organic polymers. The first report describing a dark, universally insoluble powder dates back to 1862<sup>4</sup>. In 1910 polyaniline was described as existing in four oxidation states, each of which was thought to be an “octamer”<sup>5</sup>. The current phase of polyaniline research was entered in 1980’s, when better physical characterization of the material became possible.

Nowadays, the term “polyaniline” is employed to describe a polymer of overall composition:

FIGURE 1.1  
SCHEMATIC REPRESENTATION OF POLYANILINE BASE



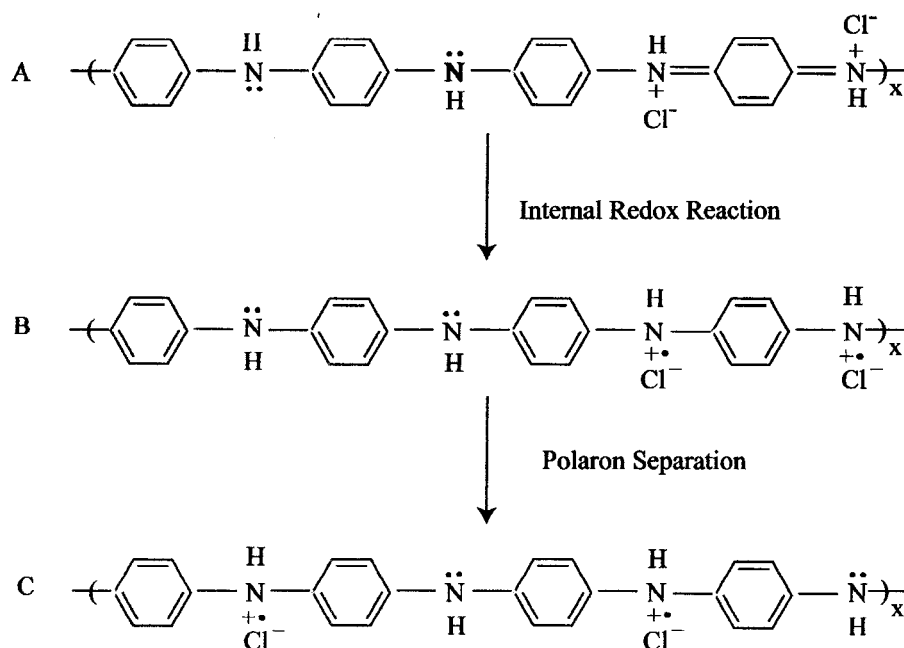
In the generalized base form depicted above,  $(1 - y)$  can vary from 0 to 1 and measures the fraction of oxidized units (containing imine species) on a macroscopic scale i. e. in a bulk sample. When  $(1 - y) = 0$ , the polymer has no such oxidized groups (it contains only amine species) and is commonly known as leucoemeraldine base. The fully oxidized polymer,  $(1 - y) = 1$ , is referred to as pernigraniline base. The half-oxidized polymer, where number of reduced and oxidized units are equal, i. e.  $(1 - y) = 0.5$ , is of special importance and is termed “emeraldine”. Materials, which are believed to be approximately in this oxidation state, but which have not been completely characterized in this regard are also referred to as “emeraldine”.

Polyaniline can be synthesized chemically or electrochemically from aniline monomer<sup>6,7</sup>. Emeraldine base is readily solution-processible and it may be cast as a free standing, flexible film from different solvents. Depending on experimental details, non-crosslinked or physically crosslinked films can be obtained. Uniaxially oriented, partially

crystalline samples are obtained by simultaneous heat treatment and mechanical stretching of emeraldine base films<sup>3,6</sup>.

FIGURE 1.2

SCHEMATIC REPRESENTATION OF EMERALDINE HYDROCHLORIDE



(A) bipolaron centered on quinoid ring; (B) localized polarons; (C) polaron lattice.

The concept of doping is the unique, central and unifying theme, which distinguishes conductive polymers from all other types of polymers<sup>3,6,8</sup>. The controlled addition of known quantities of chemical species results in dramatic changes in the electronic, magnetic, optical and structural properties of the polymer. Doping is reversible to produce the original polymer with little or no degradation of the polymer

backbone<sup>3,6</sup>. In principle, the imine nitrogen atoms of polyaniline can be partially or completely protonated to give the corresponding salts<sup>9</sup>. The degree of protonation of the polymeric base depends on its oxidation state and the pH of the aqueous acid. Complete protonation of emeraldine base by aqueous HCl, results in the formation of a structure illustrated in Figure 1.2A, which may be thought of as containing localized bipolarons centered on the quinoid rings. Some studies suggest<sup>8,10</sup> that emeraldine hydrochloride (Figure 1.2A) rearranges, via proton-assisted spin-unpairing mechanism, to form (Figure 1.2B) semiquinone radical cations (polarons). These polaron pairs then separate because of Coulomb repulsion to form a polaron lattice structure (Figure 1.2C). Protonation of emeraldine base is accompanied by an increase in conductivity of approximately 10 orders of magnitude. Remarkably, the number of electrons associated with the polymer remains unchanged upon doping<sup>3,6</sup>.

A very important step in solution processing of polyaniline was made relatively recently by synthesizing emeraldine salt using organic sulfonic acids containing large organic groups<sup>11,12</sup>. Such emeraldine salt solutions can be easily processed and blended with conventional polymers, thereby exploiting the most desirable characteristics of each type of polymer.

As a result of different synthesis conditions and processing methodologies, the conductivity of emeraldine salt may vary within five orders of magnitude. For example, low temperatures allow formation of higher molecular weight polymers and prevent cross-linking, which leads to higher conductivities. Physical properties of polyaniline films, cast from solution of *m*-cresol and chloroform, doped with camphorsulfonic acid (CSA) were compared and discussed in detail by MacDiarmid and coworkers<sup>3</sup>. X-ray

diffraction data, electronic spectra, dielectric constant and reduced viscosities of film cast from m-cresol are consistent with "expanded coil" conformations, whereas the Pani film cast from chloroform exhibit "tight coil" conformations. Consequently, the room temperature conductivity of emeraldine salt / chloroform film was only  $\sim 10^{-1}$  S/cm while that of emeraldine salt /m-cresol was  $\sim 200$  S/cm.

The highest reported experimentally obtained conductivity of emeraldine salt is  $990 \pm 50$  S/cm<sup>13</sup>. It is unlikely that a conductive polymer can be used as a substitute for copper (as an electrical conductor) unless its conductivity can be increased by 2-3 orders of magnitude. However, the unique combination of properties, displayed by polyaniline and its blends with conventional polymers, appear to show great promise for a variety of applications. At the present time, polyaniline (Pani) is one of the most technologically important polymers. It is unique among conducting polymers because of its relatively high conductivity ( $\sim 10^3$  S/cm), environmental stability, ease of synthesis and low cost of production.

The electronic conductivity of polyaniline makes it a suitable candidate as cathodes in rechargeable batteries<sup>3,7,14</sup>. The advantages are the ease of fabrication, low cost and light weight. Thin, transparent, flexible, highly conductive films of polyaniline can be deposited on conventional plastics and used for light-emitting diodes<sup>3,6,15,16</sup>.

When a conductive polymer is mixed with an insulating material, essentially no increase in conductivity is observed until particles of conductive polymer touch each other. Polyaniline has a unique ability to undergo percolation at very low loading levels (< 5 %) when blended into an insulating polymer. The blends show great electromagnetic shielding properties<sup>3,15</sup> and have use in static dissipation<sup>3,14</sup>. The bulk conductivity of

polyaniline thin films has also been utilized in chemical sensing devices. Electrical conductivity and optical absorption of the polymer is strongly influenced by certain gas molecules. Thin-film polyaniline-based sensing devices are inexpensive and operate at room temperature with satisfactory selectivity for gases <sup>6,7,15,17</sup>.

A very important application of polyaniline involves the corrosion protection of metals such as iron <sup>7,15</sup>. It appears that the effect is based not on mechanical protection but on the electronic interactions between the polymer and the metal.

Another use of polyaniline, which does not involve its electronic properties is gas separation membranes <sup>3,14</sup>. Polyaniline membranes exceed the selectivity of all known separation membranes for many gas mixtures such as O<sub>2</sub> and N<sub>2</sub>. Although the process by which this occurs is not yet clear, it seems that polyaniline membranes operate through the formation of molecular-sized channels in the membrane formed through controlled doping and dedoping of the polymer.

The polyanilines are very useful for fabrication electrochromic devices <sup>3,7,14,15</sup>. Here the ability of polyaniline to show a whole range of colors (red, blue, green) as a result of its oxidation and protonation forms is exploited. Many electrochemically dopant-induced structure-property changes in polyaniline have been described for use in, for example, electrochromic windows and displays, redox capacitors, electromechanical actuators <sup>3,7,14,15,18</sup>.

## 1.2 EXPERIMENTAL AND THEORETICAL STUDIES

Since 1980's tremendous advances have been made in understanding chemical and physical properties of polyanilines, but due to the materials' complex morphology there are still some fundamental questions which remain unclear.

It has been reported <sup>19</sup> that the predicted room temperature intrinsic conductivity of emeraldine salt is  $10^6$  S/cm, which is approximately equal to that of copper. Better understanding of the relationship between structure and electric properties of the polymer, elucidating the mechanism of conduction and determining what defects are responsible for failure to achieve the predicted high intrinsic conductivity, are common goals in conductive polyaniline research.

Models of three-dimensional amorphous semiconductors <sup>20</sup> often have been used to account for charge delocalization phenomena in conductive polyaniline. However, in conductive polymers the dopant ions are positioned interstitially between chains, whereas in conventional semiconductors they are usually substituted directly into the host lattice. Furthermore, covalent bonding along polymer chains and weak bonding between them result in a quasi-one-dimensional morphology. The conductivity of polyaniline decreases with decreasing temperature, unlike conventional metals, even though room temperature conductivity values up to  $\sim 10^3$  can be achieved <sup>13</sup>.

Different models account for different physical properties, such as, for example, the temperature dependence of dc conductivity, thermoelectric power and dielectric constant. In conductive polymers, complete evaluation of the properties is extremely

complicated because of structural disorder. As was determined by x-ray diffraction studies<sup>21-23</sup>, conductive emeraldine salt is partially crystalline and as temperatures approaches zero, the crystalline domains are associated with so-called “metallic islands”<sup>24</sup>. These crystalline islands are interconnected in a complex manner by disordered or/and partially ordered polymer chains. Distinguishable contributions to different physical properties are expected from (a) metallic islands and relatively well-organized chains in the amorphous regions and (b) the disordered polymer chains. Commonly one of these contributions dominates for a given sample crystallinity and temperature range. The models most frequently used to describe conductive polymers are the granular metallic model (GMM)<sup>24,25</sup>, quasi-one dimensional and three dimensional variable range hopping (VRH)<sup>24,25</sup>, metallic box (MBM) and interrupted metallic strands models (IMSM)<sup>24,25</sup>, and the model of Nakhmedov, Prigodin and Samukhin<sup>26</sup>. The fundamental assumption of GMM is that the metallic islands are embedded in an insulating background, and there is distinct phase segregation between the two states. The VRH model emphasizes nearest-neighbor interchain hopping in disordered regions, while GMM posits charge tunneling between metallic islands. The MBM and the IMSM were developed in terms of linear metallic strands interrupted by insulating lattice defects. In the MBM these metallic strands are assumed to bundle and are treated as a metallic box. Nakhmedov, Prigodin and Samukhin studied the conductivity and dielectric response at a finite frequency in quasi-one-dimensional conductors. The effect of electron delocalization at high temperatures, with increased chain alignment in the disordered regions, is described. The importance of interchain hopping is emphasized in this model.

One of the most fundamental unresolved issues is whether the metallic states are predominately one-dimensional (1D) or three-dimensional (3D). For example, based on electron spin resonance and nuclear magnetic resonance studies, K. Mizoguchi *et al.*<sup>27</sup> concluded that a conducting island consists of a single chain. Other authors<sup>24,28</sup> challenged this conclusion and demonstrated a 3D nature of the metallic state in polyaniline, using x-ray diffraction, electron spin resonance, dielectric constant and other related data, as well as some theoretical results.

For all organic conjugated polymers the gap between valence band (VB) and conduction band (CB) is larger than 1.5 eV so that these materials are intrinsically insulating. Initially, the high conductivity increase observed upon doping of organic polymers was ascribed to the formation of unfilled electronic bands. It was simply assumed that upon p-type or n-type doping, electrons were respectively removed from the top of the VB or added to the bottom of the CB, in analogy to the mechanism of generation of charge carriers in doped inorganic semiconductors. This assumption was however quickly challenged by the discovery that some conductive polymers, such as for example polyacetylene and polypyrrole<sup>29</sup>, display conductivity, which does not seem to be associated with unpaired electrons but rather with spinless charge carriers (bipolarons, solitons).

For conductive polyaniline, the controversy whether the charge carriers are polarons or bipolarons is an on-going debate. Electron spin resonance (ESR) data played a crucial role in the history of the development of the conduction mechanism theory. The ESR signal intensity increases sharply in the early stages of emeraldine base doping (as does the conductivity of the material). It is commonly accepted that this is due to

polarons formed in the early stage of the process. The polarons are thought to be isolated from each other and, therefore, the formation of polarons contributes little to the conductivity while every polaron contributes to the ESR intensity. Spins behaving this way belong to the category of Curie spins. As the doping level of polyaniline increases the intensity of ESR signal has a sharp decrease and as the conductivity of emeraldine salt reaches its maximum value, a minimum in ESR intensity is observed <sup>30</sup>. One reasonable explanation of the decline in ESR intensity can be the formation of the spinless bipolarons at higher doping level <sup>24,29</sup>. On the other hand, some authors <sup>10,31</sup> believe that the polaron lattice is formed at higher doping levels, as originally isolated spin states merge together. In this polaron lattice model, only spins at (or around) Fermi level contribute to ESR signal intensity. The spins behaving this way belong to the category of Pauli spins. Since only a small fraction of electron spins remains ESR active on conversion from Curie to Pauli behavior, a sharp decrease in ESR intensity is expected to accompany the major increase in conductivity.

Nuclear magnetic resonance is a powerful and widely exploited tool for studying the microscopic structure, dynamics and morphology of polymers. Polyaniline has been extensively studied using <sup>13</sup>C<sup>32-34</sup>, <sup>15</sup>N<sup>35</sup>, <sup>1</sup>H<sup>27,36-39</sup> and <sup>2</sup>H<sup>32</sup> NMR.

<sup>15</sup>N study of leucoemeraldine and emeraldine base forms of polyaniline <sup>35</sup> revealed that the emeraldine base polymer exists as an alternating copolymer of oxidized and reduced units. End-groups were not detected experimentally due to sensitivity limitations.

Kaplan and coworkers observed separation of deuterium NMR spectra into two components, attributed to flipping and rigid rings <sup>32,40</sup>. The fact that conductive

emeraldine hydrochloride had about a third as many fast flipping rings as emeraldine base was consistent with structure containing unseparated polarons or a more realistic one containing poly(semiquinone radical cation) segments and residual reduced units. From separation of deuterium spectra of polyanilines into two components, Jeener-Broekaert experiments and  $^{13}\text{C}$  relaxation measurements on emeraldine base it was concluded that there is a wide distribution of correlation times for ring flips ( $\sim 8$  orders of magnitude) in the polymer.

Kolbert and coworkers conducted a  $^{13}\text{C}$  NMR study of emeraldine salt film doped with camphor sulphonic acid (CSA) and cast from m-cresol<sup>33</sup>. A pronounced broadening of  $^{13}\text{C}$  resonance made it impossible to analyze the spectra. Any potential Knight would likely have been obscured by the 60-ppm broadening.  $^{13}\text{C}$  spin-lattice relaxation rate measurements, on the other hand, were shown to obey a modified Korringa relation<sup>41</sup> for relaxation via the hyperfine coupling to the conduction electrons.

HF-doped polyaniline powder was examined by Espe *et al.* using  $^{13}\text{C}$ ,  $^{15}\text{N}$ ,  $^{19}\text{F}$  solid state NMR<sup>42</sup>. Chemical shifts in  $^{19}\text{F}$  NMR spectra revealed three distinct types of charged environments, which were assigned to three possible arrangements of  $\text{F}^-$  counterions near positively charged nitrogens. Spin count experiments showed that only one-third of all the chains in fully doped polyaniline were detected. This observation was interpreted as an inability to observe an NMR signal from the entire crystalline region of the conductive salt, plus amorphous regions within 50 Å of the crystalline border.

The frequency dependence of the proton relaxation rate in CSA-doped polyaniline was investigated by Mizoguchi<sup>27</sup> and Beau<sup>36</sup>. It showed that spin diffusion is strongly anisotropic and quasi-one dimensional. The on-chain diffusion rate was thought to be

independent of the protonation level while the transverse diffusion exhibited a sudden drop at the percolation threshold<sup>27</sup>. This behavior was attributed to be consistent with the “conductive island” picture, but it was concluded that each island consisted of just one polymer chain. Mizoguchi *et al.* concluded that the conductivity is governed by inter-chain hopping.

We used <sup>2</sup>H NMR to study emeraldine base, emeraldine salts, and a polyaniline/Montmorillonite nanocomposite. Quadrupole echo (QE) line shapes were used to quantify the temperature dependent fraction of rapidly flipping aromatic rings in the materials. Deuteron relaxation measurements are an excellent choice of technique to quantitatively characterize dynamic processes in polymers. NMR relaxation measurements are sensitive to a wide range of motional rates, ranging from seconds to picoseconds<sup>43</sup>. As was discussed previously, most of the NMR studies were conducted on insulating polyanilines. Many authors, investigating the highly conductive form of the polymer, have commented on the unfortunate loss of NMR spectral resolution. We demonstrate that deuteron magic angle spinning (MAS) offers unexpected relief from this difficulty and provides significantly better resolution and improved sensitivity. Unlike emeraldine base, MAS spectra of ring-deuterated emeraldine salt show two partially resolved sideband manifolds, with different line widths and integrated intensities. We believe this is the first observation of a Knight shift in bulk polyaniline.

## 1.3 CLAY NANOCOMPOSITES

Conducting polymers encapsulated in two-dimensional layers of inorganic ceramics or one-dimensional channels of organic hosts offer fascinating new perspectives. The constrained environment of an inorganic host should lead to a high degree of polymer order within the host layers, and this may have a profound effect on polymer structure, properties, and mechanisms of conduction. These nanocomposite systems represent a new class of materials with diverse electrical, optical, mechanical, and thermal properties.

Clays are interesting host materials because of their ready availability, small particle size and well-known propensity for intercalation<sup>44</sup>. The basic structural units in silicate clays are silica and gibbsite sheets. The former consists of  $SiO_4^{2-}$  tetrahedra connected at three corners in the same plane forming a hexagonal network. The tips of tetrahedra all point in the same direction. The gibbsite sheet consists of two planes of hydroxyl ions between which lies a plane of magnesium or aluminum ions, which are octahedrally coordinated by the hydroxyls; this unit is known as octahedral sheet. Tetrahedral and octahedral sheets are combined so that the oxygens at the tips of the tetrahedra project into a plane of hydroxyls in the octahedral sheet and replace two-thirds of the hydroxyls. This combination of sheets forms a clay layer<sup>44</sup>.

Montmorillonite (MMT) is one of the most abundant naturally occurring clay minerals<sup>44</sup>. Its lattice consists of a sheet of octahedral alumina sandwiched between two silica sheets. Substituting ions of lower charge for higher charge in both the octahedral (e.g.,  $Mg^{2+}$  replacing  $Al^{3+}$ ) and tetrahedral (e.g.,  $Al^{3+}$  replacing  $Si^{4+}$ ) sheets, produces

negatively charged layers. Montmorillonite's general formula is  $(Al_{2-x}Mg_x)(Si_4)O_{10}(OH)_2$ . Its off-white color is due to a small amount of  $Fe^{2+}$  and  $Fe^{3+}$  impurities, replacing *Al* or *Si*.

Due to the strong intraplanar and weak interplanar binding forces, MMT clay layers can expand to accommodate loosely bound hydrated cations, water, and polar organic solvents. The cation exchange capacity of the clay is from 80 to 100 milliequivalents per 100 grams<sup>44</sup>.

It has been demonstrated<sup>3</sup> that the conductivity of polyaniline is strongly dependent on the degree of molecular alignment and the density of chemical and/or structural defects. However, there have been no reports on obtaining fully aligned polyaniline. The idea is that the host matrix will provide an environment that will favor polymer chain ordering. A low density of defects within the chains could result when the polymerization reaction occurs in a constrained environment. The reduced dimensions of organoclay matrix (on the nano-scale) preclude intermolecular interactions and cross-linking occurrence.

As was mentioned previously, goals in conductive polyaniline studies also included the optimization of the charge transport properties and a better understanding of the relationship between electronic and lattice structure. Well-defined conducting structures of nanometer dimensions can be greatly beneficial along this line, providing reduced dimension of electronic circuitry. Introduction of one layer of polyaniline into the two-dimensional clay matrix could provide an understanding of the importance of formation of three-dimensional structures on the conduction mechanism.

## CHAPTER 2

### NMR AND CONDUCTIVE POLYMERS

Nuclear Magnetic Resonance (NMR) is one of the most useful physical tools for investigating all states of matter. It can be applied to a wide range of materials such as brains, bones, cells, ceramics, chocolate, liquid crystals, surfaces, proteins, polymers, soil, oil wells, drug delivery systems, laser-polarized gases, metals and many, many others. This technique was born in 1945 when Purcell, Torrey, Pound and almost simultaneously Bloch, Hansen, Packard detected a weak radio frequency (RF) signal generated by atomic nuclei.

Magnetic resonance can be observed when nuclei possess spin angular momentum,  $I$ . In presence of a magnetic field, the transitions between different spin angular momentum quantum states of nuclei can be stimulated by resonant RF photons. Interaction between the spin angular momentum of the nucleus and the static magnetic field (Zeeman interaction) provides the largest contribution to the energies of the spin states. The interactions of interest, though, are small perturbations to these zero order

energy levels. Effects of these perturbations on NMR spectra reflect molecular structure, order and dynamics within a sample.

This chapter describes basic NMR principles and experimental techniques relevant to the present study. A summary of NMR theory, important interactions for conductive deuterated materials and motional modulation of these interactions are followed by a brief theoretical description of conductive polymers.

## 2.1 NMR BACKGROUND

### 2.1.1 SPIN ANGULAR MOMENTUM AND BASIC THEORY OF NMR

Spin is a fundamental intrinsic property of a particle. Atomic nuclei may consist of many particles coupled together so that in any given state, the nucleus possesses a total magnetic moment  $\vec{\mu}_n$  and a total angular momentum  $\vec{I}$ . These two quantities are related by the fundamental equation<sup>43,45</sup>

$$\vec{\mu}_n = \gamma_n \hbar \vec{I} \quad [2.1]$$

where  $\hbar$  is Planck's constant, and  $\gamma_n$  is the gyromagnetic ratio, characteristic of the observed nucleus. Spin angular momentum is a quantum property. One should regard it as a (vector) operator  $\vec{I} = I_x \vec{x} + I_y \vec{y} + I_z \vec{z}$ , whose eigenvalues define the observable quanta of angular momenta about space fixed axes  $\vec{x}$ ,  $\vec{y}$  and  $\vec{z}$ . Matrix elements for angular momentum operators in Cartesian basis are given by<sup>46</sup>

$$\langle \text{Im} | I_z | I' m' \rangle = m \delta_{mm'} \delta_{II'} \quad [2.2]$$

$$\langle \text{Im} | I_x | I' m' \rangle = \frac{1}{2} \delta_{II'} \left( \delta_{mm'+1} \sqrt{(I+m)(I-m+1)} + \delta_{mm'-1} \sqrt{(I-m)(I+m+1)} \right) \quad [2.3]$$

$$\langle \text{Im} | I_y | I' m' \rangle = \frac{i}{2} \delta_{II'} \left( -\delta_{mm'+1} \sqrt{(I+m)(I-m+1)} + \delta_{mm'-1} \sqrt{(I-m)(I+m+1)} \right) \quad [2.4]$$

Here,  $I$  and  $m$  are eigenvalues of the total angular momentum operator  $\vec{I}^2$  and its projection on  $\vec{z}$  axis ( $\vec{I}_z$ ), respectively.

If a nuclear spin is placed in a strong static magnetic field,  $\vec{B} = B_0 \vec{z}$ , the magnetic moment tends to align parallel to the field, corresponding to the lower energy state. The interaction of the magnetic moment and the field can be represented in terms of Hamiltonian operator

$$H = -\vec{\mu}_n \cdot \vec{B} = -\gamma_n \hbar B_0 I_z = -\hbar \omega_0 I_z \quad [2.5]$$

where  $\omega_0 = \gamma_n B_0 = 2\pi\nu_0$  is Larmor frequency. Thus, allowed energy levels are

$$E_m = -m_I \hbar \omega_0 \quad [2.6]$$

$$m_I = I, I-1, \dots, -I$$

Deuterons have spin  $I = 1$ , so that  $m_I = 1, 0, -1$

The magnetic moment  $\mu_e$  of the electron is analogous to that of a nucleus:

$$\vec{\mu}_e = -g\beta\vec{S} = \gamma_e \hbar \vec{I} \quad [2.7]$$

Here  $\vec{S}$  is the spin angular momentum of the electron,  $g$  is a dimensionless constant called the  $g$ -factor and  $\beta = e\hbar/2mc$  is the Bohr magneton. As before, the interaction between the electron magnetic moment and the static magnetic field is represented by a Hamiltonian

$$H = -\vec{\mu}_e \cdot \vec{B} = g\beta B_0 S_z \quad [2.8]$$

Note, that because of difference in the sign of charges,  $\mu_e$  and  $\mu_n$  are antiparallel. The electron spin is equal to  $1/2$ , so that  $m_s = 1/2, -1/2$ .

## 2.1.2 EQUATION OF MOTION

A theoretical treatment of a realistic NMR experiment requires that the time evolution of a large number of spins must be described. This requirement leads to the formalism of statistical mechanics. Consider an ensemble of spins, divided into  $N$  non-interacting identical systems. Each system has the same Hamiltonian, which describes how the spins in that system interact with each other and their surroundings. The state of such a system is given by<sup>45,47</sup> a linear combination of Hamiltonian eigenfunctions  $|\varphi_k\rangle$

$$|\psi(t)\rangle = \sum_{k=1}^M c_k(t) |\varphi_k\rangle \quad [2.9]$$

Any observable property of the ensemble, as for example  $x$  - component of the magnetization,  $\mu_x$ , is obtained by averaging over  $N$  systems

$$\langle \mu_x \rangle = \sum_{k,n} \langle \varphi_n | \rho | \varphi_k \rangle \langle \varphi_k | \mu_x | \varphi_n \rangle = \text{Tr}(\rho \mu_x) \quad [2.10]$$

where  $\rho$  is a density operator and  $\rho_{kn} = \frac{1}{N} \sum_{i=1}^N c_k^{(i)}(t) c_n^{(i)}(t)$  is the corresponding density matrix. The general form of the expansion coefficients is  $c_k^{(i)} = a^{(i)} e^{i\alpha^{(i)}}$ . The diagonal density matrix elements are real, non-negative numbers, which correspond to the populations of eigen states. The sum of the populations is always normalized to one. The

difference in spin state populations indicates net longitudinal spin polarization, i. e. magnetization of the sample in the direction of the external field. Off-diagonal density matrix elements are complex numbers, associated with coherences. The presence of single quantum coherences indicates an observable transverse spin magnetization, i. e. a net spin polarization perpendicular to the field.

The time evolution of the density operator is described by the Liouville von-Neuman equation <sup>45,47</sup>:

$$\frac{d\rho(t)}{dt} = \frac{i}{\hbar} [\rho(t), H(t)] \quad [2.11]$$

For a time independent Hamiltonian, the exact solution is

$$\rho(t) = e^{-\frac{iHt}{\hbar}} \rho(0) e^{\frac{iHt}{\hbar}} \quad [2.12]$$

In NMR, the Hamiltonian typically consists of a large time-independent part  $H_0$ , and a much smaller time dependent part,  $H_1(t)$ , so that  $H = H_0 + H_1(t)$ . The time-independent term,  $H_0$ , includes the time average of the Hamiltonians for the time-dependent interactions, which ensures that the average of  $H_1(t)$  is zero. To simplify calculations, an interaction representation is introduced, which removes the rapid oscillations produced by  $H_0$ .

$$\rho^*(t) = e^{\frac{iH_0t}{\hbar}} \rho(t) e^{-\frac{iH_0t}{\hbar}} \quad [2.13]$$

$$H_1^*(t) = e^{\frac{iH_0t}{\hbar}} H_1(t) e^{-\frac{iH_0t}{\hbar}} \quad [2.14]$$

The equation of motion in the interaction representation is

$$\frac{d\rho^*(t)}{dt} = \frac{i}{\hbar} [\rho^*(t), H_1^*(t)] \quad [2.15]$$

It is interesting to note, that when  $H_0 = -\hbar\omega_0 I_Z$ , the interaction representation is equivalent to a transformation to a rotating reference frame whose rotation frequency is equal to the Larmor frequency. Thus, any alternating RF fields applied at the Larmor frequency will appear static in this frame.

When  $H_I(t)$  includes random motion, equation 2.15 cannot be solved exactly because the precise time dependence is not known. However, one can use successive approximation techniques (Bernoulli method)<sup>45</sup>. Assuming that the density matrix does not vary appreciably in a time interval  $\tau = [0, t]$ , the solution is then given by a truncated series:

$$\begin{aligned} \rho^*(t) = & \rho^*(0) + \frac{i}{\hbar} \int_0^t [\rho^*(0), H_1^*(t')] dt' - \\ & - \frac{1}{\hbar^2} \int_0^t dt' \int_0^{t'} dt'' [[\rho^*(0), H_1^*(t'')], H_1^*(t')] \end{aligned} \quad [2.16]$$

## 2.2 IMPORTANT INTERACTIONS

For a solid sample in a magnetic field, the dominant interaction is the Zeeman coupling of the nuclear magnetic moment with the external field. This interaction is usually large enough (10 - 100 MHz), so that all the others can be treated by perturbation theory. Despite the fact that interactions of nuclear or electron spins with each other and their surrounding are small in comparison with Zeeman energy, they provide fundamental information about structure and dynamics, and are hence the primary motivation for doing solid state NMR.

For deuterons, relevant interactions include the coupling of nuclear electric quadrupole moment with the electric field gradient at the site of nucleus, dipole-dipole interactions between spins and hyperfine interactions of electron angular momenta with nuclear spins. The total Hamiltonian can be written as

$$H = H_{Zn} + H_{Ze} + H_Q + H_D + H_H \quad [2.17]$$

where  $H_{Zn}$  and  $H_{Ze}$  are the Hamiltonian for the nuclear and electron Zeeman interaction respectively,  $H_Q$  describes the electric quadrupole interaction,  $H_D$  refers to the nuclear magnetic dipole-dipole interaction, and  $H_H$  describes the interactions of the nuclear spin with electron spin and orbital coordinates. The latter interaction of the nuclear magnetic moment with the magnetic field produced by electrons is called hyperfine interaction; it consists of two terms:

$$H_H = H_{SL} + H_{en} \quad [2.18]$$

where  $H_{SL}$  describes coupling of nuclear angular momentum to electron orbital motion (the chemical shielding interaction) and  $H_{en}$  is a dipolar coupling between electron and nuclear spins.

These interactions can be written in terms of Cartesian vector-tensor products or in terms of a sum of the spherical irreducible tensor products<sup>46,48</sup>. In Cartesian representation an interaction Hamiltonian has the following form

$$\hat{H} = \vec{I}_1 \hat{O} \vec{I}_2 \quad [2.19]$$

Here, the second rank tensor  $\hat{O}$  can be represented by a  $3 \times 3$  matrix. It can be transformed from one coordinate system to another by operating on it with rotation matrices  $\hat{O}' = R^{-1}(\alpha, \beta, \gamma) \cdot \hat{O} \cdot R(\alpha, \beta, \gamma)$ , where  $\alpha$ ,  $\beta$  and  $\gamma$  are the Euler angles. The convention used here for transformation is that of Rose: the axis system is rotated through

$\alpha$  about z-axis,  $\beta$  about  $y'$ -axis and  $\gamma$  about  $z''$ -axis<sup>46</sup>. The laboratory axis system is usually chosen so that the direction of the external field  $\vec{B}_0$  coincides with  $\vec{z}$  direction. The coordinate system in which the second rank tensor is diagonal is known as the principal axis system (PAS). The axes of the PAS point the same direction as the eigenvectors of the interaction tensor. By convention, the z-axis points along the largest eigen-vector of the tensor, and the x-axis points along the smallest eigen-vector. In this work elements of  $\hat{O}(LAB)$  are denoted by  $x$ ,  $y$  and  $z$  subscripts, while in the PAS numerical values are used.

The expression for an interaction Hamiltonian (in units of  $\hbar$ ) in spherical irreducible tensor form is

$$\hat{H} = \sum_{l=0}^{l_{\max}} \sum_{m=-l}^l (-1)^m \hat{A}_{-m}^{(l)} \hat{T}_m^{(l)} \quad [2.20]$$

The maximum rank of the spherical tensor, involved in the interaction description,  $l_{\max}$ , is determined by the selection rules for allowed quantum transitions between stationary spin states. Tensor  $\hat{A}_m^{(l)}$  depends only on the spin operators and tensor  $\hat{T}_m^{(l)}$  depends on the electronic state and spatial coordinates of the interacting local fields. Coordinate transformations of these tensors can be done using Wigner rotation matrix formalism<sup>49</sup>.

## 2.2.1 ZEEMAN INTERACTION

The Zeeman interaction refers to the coupling of nuclear or electronic spin to the external static field,  $B_0$ . The Hamiltonian has the form:

$$H_Z = -\gamma \hbar B_0 I_Z \quad [2.21]$$

$H_Z$  is a time independent Hamiltonian, and its eigenvalues are simple, being only multiples ( $\gamma\hbar B_0$ ) of the eigenvalues of  $I_Z$ . It follows that for spin  $I$ , there are  $(2I+1)$  equally spaced Zeeman energy levels

$$E_m = -m\hbar\omega_0 \quad [2.22]$$

Assuming that transitions are allowed only for  $\Delta m = \pm 1$ , the NMR spectrum is then a single,  $2I$ -fold degenerate line at Larmor frequency  $\omega_0 = \gamma B_0$ .

Since most of the experiments described in this dissertation were conducted using a laboratory spectrometer based on 7 T magnet, the strength of the interactions will be given relative to this field; the Larmor frequency for a deuteron in 7 T field is 46.06 MHz.

## 2.2.2 THE QUADRUPOLE INTERACTION

If one describes the nucleus and the surrounding electronic wave function as two classical charge distributions  $\rho_n(r_n)$  and  $\rho_e(r_e)$ , their electrostatic energy is

$$E = \iint \frac{\rho_e(r_e)\rho_n(r_n)dr_e dr_n}{|r_e - r_n|} \quad [2.23]$$

which can be readily factored into a multipole expansion:

$$\begin{aligned} E &= \sum_{l=0}^{\infty} \sum_{m=-l}^l \frac{4\pi}{(2l+1)} \frac{r_n^l}{r_e^{l+1}} \rho_n(r_n)\rho_e(r_e)Y_m^{*(l)}(\theta_n, \varphi_n)Y_m^{(l)}(\theta_e, \varphi_e) = \\ &= \sum_{l=0}^{\infty} \sum_{m=-l}^l (-1)^m A_m^{(l)}(r_n, \theta_n, \varphi_n)T_m^{*(l)}(r_e, \theta_e, \varphi_e) \end{aligned} \quad [2.24]$$

We assumed here that  $r_e \gg r_n$ . It is clear that  $A_m^{(l)}$  and  $T_m^{(l)}$  transform under rotation of the coordinate system as spherical harmonics of order  $l$ . The tensor operator  $A_m^{(l)}$  with  $2l+1$

components is called the multipole moment of order  $l$ . If the state of the nucleus is described by a wave function  $\phi_n$ , then

$$\langle A_m^{(l)} \rangle = \langle \phi_n | A_m^{(l)} | \phi_n \rangle \quad [2.25]$$

Odd values of  $l$  are forbidden<sup>50</sup>, if we assume that stationary nuclear states have well-defined parities. It follows from well-known properties<sup>45,50</sup>, that for a particle of spin  $I$ , the matrix elements  $A_m^{(l)}$  are different from zero if  $0 \leq l \leq 2I$ . Therefore, nuclei of spin  $I \geq 1$  have quadrupole moments. Since the nuclear radius  $r_n$  is much smaller than the electron radius  $r_e$ , the multipole expansion of electrostatic energy (Eq. 2.24) converges rapidly. This explains why there is little experimental evidence of electrostatic interactions with  $l > 2$ .

It can be shown that components of the nuclear quadrupole tensor  $A_m^{(2)}$  can be written as

$$\begin{aligned} A_0^{(2)} &= \frac{1}{\sqrt{6}}(3I_z^2 - I \cdot I) \\ A_{\pm 1}^{(2)} &= \mp \frac{1}{2}(I_z I_{\pm} + I_{\pm} I_z) \\ A_{\pm 2}^{(2)} &= \frac{1}{2} I_{\pm}^2 \end{aligned} \quad [2.26]$$

If  $V(x, y, z)$  is the electrostatic potential produced by electrons at the point  $x, y, z$ , then components of the electronic tensor  $T_m^{(2)}$  in principal axis system become

$$\begin{aligned} T_0^{(2)}(PAS) &= \frac{\sqrt{6}}{4I(2I-1)} \omega_Q \\ T_{\pm 1}^{(2)}(PAS) &= 0 \\ T_{\pm 2}^{(2)}(PAS) &= \frac{1}{4I(2I-1)} \omega_Q \eta \end{aligned} \quad [2.27]$$

where  $\omega_Q = e^2 Q V_{33}$  is the quadrupole coupling constant,  $e$  is the charge of electron and  $Q$  is the quadrupole moment. The terms  $V_{ii}$  are the principal components of the electric field gradient tensor (EFG), so that  $|V_{33}| \geq |V_{22}| \geq |V_{11}|$  and  $\eta$  is an asymmetry parameter

$$\eta = \frac{V_{11} - V_{22}}{V_{33}}.$$

For deuterons, quadrupole coupling is the dominant interaction. Its strength is approximately 170 – 250 kHz, which is still two orders of magnitude less the Zeeman term, so that it produces a shift of Zeeman energy levels (Figure 2.1), which can be calculated using first order perturbation theory.

$$H = H_{Zn} + H_Q = \begin{pmatrix} -\omega_0 + \frac{T_0^{(2)}}{\sqrt{6}} & \frac{T_{-1}^{(2)}}{\sqrt{2}} & T_{-2}^{(2)} \\ -\frac{T_1^{(2)}}{\sqrt{2}} & -\frac{2T_0^{(2)}}{\sqrt{6}} & -\frac{T_{-1}^{(2)}}{\sqrt{2}} \\ T_2^{(2)} & \frac{T_1^{(2)}}{\sqrt{2}} & \omega_0 + \frac{T_0^{(2)}}{\sqrt{6}} \end{pmatrix} \quad [2.28]$$

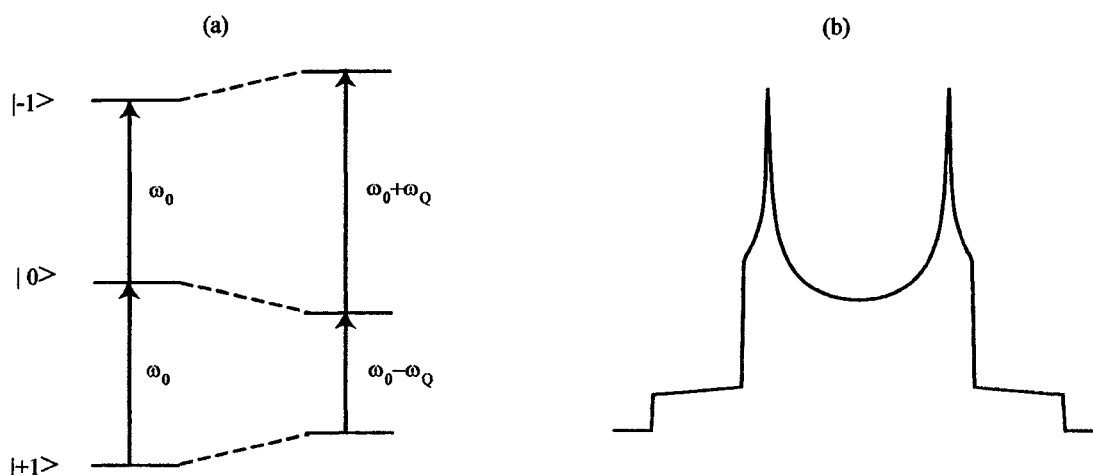
Instead of single transition at the Larmor frequency, two symmetrically shifted resonance frequencies are observed:

$$\begin{aligned} \omega_{21} &= \omega_0 - \frac{3}{\sqrt{6}} T_0^{(2)} \\ \omega_{32} &= \omega_0 + \frac{3}{\sqrt{6}} T_0^{(2)} \end{aligned} \quad [2.29]$$

In the case of powdered samples, an orientation dependent distribution of doublets will be observed in deuteron spectrum. If  $\Omega_{PL} = (\alpha_{PL}, \beta_{PL}, \gamma_{PL})$  are Euler angles relating the principal axis system to the laboratory frame, and  $D_{ij}^{(2)}(\Omega_{PL})$  are the components of

FIGURE 2.1

## DEUTERON ENERGY LEVELS AND POWDER PATTERN



(a) Deuteron Zeeman levels and quadrupolar shifts. (b) Powder pattern resulting from orientation dependence of overlapping quadrupolar doublets.

Wigner rotation matrices<sup>49</sup>, then the second rank tensor transformation from PAS to LAB can be written

$$T_0^{(2)}(LAB) = \sum_{m=-2}^2 D_{0m}^{(2)}(\Omega_{PL}) T_m^{(2)}(PAS) \quad [2.30]$$

It is convenient to characterize experimentally observed resonances in deuteron spectra by the distance between quadrupole doublet (“horns”):

$$2\Omega_Q = \sqrt{6} T_0^{(2)}(LAB) = \frac{3}{4} \omega_Q (3 \cos^2 \beta_{PL} - 1 + \eta \sin^2 \beta_{PL} \cos 2\gamma_{PL}) \quad [2.31]$$

## 2.2.3 MAGNETIC DIPOLAR INTERACTION

The strength of the magnetic field at the nucleus may be significantly affected by the fields of nearby magnetic moments of electrons and other nuclei. The classical energy of interaction between two magnetic moments,  $\mu_1$  and  $\mu_2$ , in *dipolar approximation* is<sup>45,51</sup>

$$E = \frac{(\vec{\mu}_1 \cdot \vec{\mu}_2)}{r^3} - 3 \frac{(\vec{\mu}_1 \cdot \vec{r})(\vec{\mu}_2 \cdot \vec{r})}{r^5} \quad [2.32]$$

where  $|\vec{r}|$  is the distance between  $\mu_1$  and  $\mu_2$ . The corresponding quantum-mechanical Hamiltonian is obtained by substituting  $\vec{\mu}_i = \gamma_i \hbar \vec{I}_i$ . For an isolated pair of spins, the dipolar Hamiltonian is<sup>45,51</sup>

$$H_D = \vec{I}_1 \cdot D \cdot \vec{I}_2 \quad [2.33]$$

$$D_{ij} = \omega_D \hbar \left( \delta_{ij} - \frac{3x_i x_j}{r^2} \right) \quad [2.34]$$

in which  $D_{ij}$  are the components of the Cartesian dipole coupling tensor and  $\omega_D = \frac{\gamma_1 \gamma_2 \hbar}{r^3}$  is the dipolar coupling constant. The Hamiltonian can be rewritten in terms of second rank irreducible tensors (Eq. 2.20), where the spin operators are

$$\begin{aligned} A_0^{(2)} &= \frac{1}{\sqrt{6}} (3I_z^{(1)} I_z^{(2)} - \vec{I}^{(1)} \cdot \vec{I}^{(2)}) \\ A_{\pm 1}^{(2)} &= \mp \frac{1}{2} (I_z^{(1)} I_{\pm}^{(2)} + I_{\pm}^{(1)} I_z^{(2)}) \\ A_{\pm 2}^{(2)} &= \frac{1}{2} I_{\pm}^{(1)} I_{\pm}^{(2)} \end{aligned} \quad [2.35]$$

and the space operators in the PAS are

$$T_0^{(2)}(PAS) = -\sqrt{6}\omega_D, \quad T_{\pm 1}^{(2)}(PAS) = T_{\pm 2}^{(2)}(PAS) = 0 \quad [2.36]$$

Note, that this is simpler than the quadrupole case because the asymmetry parameter for dipolar coupling is zero.

In a polycrystalline sample the orientation dependence of dipolar interaction result in a powder pattern spectrum observed in the laboratory frame

$$T_0^{(2)}(LAB) = D_{00}^{(2)}(\Omega_{PL})T_0^{(2)}(PAS) = -\frac{\sqrt{6}}{2}\omega_D(3\cos^2\beta_{PL} - 1) \quad [2.37]$$

In a system such as deuterated polyaniline, which was studied extensively in this work, one can consider dipolar coupling of deuterons with  $^{13}\text{C}$ ,  $^2\text{H}$ , and  $^1\text{H}$  nuclei. The typical distances between nuclei listed above are  $r_{DC} = 1.1 \times 10^{-10}$  m,  $r_{DD} = 2.5 \times 10^{-10}$  m, and  $r_{DH} = 3.0 \times 10^{-10}$  m respectively <sup>52</sup>. Since the natural abundance of  $^{13}\text{C}$  is 1.1%, the intensity arising from  $^2\text{H}$  coupled to  $^{13}\text{C}$  is negligible. The dipolar coupling constant,  $\omega_D$ , for deuteron - deuteron interactions at the distance given above is  $\sim 170$  Hz and for deuteron-proton interactions is  $\sim 68$  Hz. For a system of two deuterons the static Hamiltonian due to Zeeman, quadrupole and dipolar interactions is given by

$$H = -\omega_0(I_z^{(1)} + I_z^{(2)}) + \frac{1}{3}\omega_Q \left\{ 3[(I_z^{(1)})^2 + (I_z^{(2)})^2] - (I^{(1)})^2 - (I^{(2)})^2 \right\} + \omega_D(3I_z^{(1)}I_z^{(2)} - \vec{I}^{(1)} \cdot \vec{I}^{(2)}) \quad [2.38]$$

As shown in reference <sup>53</sup>, in such a system the biggest transition frequency due to the quadrupole interaction is equal to  $2\omega_Q$  ( $\sim 360$  kHz) and line splitting due to the dipolar term is  $6\omega_D$  ( $\sim 1$  kHz for deuteron - deuteron coupling). Therefore, the strength of inter-nuclear magnetic dipole coupling is two orders of magnitude less than the strength of electrical quadrupole coupling and can be safely ignored in the studied system.

Even though dipolar coupling between nuclear and electron magnetic moments produces a second-order perturbation effect in diamagnetic systems and is usually ignored in solid state NMR, in paramagnetic system, such as conductive polyaniline, this electron-nucleus coupling produces first-order perturbation effects and must be considered in detail. This is done in the next chapter.

## 2.2.4 HYPERFINE INTERACTIONS

The hyperfine interaction is that of the magnetic moment of the nucleus,  $\mu_n$ , with the magnetic field produced by electrons. The latter can originate either from the orbital motion of electrical charges (chemical shielding) or from the magnetic moment associated with unpaired electron spin.

### *a) Chemical shielding interaction*

The circulating electron charges establish a magnetic field that opposes the external field; thus, the electrons are said to shield the nucleus from the applied external field. Chemical shielding depends on the electronic current density in the vicinity of the nucleus. Since NMR frequencies depend on the strength of the applied magnetic field at the nucleus, chemical shielding results in different resonant frequencies for each chemically distinct nucleus in the sample.

For a particular nucleus, the size of chemical shift is proportional to the strength of the applied magnetic field. In order to be able to compare data collected using spectrometers operating at different fields, frequencies are expressed in dimensionless units, called parts per million (ppm). The chemical shift,  $\delta$ , is calculated as a ratio of

frequencies relative to some reference compound  $\delta = \frac{\nu - \nu_{ref}}{\nu_{ref}} \times 10^6$ . The deuteron

chemical shift range has a span of about 10 ppm for diamagnetic materials.

Chemical shielding is anisotropic. Empirically, it is described by a second rank tensor  $\sigma$ , and in general, can be decomposed into symmetric and anti-symmetric parts. The anti-symmetric part has negligible effect on NMR spectra<sup>54</sup>. The Hamiltonian for the chemical shielding interaction is

$$H_{SL} = -\gamma_n \hbar \vec{I} \cdot \vec{B}_{induced}(LAB) = \gamma_n \hbar \vec{I} \sigma(LAB) \vec{B}_0 \quad [2.39]$$

It can be rewritten in terms of the irreducible spherical tensor products according to equation 2.20,

$$\begin{aligned} A_0^{(0)} &= -\frac{1}{\sqrt{3}} \vec{I} \cdot \vec{B}, & A_0^{(1)} &= -\frac{i}{\sqrt{2}} (B_y I_x - B_x I_y), \\ A_{\pm 1}^{(1)} &= \frac{1}{2} (B_z I_x - B_x I_z \pm i(B_z I_y - B_y I_z)) \\ A_0^{(2)} &= \sqrt{\frac{2}{3}} \left( B_z I_z - \frac{1}{2} (B_x I_x + B_y I_y) \right), & [2.40] \\ A_{\pm 1}^{(2)} &= \mp \frac{1}{2} (B_x I_z - B_z I_x \pm i(B_y I_z + B_z I_y)), \\ A_{\pm 2}^{(2)} &= \frac{1}{2} (B_x I_x - B_y I_y \pm i(B_x I_y + B_y I_x)) \end{aligned}$$

The  $T$  components in the principal axis system, where  $\sigma$  is diagonal, can be written in terms of the characteristic chemical shielding parameters

$$\begin{aligned} T_0^{(0)}(PAS) &= -\sqrt{3} \sigma_{iso}, & \sigma_{iso} &= \frac{1}{3} Tr(\sigma), & \sigma_{33} &\geq \sigma_{22} \geq \sigma_{11} \\ T_0^{(1)}(PAS) &= T_{\pm 1}^{(1)}(PAS) = T_{\pm 1}^{(2)}(PAS) = 0 & [2.41] \end{aligned}$$

$$T_0^{(2)}(PAS) = \sqrt{\frac{3}{2}}(\sigma_{33} - \sigma_{iso}), \quad T_{\pm 2}^{(2)} = \frac{\eta}{2}(\sigma_{33} - \sigma_{iso}), \quad \eta = \frac{\sigma_{11} - \sigma_{22}}{\sigma_{33} - \sigma_{iso}}$$

Since the direction of the external field is usually chosen along z-axis in laboratory frame and since chemical shift is only a small perturbation of Zeeman Hamiltonian, to the first order the expression for  $H_{SL}$  then becomes

$$H_{SL}(LAB)/\hbar = A_0^{(0)}T_0^{(0)}(LAB) + A_0^{(2)}T_0^{(2)}(LAB) = \gamma_n I_z \sigma_{zz} B_0 \quad [2.42]$$

An expression for  $\sigma_{zz}$ , in terms of the principal values of the shielding tensor and the Euler angle transformation from the principal axis system to the laboratory frame is found by applying rotation operators to  $\sigma(PAS)$ <sup>46</sup>:

$$\begin{aligned} \sigma_{zz} &= \left[ R^{-1}(\alpha_{PL}, \beta_{PL}, \gamma_{PL}) \sigma(PAS) R(\alpha_{PL}, \beta_{PL}, \gamma_{PL}) \right]_{zz} = \\ &= \sigma_{11} \cos^2 \gamma \cdot \sin^2 \beta + \sigma_{22} \sin^2 \gamma \cdot \sin^2 \beta + \sigma_{33} \cos^2 \beta \end{aligned} \quad [2.43]$$

The NMR frequency of a nucleus, subject to the Zeeman and chemical shielding interactions, is given in the first order approximation by

$$\omega = \omega_0 (1 - \sigma_{zz}) \quad [2.44]$$

where  $\omega_0 = \gamma_n \hbar B_0$  is the Larmor frequency.

#### *b) Electron – nucleus spin interaction*

Some materials, including conductive polymers, can have localized unpaired electrons. Hyperfine coupling between the nucleus and the unpaired electron spin produces a so-called paramagnetic shift, which are comparable to or larger than the chemical shift discussed above.

In a metal, the conduction electrons are delocalized, so that a given nuclear spin experiences a magnetic coupling with many electrons. Therefore, the coupling to the electron spins must be averaged over the electron spin orientations. In the absence of an

external field, there is no preferential orientation for the electron spins, and thus there is zero average magnetic coupling to the nucleus. The application of a static magnetic field polarizes the electron spins. This gives rise to an observable Knight shift. This effect was named after Professor Walter Knight who first observed the phenomenon<sup>45</sup>.

While there are numerous similarities between the paramagnetic shift and the Knight shift of the nuclear resonance, there are fundamental differences. In a non-metallic substance with localized unpaired electrons, each nuclear spin “sees” the magnetic field of only one electron spin and it is permissible to replace this field by its time average over the very frequent electron spin flips, caused by exchange or very fast relaxation. In a metal, where the conduction electrons are not localized, each nuclear spin “sees” magnetic fields from all the electrons of the sample at the same time, and an average is the ensemble average.

The form of the Hamiltonian for dipolar coupling between magnetic moments of a nucleus and an electron is identical to equations 2.32 – 2.36 as long as nuclear and electron moments,  $\mu_n$  and  $\mu_e$ , are far enough apart.

$$H_d = \gamma_n \gamma_e \hbar^2 \left( \frac{(\vec{I} \cdot \vec{S})}{r^3} - 3 \cdot \frac{(\vec{I} \cdot \vec{r})(\vec{S} \cdot \vec{r})}{r^5} \right) \quad [2.45]$$

This holds for electronic wave functions of *p*-state, *d*-state, or other states of non-zero angular momentum. For *s* – states, however, the electron wave function is non-zero at the nucleus and the dipolar approximation breaks down. The interaction Hamiltonian for the nucleus and an electron can then be obtained using relativistic theory (Dirac equation)

45,50

$$H_F = \left( \frac{8\pi}{3} \right) \hbar^2 \gamma_n \gamma_e \delta(\vec{r} - \vec{r}_e) \vec{S} \cdot \vec{I} \quad [2.46]$$

where the term  $\delta(\vec{r} - \vec{r}_e)$  is the Dirac delta function, which is 1 for  $\vec{r} - \vec{r}_e = 0$  and zero otherwise ( $\vec{r}$  is the position of the nucleus of interest and  $\vec{r}_e$  is the position of a localized electron). The expectation value of the Hamiltonian  $H_F$ , can be written as  $I \cdot a \cdot S$ , where  $a = \left(\frac{8\pi}{3}\right) \hbar^2 \gamma_n \gamma_e |\psi(\vec{r})|^2$ ,  $|\psi(\vec{r})|$  is the amplitude of the electronic wave function at the nucleus, so that for  $|\psi(\vec{r})|$  to be non-vanishing the electron must have some probability of being at the nucleus. This is true only for electrons in  $s$ -states. This part of the Hamiltonian is called the Fermi contact term. The other portion of the hyperfine Hamiltonian, which includes dipolar coupling ( $\vec{I} \neq 0$ ) and chemical shielding is called pseudo-contact.

For a metallic sample the Fermi contact term of the Hamiltonian is simply

$$H_F = \left(\frac{8\pi}{3}\right) \hbar^2 \gamma_n \gamma_e \sum_j \delta(\vec{r} - \vec{r}_j) \vec{S}_j \cdot \vec{I} \quad [2.47]$$

where sum is over all unpaired electrons. The expectation value of the total electron – nucleus spin interaction is

$$\begin{aligned} \gamma_n \gamma_e \hbar^2 \sum_j \langle \psi_m^{(j)} | \left( \frac{(\vec{I} \cdot \vec{S}_j)}{r_j^3} - 3 \cdot \frac{(\vec{I} \cdot \vec{r}_j)(\vec{S}_j \cdot \vec{r}_j)}{r_j^5} + \frac{8\pi}{3} \delta(\vec{r}_j) \vec{S}_j \cdot \vec{I} \right) | \psi_m^{(j)} \rangle = \\ = \sum_j \vec{I} \cdot a_j \cdot \vec{S}_j \end{aligned} \quad [2.48]$$

Assuming that  $a_j$  is approximately the same for all the unfilled orbitals near the top of the Fermi distribution,  $\sum_j \vec{I} \cdot a_j \cdot \vec{S}_j = \vec{I} \cdot a \cdot \sum_j S_j = \vec{I} \cdot a \cdot \vec{S}$

The Hamiltonian can be rewritten as an irreducible spherical tensor products where

$$\begin{aligned}
A_0^{(0)} &= -\frac{1}{\sqrt{3}} \vec{I} \cdot \vec{S}, & A_0^{(1)} &= \frac{1}{2\sqrt{2}} (I_+ \mathbf{s}_- - I_- \mathbf{s}_+), & A_{\pm 1}^{(1)} &= \frac{1}{2} (I_Z \mathbf{s}_{\pm} - I_{\pm} \mathbf{s}_Z) \\
A_0^{(2)} &= \frac{1}{\sqrt{6}} (3I_Z \mathbf{s}_Z - \vec{I} \cdot \vec{S}), & A_{\pm 1}^{(2)} &= \mp \frac{1}{2} (I_Z \mathbf{s}_{\pm} + I_{\pm} \mathbf{s}_Z), & A_{\pm 2}^{(2)} &= \frac{1}{2} I_{\pm} \mathbf{s}_{\pm} \quad [2.50]
\end{aligned}$$

The  $T$  components in the principal axis system, where  $a$  is diagonal, can be written as

$$\begin{aligned}
T_0^{(0)}(PAS) &= -\sqrt{3} a_{iso}, \quad a_{iso} = \frac{1}{3} Tr(a), \quad a_{33} \geq a_{22} \geq a_{11} \\
T_0^{(1)}(PAS) &= T_{\pm 1}^{(1)}(PAS) = T_{\pm 1}^{(2)}(PAS) = 0 \quad [2.51] \\
T_0^{(2)}(PAS) &= \sqrt{\frac{3}{2}} (a_{33} - a_{iso}), \quad T_{\pm 2}^{(2)} = \frac{\eta}{2} (a_{33} - a_{iso}), \quad \eta = \frac{a_{11} - a_{22}}{a_{33} - a_{iso}}
\end{aligned}$$

In the equations above  $a_{kk} = \sum_j a_{kk}^{(j)}$ , where the sum is over all electrons. Tensor  $a$  is anisotropic and the Knight and paramagnetic shifts depend on the direction of the applied field with respect to the crystalline axis. Since the anisotropic internal field is much smaller than the applied field  $B_0$ , only its component parallel to  $B_0$  is effective in shifting the resonance frequency.

$$H_{en}(LAB)/\hbar = A_0^{(0)} T_0^{(0)}(LAB) + A_0^{(2)} T_0^{(2)}(LAB) = \gamma_n I_z a_{zz} B_0 \quad [2.52]$$

Component  $a_{zz}$  can be expressed via values of tensor  $a$  in the PAS and the Euler angles connecting the PAS and LAB systems <sup>46</sup>

$$a_{zz}(LAB) = a_{11} \cos^2 \gamma \cdot \sin^2 \beta + a_{22} \sin^2 \gamma \cdot \sin^2 \beta + a_{33} \cos^2 \beta \quad [2.53]$$

Development of a rigorous expression for the Knight shift is a formidable task not only for conductive polymers with intricate morphology but even for pure metals. Assuming that electrons in a metal are weakly interacting and can be described by Bloch

wave functions  $\psi_{\vec{k}s} = u_{\vec{k}}(\vec{r})e^{i\vec{k}\cdot\vec{r}}\psi_s$ , the Fermi contact interaction Hamiltonian can be written in a form <sup>45,50</sup>

$$H_{en} = -\gamma_n \hbar I_{nz} \frac{8\pi}{3} \left\langle |u_{\vec{k}}(0)|^2 \right\rangle_F \chi B_0 \quad [2.54]$$

where symbol  $\langle \rangle_F$  means that the average is evaluated over all orbits at the Fermi energy level and  $\chi$  is the total spin susceptibility of the electrons. According to the well-known Curie law, spin susceptibility is

$$\chi = \frac{\gamma^2 \hbar^2}{k_B T} \cdot \frac{I(I+1)}{3} \quad [2.55]$$

Substituting the value for the electron spin, one can obtain

$$\chi = \frac{\gamma_e^2 \hbar^2}{4k_B T} \quad [2.55a]$$

This value of susceptibility of bound electron should be contrasted with that of a free electron gas <sup>45,50,55</sup>,

$$\chi = \frac{3\gamma_e^2 \hbar^2}{2k_B T_F} = \gamma_e^2 \hbar^2 \frac{\rho(E_F)}{2} \quad [2.55b]$$

where  $T_F$  is the Fermi temperature, and  $\rho(E_F)$  is the density of states at the Fermi level. The susceptibility of conduction electrons is practically independent of the temperature, since the Fermi temperature is of the order of  $10^4$  to  $10^5$  K <sup>50,51</sup>. It may be worth pointing out that the two features, delocalization of spin orbitals, and small, temperature-independent susceptibility are not necessarily present simultaneously. Thus in semiconductors or conducting polymers, the conduction electrons can have their orbits spread over the entire sample but, because of their small number in the conduction band,

their distribution in energy among those orbits is described by Boltzmann statistics and their spins are not paired to the same extent as in metals.

The expression for the Fermi contact coupling (Eq. 2.54) is entirely equivalent to the interaction with an extra magnetic field  $\Delta B$ , which aids the applied field  $B_0$  and is given by

$$\frac{\Delta B}{B_0} = \frac{8\pi}{3} \left\langle |u_{\bar{k}}(0)|^2 \right\rangle_F \frac{\gamma_e^2 \hbar^2}{2} \rho(E_F) = \frac{8\pi}{3} \left\langle |u_{\bar{k}}(0)|^2 \right\rangle_F \chi \quad [2.56]$$

To summarize, the properties of the metallic Knight shift are:

- 1) it is typically positive;
- 2) it is proportional to applied field  $B_0$ ;
- 3) it is very nearly independent of temperature;
- 4) in general, since the larger- $Z$  atoms will have larger value of  $\left\langle |u_{\bar{k}}(0)|^2 \right\rangle_F$ , the Knight shift increases with increasing nuclear charge  $Z$ .

It was shown by Bloembergen<sup>56</sup> that the Knight shift for semiconductors is given by

$$\frac{\Delta B}{B_0} = \frac{8\pi}{3} \gamma_e^2 \hbar^2 \left\langle |u_{\bar{k}}(0)|^2 \right\rangle_{E_0} \frac{n_e}{k_B T} \quad [2.57]$$

where  $\left\langle \right\rangle_{E_0}$  is now to be evaluated near the bottom of the conduction band for electrons or the top of the valence band for holes and  $n_e$  denotes the temperature dependent number of electrons per unit volume in the conduction band.

## 2.3 MOTION AND RELAXATION

### 2.3.1 MOTION

One of the most important and useful features of NMR is its ability to probe molecular motion over a wide range of timescales. Motional processes can be detected by NMR if they produce changes in the nuclear spin Hamiltonian. The nature of motional effects depends on the type of motion and their timescale, which is summarized in Figure 2.2.

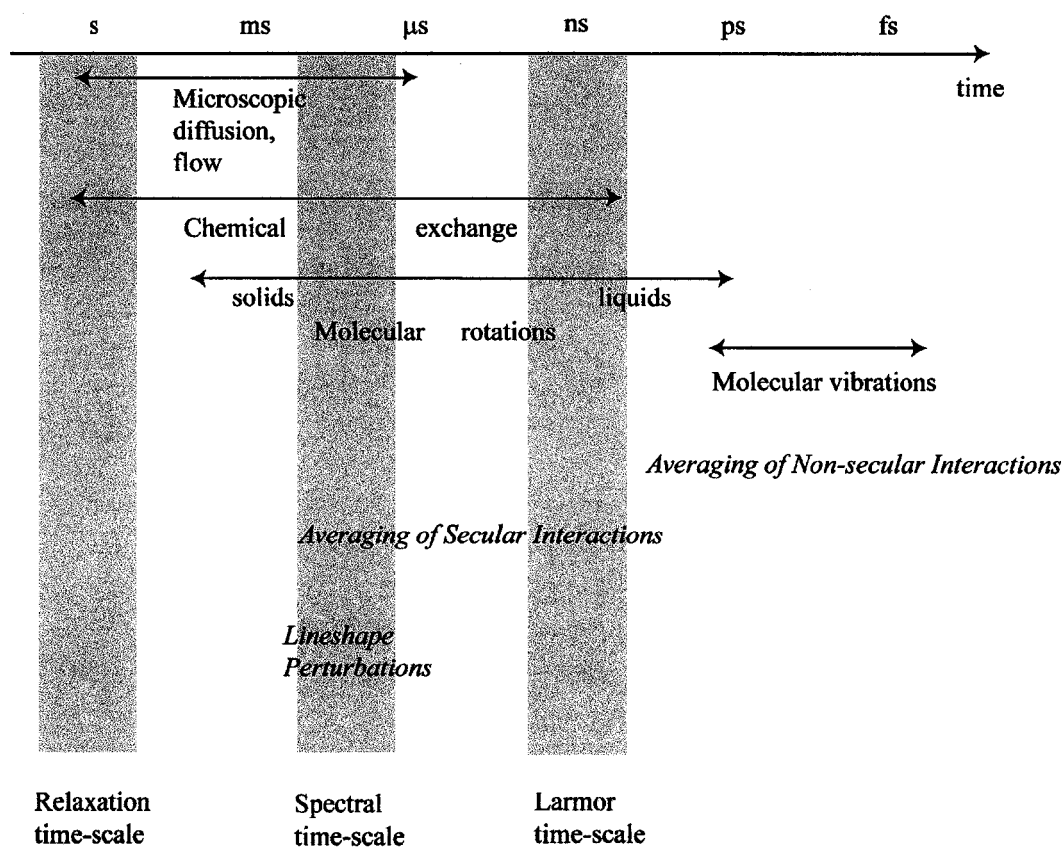
The effects of a motional process on nuclear spins depend on their relationship to three characteristic timescales, indicated in Figure 2.2 by vertical bars<sup>43</sup>. The Larmor timescale is roughly the time required for spins to precess through 1 radian in the magnetic field with characteristic time,  $\tau_0$ , given by  $|\omega_0\tau_0| \sim 1$ . The inverse of the spectral timescale represents the width of the NMR spectrum in absence of motion (in frequency units). For example, if a spin system contains two spins, with chemical shift frequencies  $\omega_a$  and  $\omega_b$ , then spectral timescale  $\tau_{spec}$  is given by  $|(\omega_a - \omega_b)\tau_{spec}| \sim 1$ . The relaxation timescale refers to the value of the spin-lattice relaxation time constant  $T_1$ , which for deuterons ranges between about 1 ms and several hundred seconds.

The effects of motion on the nuclear spin dynamics are represented in Figure 2.2 in *italic font*. The correct treatment of motional averaging depends on the relevant timescale of the process. Motions that are faster than the Larmor timescale (for example, vibrations) average the spin Hamiltonian before the secular approximation is made. Motions that are slower than Larmor timescale (for example, rotations) average the spin

Hamiltonian after the secular approximation. This distinction is important because relaxation processes are mainly caused by non-secular Hamiltonian terms, while the form of the NMR lineshape is determined by secular terms. This implies, for example, that if

FIGURE 2.2

## MOTIONAL TIMESCALES ASSOCIATED WITH DIFFERENT PHENOMENA



one wants to consider nuclear spin relaxation, it is important to correct the values of spin interaction parameters for rapid vibrational and librational motion, while no corrections should be made for slower rotational and translational motion.

For calculations of the NMR lineshape (as distinction from the relaxation behavior), it is appropriate to average the spin interactions over all motions that are faster than the spectral timescale. In this case, for a solid sample the Euler angles describing powder orientations are now time-dependent due to internal motion. In case of the quadrupole coupling, the averaged Hamiltonian experienced by spins is

$$\langle H_Q(LAB) \rangle_t = A_0^{(2)} \langle T_0^{(2)}(LAB) \rangle_t = A_0^{(2)} \sum_{k=-2}^2 \langle D_{0k}^{(2)}(\Omega_{PL}) \rangle_t T_k^{(2)}(PAS) \quad [2.58]$$

Invoking the ergodic hypothesis allows the replacement of the time averaged Wigner rotation matrix elements by their ensemble average (equivalent to a powder average) values for a model dependent geometry of motion:

$$\langle D_{ij}^{(2)}(\Omega_{PL}) \rangle_t = \langle D_{ij}^{(2)}(\Omega_{PL}) \rangle_{\Omega} = \int_0^{2\pi} d\alpha \int_0^{2\pi} d\gamma \int_0^{\pi} d\beta \cdot \sin\beta \cdot P(\Omega) \cdot D_{ij}^{(2)}(\Omega_{PL}) \quad [2.59]$$

Here  $P(\Omega)$  is a normalized probability of certain orientations,  $\Omega=(\alpha,\beta,\gamma)$ , defined by the motional model. For example, if a deuteron continuously librates in a cone with angle  $\beta_c$ , the observed quadrupolar frequencies will be modified by averaging  $H_Q$  with the uniform probability

$$P(\Omega) = \frac{1}{\int_0^{2\pi} d\alpha \int_0^{2\pi} d\gamma \int_0^{\beta_c} d\beta \cdot \sin\beta} = \frac{1}{4\pi^2(1 - \cos\beta_c)}, \quad 0 < \beta < \beta_c \quad [2.60]$$

$$P(\Omega) = 0, \quad \text{otherwise.}$$

So that

$$\begin{aligned} 2\Omega_Q &= \sqrt{6} \langle T_0^{(2)}(LAB) \rangle_{\Omega} = \\ &= \sqrt{6} \left( \langle D_{00}^{(2)}(\Omega_{PL}) \rangle_{\Omega} T_0^{(2)}(PAS) + \left[ \langle D_{0-2}^{(2)}(\Omega_{PL}) \rangle_{\Omega} + \langle D_{02}^{(2)}(\Omega_{PL}) \rangle_{\Omega} \right] T_{\pm 2}^{(2)}(PAS) \right) \quad [2.61] \end{aligned}$$

The ensemble averages of  $\langle D_{00}^{(2)}(\Omega_{PL}) \rangle_{\Omega}$  and  $\langle D_{0-2}^{(2)}(\Omega_{PL}) \rangle_{\Omega} + \langle D_{02}(\Omega_{PL}) \rangle_{\Omega}$  describing the molecular motion are:

$$\langle D_{00}^{(2)}(\Omega_{PL}) \rangle_{\Omega} = \frac{1}{2} \cos \beta_c (\cos \beta_c + 1) \quad [2.62]$$

$$\langle D_{0-2}^{(2)}(\Omega_{PL}) \rangle_{\Omega} + \langle D_{02}(\Omega_{PL}) \rangle_{\Omega} = 0$$

This means that in the LAB frame the motionally averaged asymmetry parameter is zero,  $\langle \eta \rangle = 0$ , and the averaged quadrupole splitting reduces to

$$2\Omega_Q = \frac{3}{4} \omega_Q \cdot \cos \beta_c (\cos \beta_c + 1), \quad [2.63]$$

In the case of jumps between discrete orientations, the integral 2.59 reduces to a sum. The difference in amplitude in the case of discrete jumps versus continuous motion can be derived<sup>57</sup>.

Motion on the spectral timescale,  $\tau_{spec}$ , causes the modulation of the NMR lineshape. For example, consider a two site exchange process, in which an isolated nuclear spin is transported between two different electronic environments,  $A$  and  $B$ , with different chemical shifts but identical free energy occupation probabilities at rate  $k$ . The chemical shift difference for the process is  $\omega_{\Delta} = \omega_A - \omega_B$ . If the exchange rate constant is smaller than the magnitude of  $\frac{\omega_{\Delta}}{2}$  (but still comparable in size to  $\omega_{\Delta}$ ), then no averaging occurs and two distinct lines are observed in the NMR spectrum. The full width at half height of each line is  $k/\pi$  Hertz<sup>58</sup>. When the spin makes a transition between the two states, its precession frequency suddenly changes. These unpredictable jumps in precession frequency lead to loss of phase coherence and enhance the decay of the total

transverse magnetization. An increase in the exchange rate thus leads to broadening of the spectral peaks. As  $k$  approaches  $\frac{\omega_{\Delta}}{2}$  the probability of random jumps between two sites during the experiment is spread over whole spectral range in a Gaussian-like manner and only one motionally broadened line, centered at the weighted average frequency, is observed. Finally, as the rate becomes larger than the static splitting,  $k > \frac{\omega_{\Delta}}{2}$ , the lines are completely averaged and collapse into a single sharp transition at the weighted average frequency. The width of the peak,  $\delta$ , is given by  $\delta = \frac{\omega_{\Delta}^2}{2k} \cdot p_A \cdot p_B$ , where  $p_i$  is the population of  $i$ -th site<sup>58</sup>. The theory, which has been briefly outlined above, is referred to in literature as motional narrowing theory.

A complete description of the time evolution of a spin system, accounting for spin dynamics in any motional regime, requires the evaluation of the stochastic Liouville-von Neumann equation<sup>59</sup>. Software package EXPRESS was used to calculate the quadrupole echo lineshapes and  $T_{1Z}$ ,  $T_{1Q}$  anisotropies of studied polymers<sup>60</sup>. This program solves the stochastic Liouville-von Neumann equation for the time evolution of the density matrix for a single deuteron:

$$\frac{d}{dt} \rho^*(t) = (i\Omega + R + K)[\rho^*(t) - \rho^*(\infty)] = L[\rho^*(t) - \rho^*(\infty)] \quad [2.64]$$

where  $\rho^*(\infty)$  is the equilibrium spin density matrix in the interaction representation<sup>45</sup>, denoted by a star superscript,  $\Omega = [\rho^*, \langle H_Q \rangle^*]$  is the diagonal operator of site frequencies,  $R = [\rho^*, H_1^*(t)]$  is a relaxation operator,  $K$  is a kinetic exchange matrix and

$L$  is the Liouville operator. Elements of matrix  $K$ ,  $k_{ij}$ , are the jump rates from site  $j$  to  $i$ , which satisfy the condition of detailed balance:

$$k_{ii} = -\sum_{i \neq j} k_{ij} \quad [2.65]$$

Assuming that a nucleus jumps instantaneously between  $N$  sites, defined by the orientation of principal axes system of the electric field gradient, the complete spin density superoperator is constructed as a direct product of the individual spin density matrices for each site. If only the time evolution is wanted, then it is not necessary to solve the complete stochastic Liouville equation. Only its sub-matrix  $M^+$  needs to be considered because only  $\rho_{12}$  and  $\rho_{23}$  give detectable transverse magnetization  $M^+(t) = \text{Tr}\{\rho(t)I^+\}$ . Accordingly, the equation for magnetization will be

$$\frac{d}{dt} M(t) = LM(t) \quad [2.66]$$

The formal solution is given by,

$$M(t) = e^{Lt} M(0) \quad [2.67]$$

When the site populations are not equal,  $K$  is not symmetric, but can be symmetrized after a diagonal similarity transformation<sup>59</sup>

$$\begin{aligned} K' &= U^{-1} K U \\ U_{ij} &= p_i^{1/2} \delta_{ij} \end{aligned} \quad [2.68]$$

where  $p_i$  is the population of site  $i$ . The symmetric matrix  $L$ , then, has orthogonal eigenvectors written as columns in the matrix  $X$ , and its eigenvalues,  $\lambda$ , can be found numerically:

$$\lambda = X^{-1} U^{-1} L U X \quad [2.69]$$

Using these eigenvectors and eigenvalues, the solution to Eq. 2.67 is,

$$M(t) = UXe^{At}X^{-1}U^{-1}M(0) \quad [2.70]$$

This solution can be used to evaluate the time evolution of  $M$  between pulses in a generic multipulse NMR experiment. The effect of pulses can be included as boundary conditions for successive time intervals. The pulse sequences used in the present study have been discussed in Chapter 3. The software package EXPRESS is capable of modeling multi-axis jump motions for a sequence up to four “jumping frames”.

### 2.3.2 MAGIC ANGLE SPINNING

In liquids, anisotropic interactions are averaged by fast random tumbling of molecules. In solids, where molecular rotations are strongly restricted, it is possible to influence the NMR spectrum by mechanical rotation of the whole sample about a special axis, whose “magic” properties of averaging the second rank spherical tensor interactions are realized by imparting an appropriate periodic time dependence to the spatial components of the interaction Hamiltonians. Magic angle spinning (MAS) is a method used to increase resolution in solid state NMR by selective averaging of the anisotropic interactions. If the sample is spun rapidly about an axis oriented at the angle  $\theta = \text{arcCos}\left(\frac{1}{\sqrt{3}}\right) = 54.74^\circ$  with respect to the external magnetic field, all second rank anisotropic interactions are averaged, giving a high resolution, “liquid-like” spectra<sup>54</sup>.

For studies of conductive polymers, the static interactions Hamiltonian can be generalized as  $H = A_0^{(0)}T_0^{(0)}(LAB) + A_0^{(2)}T_0^{(2)}(LAB)$ . The first term is present only for

hyperfine interactions. Since this term is invariant to coordinate transformations ( $D_{00}^{(0)} = 1$ ), the effect of MAS on all static interactions Hamiltonians in the LAB frame can be derived from the other term,  $T_0^{(2)}(LAB)$ .

Components of  $T_0^{(2)}(LAB)$  can be calculated by transforming the coordinate system from the principal axis system (PAS) to a frame fixed in the rotor (ROT):

$$PAS \xrightarrow{\Omega_{PR}} ROT \xrightarrow{\Omega_{RL}} LAB$$

Here  $\Omega_{PR} = (0, \beta, \gamma(t))$  and  $\Omega_{RL} = (0, \theta, 0)$ . “Active” rotation<sup>46</sup> of the rotor is described by angle  $\alpha(t)$  around the rotor axis. This coordinate transformation is “passive” in the sense of Rose<sup>61</sup>, so that  $\gamma(t)$  should be considered instead. Angles  $\gamma(t)$  and  $\beta$  describe the PAS orientation of interaction tensors within the rotor. The time dependence of the azimuthal angle is  $\gamma(t) = \phi + \omega_r t$ , where  $\omega_r = 2\pi/\tau_r$  is the rotor frequency. Due to cylindrical symmetry of the system,  $\alpha$  is irrelevant. In the laboratory frame the rotor z-axis is oriented at the magic angle  $\theta$  with respect to the external field. The set of Wigner transformations for  $T_0^{(2)}(LAB)$  is given by

$$T_0^{(2)}(LAB) = \sum_{k=-2}^2 D_{k0}^{(2)}(\Omega_{RL}) \sum_{p=-2}^2 D_{pk}^{(2)}(\Omega_{PR}) T_p^{(2)}(PAS) \quad [2.71]$$

Due to the symmetry of quadrupole, dipolar and hyperfine interactions  $T_{\pm 1}^{(2)} = 0$ . This allows for simplification:

$$\begin{aligned} T_0^{(2)}(LAB) &= T_2^{(2)}(PAS) \sum_{k=-2}^2 D_{k0}^{(2)}(\Omega_{RL}) (D_{-2k}^{(2)}(\Omega_{PR}) + D_{2k}^{(2)}(\Omega_{PR})) + \\ &+ T_0^{(2)}(PAS) \sum_{k=-2}^2 D_{k0}^{(2)}(\Omega_{RL}) D_{0k}^{(2)}(\Omega_{PR}) \end{aligned} \quad [2.72]$$

Substitution of Wigner matrix elements and utilization of their symmetry properties <sup>49</sup>

helps to factor out the time dependent terms of  $T_0^{(2)}(LAB)$ :

$$T_0^{(2)}(LAB) = T_0^{(2)}(PAS) \frac{1}{2} A(\beta, \gamma(t)) + T_2^{(2)}(PAS) \frac{1}{\sqrt{6}} B(\beta, \gamma(t))$$

$$A(\beta, \gamma(t)) = \sin^2 \beta \cos 2(\phi + \omega_r t) - \sqrt{2} \sin 2\beta \cos(\phi + \omega_r t) \quad [2.73]$$

$$B(\beta, \gamma(t)) = \cos 2(\phi + \omega_r t) + \cos^2 \beta \cos 2(\phi + \omega_r t) + \sqrt{2} \sin 2\beta \cos(\phi + \omega_r t)$$

Thus, all the Hamiltonians are periodically modified by  $\omega_r t$ , so that  $H(t=0) = H(t = n\tau_r)$ , for any number of rotor periods,  $n$ . In other words, each interaction will be refocused once per rotor period. In general, this leads to rotational sidebands (at the multiples of the rotor frequency) in the Fourier transformed spectra. The intensity distribution among the spinning sidebands will depend on spin rate. Since the total intensity of the observed nucleus is conserved, the smaller the number of sidebands, the higher their intensity and the sensitivity. Imprecise setting of the magic angle will cause deviations from Eq. 2.73 and broadening of the spinning side bands. This can be used for precise experimental setting of  $\theta$ , by adjusting the angle until the narrowest line width is achieved.

For each specific interaction in Eq. 2.17, the corresponding MAS Hamiltonian can be easily written. For quadrupole and electron-nucleus spin interaction the explicit form of MAS Hamiltonians are

$$H_Q = \frac{\omega_Q}{8} (3I_z^2 - \vec{I} \cdot \vec{I}) \left( A(\beta, \gamma(t)) + \frac{\eta}{3} B(\beta, \gamma(t)) \right)$$

$$H_{en} = \vec{I} \cdot \vec{S} \cdot \mathbf{a}_{iso} + (3I_z S_z - \vec{I} \cdot \vec{S}) \frac{a_{33} - a_{iso}}{4} \left( A(\beta, \gamma(t)) + \frac{\eta}{3} B(\beta, \gamma(t)) \right)$$

### 2.3.3 RELAXATION

If a sample is allowed to be undisturbed for a long time in the magnetic field, it reaches a state of thermal equilibrium. This means that all coherences in the sample are zero and the populations are given by the Boltzmann distribution. Application of a radio-frequency pulse disturbs the equilibrium: populations deviate from their thermal equilibrium values, and in many cases, coherences are created.

The study of nuclear spin relaxation is a valuable tool because relaxation processes are sensitive to non-secular part of interaction Hamiltonians, which have little influence on ordinary NMR spectra, so that they cannot be revealed by studying NMR lineshapes.

Relaxation is a process by which thermal equilibrium is reestablished, through interaction of the spin with the thermal molecular environment. Relaxation processes may be divided roughly into two types. Spin lattice relaxation (or longitudinal relaxation) is concerned with the return of spin populations back to their Boltzmann distribution values. Spin-spin relaxation (or transverse relaxation) is concerned with the decay of coherences.

#### *a) Spin-lattice relaxation, $T_1$*

When a quantum mechanical system placed in external magnetic field, a bulk magnetization is created due to the Boltzmann distribution favoring population of magnetic moments parallel to the field (see section 3.3). This implies that the probability of transition to the upper state is smaller than that to the lower state. This seems to contradict a famous formula from time - dependent perturbation theory for the probability

per second,  $P_{a \rightarrow b}$ , that an interaction  $V(t)$  induces a transition from state  $a$  with energy  $E_a$  to state  $b$  whose energy is  $E_b$ :

$$P_{a \rightarrow b} = \frac{2\pi}{\hbar} |(b|V|a)|^2 \delta(E_a - E_b - \hbar\omega) \quad [2.74]$$

Since  $|(b|V|a)|^2$  equals  $|(a|V|b)|^2$ , the probability of transitions from state  $a$  to  $b$  is equal to probability of transition from state  $b$  to  $a$ .

The resolution of this paradox is that the thermal transition requires not only a spin coupling but also another system (“lattice”) in an energy state that permits this transition<sup>45</sup>. In thermal equilibrium the nuclear spin levels will have the same relative populations as do those of the lattice. Phenomenologically, the rate of change of the population difference,  $n$ , between two states is<sup>45</sup>

$$\frac{dn}{dt} = \frac{n_0 - n}{T_1} \quad [2.75]$$

where  $n_0$  is equilibrium population difference and  $T_1$  is a characteristic time associated with the approach to equilibrium, called the spin-lattice relaxation time. The solution of this equation is  $n = n_0 + Ae^{-t/T_1}$ . For two-level system (spin =  $1/2$ ), one can recognize that magnetization along the external field,  $M_z$ , is proportional to  $n$ , so that Equation 2.75 can be rewritten as

$$\frac{dM_z}{dt} = \frac{M_0 - M_z}{T_1} \quad [2.76]$$

where  $M_0$  is the thermal equilibrium magnetization.

b) *Transverse relaxation,  $T_2$*

A different relaxation phenomenon simply expresses the fact that in thermal equilibrium, under a static field the magnetization  $\vec{M}$  is parallel to  $\vec{B}_0$ . That is, the  $x$ - and  $y$ -components must vanish. Mathematically this can be expressed as

$$\begin{aligned}\frac{dM_x}{dt} &= -\frac{M_x}{T_2} \\ \frac{dM_y}{dt} &= -\frac{M_y}{T_2}\end{aligned}\tag{2.77}$$

The characteristic time  $T_2$  is called transverse relaxation time. For solids, it is usually much smaller than spin-lattice relaxation time.

c) *Redfield theory: a microscopic theory of  $T_1$  and  $T_2$*

Spin relaxation is caused by randomly fluctuating magnetic fields at the site of the nucleus. As described in section 2.1.2 the Hamiltonian can be written as  $H = H_0 + H_1(t)$ , where  $H_0$  is time independent term and  $H_1(t)$  fluctuates at random with the average value  $\langle H_1(t) \rangle = 0$ . To define how rapidly  $H_1$  fluctuates, the “correlation function”,  $G_{\alpha\beta\alpha'\beta'}(\tau)$ , is introduced

$$G_{\alpha\beta\alpha'\beta'}(\tau) = \langle (\alpha|H_1(t)|\beta)(\beta'|H_1(t+\tau)|\alpha') \rangle\tag{2.78}$$

For the time less than some critical time  $\tau_c$ , called the “correlation time”, the motion may be considered negligible, so that  $H_1(t) \approx H_1(t+\tau)$ . If the interval  $\tau$  is long compared to the time-scale of fluctuations or  $\tau_c$ , then system loses its “memory”,  $H_1(t+\tau)$  becomes progressively less correlated to  $H_1(t)$  and  $G_{\alpha\beta\alpha'\beta'}(\tau)$  dies to zero.

In relaxation theory an important role is played by the spectral density,  $J_{\alpha\beta\alpha'\beta'}(\omega)$ , defined as the Fourier transform of the correlation function<sup>43,45</sup>:

$$J_{\alpha\beta\alpha'\beta'}(\omega) = \int_{-\infty}^{\infty} G_{\alpha\beta\alpha'\beta'}(\tau) e^{-i\omega\tau} d\tau \quad [2.79]$$

If the Hamiltonian fluctuates rapidly, the characteristic time-scale for the motion is short, and the spectral density is broad; vice versa if the Hamiltonian fluctuates slowly, the fluctuation time-scale is long, and the spectral density function is narrow.

The time average of the derivative of the density matrix in equation 2.16 can be written as

$$\frac{d\rho^*(t)}{dt} = \frac{i}{\hbar} [\rho^*(0), H_1^*(t)] - \frac{1}{\hbar^2} \int_0^t dt' \left[ [\rho^*(0), H_1^*(t')] \right] H_1^*(t) \quad [2.80]$$

To evaluate this time-average, it is necessary to make an approximation. The theory developed on the following basic assumptions is due to A. G. Redfield <sup>45</sup>:

There exists a time  $t$  such that

- 1) the Hamiltonian  $H_I(t)$  fluctuates rapidly over all possible values

but

- 2)  $t$  is short enough, so that  $\rho^*(0)$  does not differ much from  $\rho^*(t)$ .

Based on the above statement, only the second term in equation 2.80 contributes to the time evolution of the density matrix; higher order terms in the successive approximation series can be ignored; it is permissible to substitute the upper integration limit  $t$  by infinity and  $\rho^*(0) \rightarrow \rho^*(t)$ .

Thus, in the Redfield limit equation 2.80 simplifies to

$$\frac{d\rho^*(t)}{dt} = -\frac{1}{\hbar^2} \int_0^{\infty} dt' \left[ [\rho^*(t), H_1^*(t')] \right] H_1^*(t) \quad [2.81]$$

Evaluation of this equation yields <sup>45,60</sup>:

$$\frac{d\rho_{\alpha\alpha'}^*(t)}{dt} = \sum_{\beta, \beta'} R_{\alpha\alpha'\beta\beta'} e^{i(\omega_\alpha - \omega_\beta + \omega_{\beta'} - \omega_{\alpha'})t} \rho_{\beta\beta'}^* \quad [2.82]$$

This is a set of linear differential equations for the elements of the density matrix <sup>60</sup>. Because the exponential factor in this equation, the non-secular terms (where  $\omega_\alpha - \omega_\beta \neq \omega_{\alpha'} - \omega_{\beta'}$ ) are insignificant <sup>45,60</sup>. Thus, Redfield's equation can be reduced further to

$$\frac{d\rho_{\alpha\alpha'}^*(t)}{dt} = \sum_{\beta, \beta'} R_{\alpha\alpha'\beta\beta'} \rho_{\beta\beta'}^* \quad [2.83]$$

The elements of Redfield operator,  $R_{\alpha\alpha'\beta\beta'}$ , are given by <sup>45,60</sup>

$$R_{\alpha\alpha'\beta\beta'} = \frac{1}{2\hbar^2} \left( \begin{array}{l} J_{\alpha\beta\alpha'\beta'}(\omega_{\alpha'} - \omega_{\beta'}) + J_{\alpha\beta\alpha'\beta'}(\omega_\alpha - \omega_\beta) - \delta_{\alpha'\beta'} \sum_\gamma J_{\gamma\beta\gamma\alpha}(\omega_\gamma - \omega_\beta) - \\ - \delta_{\alpha\beta} \sum_\gamma J_{\gamma\alpha'\gamma\beta'}(\omega_\gamma - \omega_{\beta'}) \end{array} \right) \quad [2.84]$$

#### d) Characteristic relaxation times for deuteron NMR

For an ensemble of isolated spin 1/2 nuclei, there are only two time constants for relaxation: the spin-lattice relaxation time constant  $T_1$  for the equilibration of populations and the spin-spin relaxation time constant  $T_2$  for the decay of single-quantum coherences. In systems of coupled spins and/or single spins greater than 1/2, one needs more time constants to fully characterize the relaxation.

For deuterons, three different relaxation time constants are usually studied <sup>53</sup>:

- 1) relaxation time of Zeeman order  $T_{1Z}$ , which describes the time evolution of the z-component of the magnetization vector  $\langle M_z(t) \rangle \propto \langle I_z(t) \rangle = \text{Tr}(\rho(t)I_z) = \rho_{11} - \rho_{33}$ ;
- 2) quadrupolar order <sup>49</sup> relaxation  $\langle Q_z \rangle = \text{Tr}(\rho(t)Q_z) = \rho_{11} - 2\rho_{22} + \rho_{33}$ ;
- 3) transverse relaxation  $\langle M_-(t) \rangle \propto \langle I_-(t) \rangle = \text{Tr}(\rho(t)I_-) = \sqrt{2}(\rho_{12} + \rho_{23})$ .

If the quadrupolar Hamiltonian is represented in terms of second rank irreducible spherical tensors (Eq. 2.20), it is possible to calculate explicit forms of the relaxation times<sup>59,60</sup>. Spectral density  $J_{\alpha\beta\alpha'\beta'}(\omega)$  given in equation 2.79 can be expressed as

$$J_{\alpha\beta\alpha'\beta'}(\omega) = (T_0^{(2)}(PAS))^2 \sum_{m=-2}^2 \langle \alpha | A_{-m}^{(l)} | \beta \rangle \langle \alpha' | A_{-m}^{*(l)} | \beta' \rangle \cdot j_m(m\omega) \quad [2.85]$$

$$j_m(m\omega) = (T_0^{(2)}(PAS))^{-2} \int_0^\infty T_m^{(l)}(LAB, t) T_m^{(l)}(LAB, t + \tau) e^{-i\omega\tau} d\tau \quad [2.86]$$

where  $j_m(m\omega)$  is the reduced spectral density. When the conditional probability,  $P(\Omega_0, \Omega, \tau = t - t_0)$ , of the system having orientation  $\Omega_0 = (\alpha_0, \beta_0, \gamma_0)$  at time  $t_0$  and orientation  $\Omega = (\alpha, \beta, \gamma)$  at time  $t$ , is specified by the motional model, the ensemble average of the correlation function (Eq. 2.84) can be calculated in terms of Wigner rotation matrix elements

$$\begin{aligned} \langle T_m^{(l)}(LAB, t) T_m^{(l)}(LAB, t + \tau) \rangle &= \\ &= \sum_{k=-2}^2 T_k^{(l)}(PAS) T_k^{(l)}(PAS) \cdot \int_{\Omega_0} P(\Omega_0) D_{km}^{(2)}(\Omega_0) d\Omega_0 \int_{\Omega} P(\Omega_0, \Omega, \tau) D_{km}^{(2)}(\Omega) d\Omega \end{aligned} \quad [2.87]$$

Using the spectral densities (Eq. 2.85, 2.86), Redfield coefficients  $R_{\alpha\alpha'\beta\beta'}$  can be evaluated (Eq. 2.84). The corresponding relaxation time constants are then

$$T_{12}^{-1} = R_{1122} + 2R_{1133} = \frac{3\pi^2}{2} \chi^2 (j_1(\omega_0) + 4j_2(2\omega_0)) \quad [2.88]$$

$$T_{1Q}^{-1} = 3R_{1122} = \frac{9\pi^2}{2} \chi^2 j_1(\omega_0) \quad [2.89]$$

Analytical calculations of relaxation time anisotropies for a given motional model (Eq. 2.88 and 2.89) can be compared with experimentally measured rate constants. The

motional model is validated by adjusting its parameters until they produce the best fit to the experimental data.

*e) Relaxation of nuclei in metals*

It is convenient to use another technique for computing  $T_1$  in metals, called the “spin temperature” approach<sup>45,62</sup>. This method is appropriate when the coupling of the nuclei with one another or coupling of the nuclei to the spin magnetic moments of the conduction electrons is much stronger than with the lattice. The strong coupling establishes a common temperature,  $T$ , for the spins, and coupling with the lattice, which has temperature  $T_L$ , causes this temperature to change<sup>45,62</sup>:

$$\frac{d\beta}{dt} = \frac{\beta_L - \beta}{T_1} \quad [2.90]$$

$$\beta = \frac{1}{kT} ; \quad \beta_L = \frac{1}{kT_L}$$

It can be shown that the spin-lattice relaxation rate for this model obeys

$$\frac{1}{T_1} = \frac{1}{2} \frac{\sum_{m,n} W_{mn} (E_m - E_n)^2}{\sum_n E_n^2} \quad [2.91]$$

here  $W_{mn}$  is the probability per second that the lattice induces a transition of the system from state  $m$  with energy  $E_m$  to state  $n$  with energy  $E_n$  (thus  $n$  designates a state of the total system, rather than the energy of a single spin).

From quantum mechanics it follows<sup>45,47,63</sup> that the probability of transition from the initial state  $|mks\rangle$  to the final state  $|nk's'\rangle$  (denoting nuclear quantum numbers  $m$  and  $n$  and electron transitions from state of wave vector  $\vec{k}$  and spin orientation  $s$  to a state  $\vec{k}', s'$ ) is

$$W_{mks, nk's'} = \frac{2\pi}{\hbar} \sum_{\substack{ks\text{-occupied} \\ k's'\text{-unoccupied}}} \left| \langle m\bar{k}s | H_F | n\bar{k}'s' \rangle \right|^2 \delta(E_m + E_{ks} - E_n - E_{k's'}) \quad [2.92]$$

The operator  $H_F$  is given by the equation 2.47 and summation restriction on  $ks$  and  $k's'$  can be removed by introducing the Fermi function  $f(\bar{k}, s)$  for the ensemble of electrons, then  $W_{mn} = \sum W_{mks, nk's'} \cdot f(\bar{k}, s) \cdot [1 - f(k', s')]$ . In the approximation that the wave

function can be written as  $|m\bar{k}s\rangle = |m\rangle|s\rangle u_{\bar{k}}(\vec{r})e^{i\vec{k}\vec{r}}$ , the transition probability is <sup>45,62</sup>

$$\begin{aligned} W_{mn} &= \frac{64}{9} \pi^3 \hbar^3 \gamma_e^2 \gamma_n^2 \sum_{\alpha} \left| \langle m | I_{\alpha} | n \rangle \right|^2 \int \left\langle |u_{\bar{k}}(0)|^2 \right\rangle_F^2 \rho^2(E) f(E) [1 - f(E)] dE = \\ &= \frac{64}{9} \pi^3 \hbar^3 \gamma_e^2 \gamma_n^2 \left\langle |u_{\bar{k}}(0)|^2 \right\rangle_F^2 \rho^2(E_F) kT \sum_{\alpha} \left| \langle m | I_{\alpha} | n \rangle \right|^2 \end{aligned} \quad [2.93]$$

here symbol  $\langle \rangle_F$  means that the average is evaluated over all orbits at the Fermi energy level,  $\rho(E_F)$  is density of states at the Fermi level and the notation  $f(\bar{k}, s)$  means

$$f(E) = \frac{1}{e^{\frac{E-E_F}{k_B T}} + 1}, \text{ where } E \text{ is the energy of an electron with the wave vector } \bar{k} \text{ and spin}$$

coordinate  $s$ . Utilizing equation 2.91, spin-lattice relaxation time is then

$$\frac{1}{T_1} = \frac{64}{9} \pi^3 \hbar^3 \gamma_e^2 \gamma_n^2 \left\langle |u_{\bar{k}}(0)|^2 \right\rangle_F^2 \rho^2(E_F) kT \quad [2.94]$$

The quantity  $\left\langle |u_{\bar{k}}(0)|^2 \right\rangle_F^2$  appearing in the expression also occurred in the equation 2.56 for the Knight shift. One can therefore substitute it and use the formula<sup>45</sup> for spin susceptibility of a Fermi gas of non-interacting spins to show

$$T_1 \left( \frac{\Delta B}{B_0} \right)^2 = \frac{\hbar}{4\pi kT} \cdot \frac{\gamma_e^2}{\gamma_n^2} \quad [2.95]$$

Equation 2.95 is commonly known as the Korringa relation, after Dr. J. Korringa who first published it.

One can calculate the transition probability  $W_{mn}$  and, consequently the  $T_1$  relaxation time, for semiconductors. Electrons in the conduction band and holes in the valence band of a semiconductor may be looked upon as a Maxwell-Boltzmann gas<sup>64</sup>. The distribution function, then, in the integral in Eq. 2.93 is  $f(E) = e^{-(E-E_F)/k_B T}$ . Also, in the high energy approximation ( $E - E_f \gg k_B T$ ) the probability  $1 - f(E)$  of finding a free electron or a hole state is practically equal to unity. The density of the electron states in the conduction band is given by<sup>63,64</sup>

$$\rho(E) = \frac{1}{2\pi} \left( \frac{2m_e}{\hbar^2} \right)^{3/2} (E - E_g)^{1/2} \quad [2.96]$$

where  $m_e$  denotes the effective mass of an electron, top of the valence band chosen as the origin ( $E = 0$ ) while the bottom of the conduction band labeled  $E = E_g$ . Using all of the above one can obtain

$$\frac{1}{T_1} = \frac{128}{9} \cdot \frac{\gamma_e^2 \gamma_n^2}{\hbar^3 \pi} \left\langle |u_{\vec{k}}(0)|^2 \right\rangle_{E_0}^2 m_e^3 (kT)^2 e^{-\frac{(E_g - E_F)}{k_B T}} \quad [2.97]$$

where  $\langle \rangle_{E_0}$  is now to be evaluated near the bottom of the conduction band for electrons or the top of the valence band for holes. Equation [2.97] valid for any (pure or doped) semiconductor. It is well known the Fermi energy and therefore the explicit temperature dependence of  $T_1$  varies strongly with the concentration of donors or acceptors.

## 2.4 POLARONS AND BIPOLARONS

Organic conjugated polymers are typically either insulators or semi-conductors and have a band gap larger than  $\sim 1.5 \text{ eV}$ <sup>29</sup>. Two processes can affect the conductivity of these polymers known as redox and protonic “doping”. Even though the term “doping” can be sometimes misleading, the term is widely used in the literature in analogy with the impurity doping of inorganic semi-conductors.

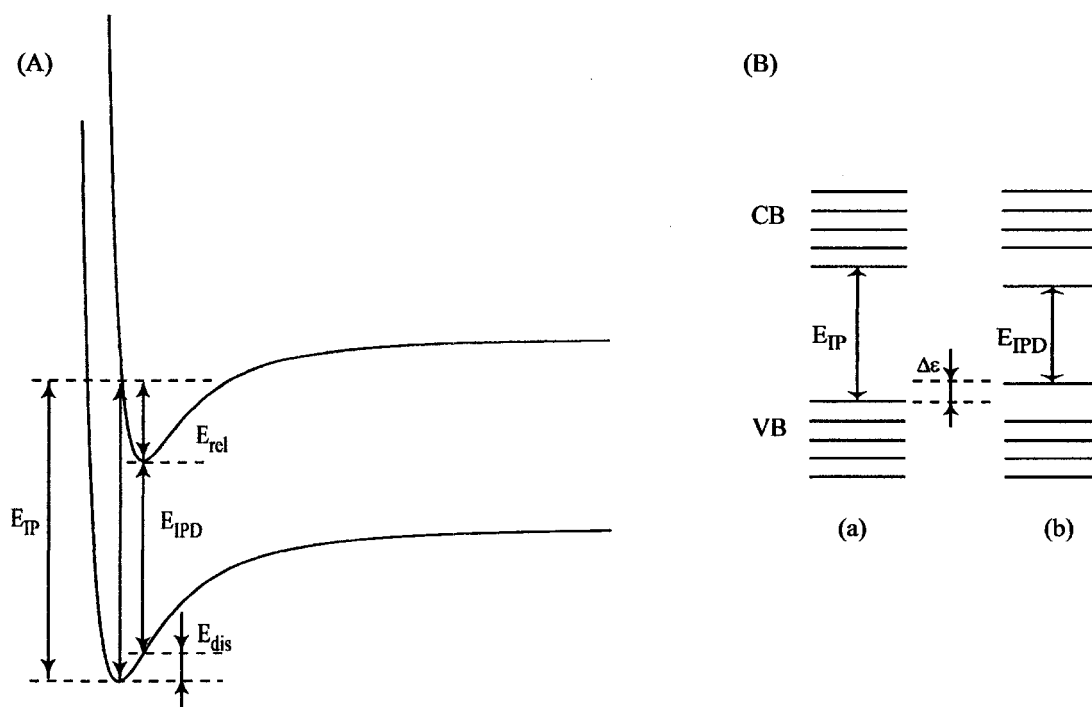
Initially, the high conductivity increase observed upon doping of organic polymers was thought to result from the formation of filled (donors) or unfilled (acceptors) electronic bands in the gap, in analogy to the mechanism of generation of charge carriers in inorganic semi-conductors. This assumption was, however, quickly challenged by the discovery that polyacetylene, polyparaphenylene and polypyrrole can display conductivity, which does not seem to be associated with unpaired electrons but rather with spinless charge carriers<sup>29</sup>.

In organic molecules, it is usually the case that the equilibrium geometry in the ionized state is different from that in the ground state<sup>29</sup>. The energies involved in the ionization process are schematically depicted in figure 2.3. A vertical ionization process costs energy  $E_{IP}$ . If geometry relaxation takes place in the ionized state, we gain back relaxation energy  $E_{rel}$ . Conceptually, going from the ground state to the relaxed ionized state can also be thought of in the following way. The geometry of the molecule is first distorted in the ground state in such a way that the molecule adopts the equilibrium geometry of the ionized state. This costs distortion energy  $E_{dis}$ . If one considers the one-electron energy levels of the molecule, the distortion leads to an upward shift of the top

level of the conduction band and downward shift of the lowest level of the valence band. If we then proceed to the ionization of the distorted molecule, it requires energy  $E_{IPD}$  (Figure 2.3).

FIGURE 2.3

## ILLUSTRATION OF A MOLECULAR IONIZATION PROCESS ENERGIES



(A) Illustration of energies involved in a molecular ionization process.  $E_{IP}$  is the vertical ionization energy,  $E_{rel}$  is the relaxation energy gained in the ionized state,  $E_{dis}$  is the distortion energy to be paid in the ground state in order for the molecule to adopt the equilibrium geometry of the ionized state, and  $E_{IPD}$  is the ionization energy of the distorted molecule. (B) Schematic illustration of the electron energy levels: (a) the equilibrium geometry of the ground state; (b) the equilibrium geometry of the first ionized state.

From Figure 2.3 it is clear that it is energetically favorable to have a geometry distortion when the quantity  $E_{IP} - E_{IPD}$  ( $= \Delta\varepsilon$ ) is larger than the distortion energy  $E_{dis}$ . In a polymer or any solid, a vertical ionization process  $E_{IP}$  results in creation of a hole on the top of the valence band. In this case no geometry relaxation takes place, the positive charge is delocalized on the chain and the presence of the hole on the top of the valence band leads to the metallic character. This situation corresponds to the initial assumption about the mechanism of conduction in doped organic polymers.

However, as discussed previously, in organic polymers, it can be energetically favorable to localize the charge that appears on the chain, and to have a local distortion of the lattice around the charge. This process causes the presence of localized electronic states in the gap due to an upward shift  $\Delta\varepsilon$  of the top level of the conduction band and downward shift of the lowest level of the valence band. These states are called polaron states and the electric charge associated with such a lattice distortion is called a polaron. Theoretical calculations, based on Huckel theory, have been conducted for different conductive polymers<sup>29</sup>. This study indicated that polaron formation is generally energetically favorable in organic conjugated polymers.

What happens when a second electron is removed from the polymer chain? Is it more favorable to take the second electron from the polaron or from somewhere else on the chain? In the former case, a bipolaron is formed. A bipolaron is defined as a pair of like charges associated with a strong lattice distortion. The formation of a bipolaron implies that the energy gained by the interaction with the lattice is larger than the Coulomb repulsion between the two charges of the same sign in the same location. The bipolaron is spinless<sup>29</sup>. The question of bipolaron formation versus creation of two

polarons depends on properties of the polymer and should be considered on individual basis. Removal of more electrons from the polymer chain leads to the formation of polaron or bipolaron energy bands<sup>29</sup>.

## CHAPTER 3

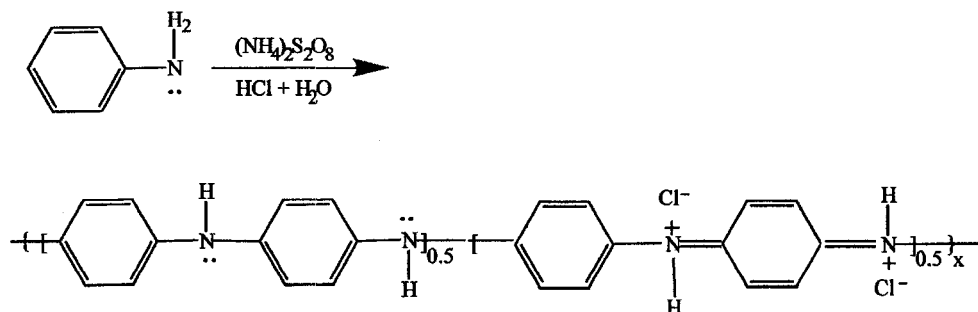
### EXPERIMENTAL METHODS

#### 3.1 MATERIAL PREPARATION

Polyaniline was synthesized by a method similar to a literature procedure<sup>65</sup>. Starting materials for polymer synthesis were obtained from Aldrich Chemical Co. and used as received, except for aniline, which was distilled from zinc dust. Emeraldine salt was prepared by oxidizing aqueous HCl (5 mL of concentrated hydrochloric acid) solution of aniline (2.00 g) ( $C_6H_5NH_2$  or 99 atom % D  $C_6D_5NH_2$ ) with ammonium peroxydisulfate (4.9 g of  $(NH_4)_2S_2O_8$ ) in air at  $\sim 3^\circ C$ . After the oxidant was added, the solution was stirred for  $\sim 1$  hour. The temperature of polymerization was maintained by occasional addition of grape-sized chunks of ice. The precipitate was washed five times with deionized water and dried under vacuum at ambient temperature. Abbreviation ES/HCl is used for the compound throughout the dissertation.

FIGURE 3.1

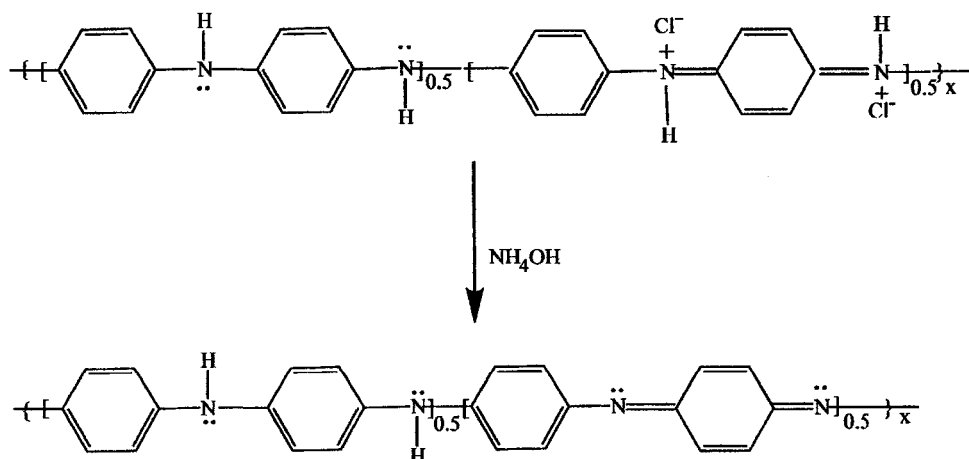
## SCHEMATIC ILLUSTRATION OF EMERALDINE SALT SYNTHESIS



Emeraldine hydrochloride was converted to the base by stirring with 0.1 M aqueous solution of ammonium hydroxide ( $\text{NH}_4\text{OH}$ ) in air for one hour. The suspension was filtered and washed with five portions of water, then dried at room temperature under vacuum.

FIGURE 3.2

## SCHEMATIC ILLUSTRATION OF OBTAINING EMERALDINE BASE



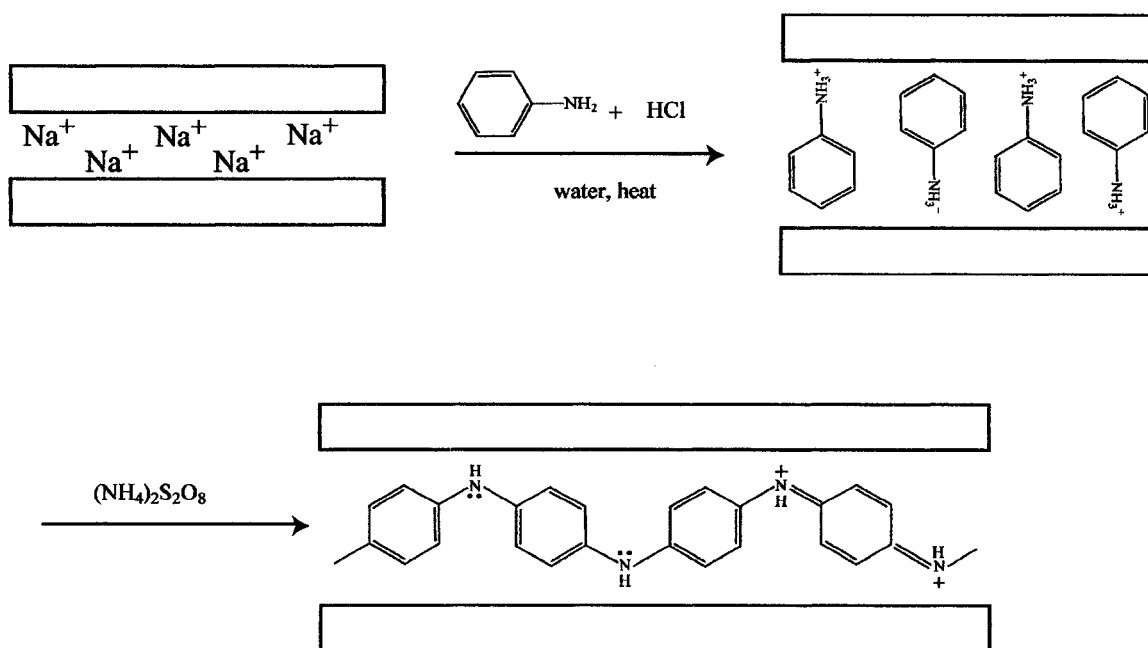
As was mentioned in Chapter 1, doping of Pani is reversible, and produces original polymer with little or no degradation. Thus, by controllably adjusting subsequent processing conditions, emeraldine base can be converted back to a conducting salt with tailor-made properties. For example, the conductivity of re-doped emeraldine salt can be varied over 5 orders of magnitude, depending on processing methodology. For the current study, deuterated polyaniline base was converted into two emeraldine salt films with different properties. The processing was done by Dr. Espe's group at the University of Akron as follows: a 2:1 mole ratio of camphorsulfonic acid (CSA) and emeraldine base (EB) were mixed for ~ 2 min and then added to either (a) *m*-cresol or (b) N-methylpyrrolidone (NMP) to form a 1 wt.% solution. The *m*-cresol solution (ES/CSA/*m*-cresol) was sonicated for 9 hrs at room temperature, stirred for 14 hrs and then filtered through a 0.45 $\mu$ m syringe filter (Whatman: PTFE) onto a glass plate, which was placed into a vacuum oven at 50°C until the film was dry (~5 hours). The NMP solution (ES/CSA/NMP) was sonicated for 7 hrs at ambient temperature, stirred for 16 hrs and filtered through a 0.45 $\mu$ m syringe filter into a petri dish. It was placed in a vacuum oven at 50°C for ~9 hrs (until dry).

A schematic illustration of Pani / Clay nanocomposite synthesis is shown in Figure 3.3. In the first step of the reaction, sodium montmorillonite is dispersed in water. At low concentrations, the clay in water facilitates the exchange of surface ions<sup>44</sup>. Excess aniline hydrochloride is used in this step to replace surface Na<sup>+</sup> completely with anilinium ions. After washing the mixture with a large amount of de-ionized water only the monomer that had been introduced into clay galleries remains in the reaction system.

Finally, an oxidant was added to initiate the polymerization reaction. The product was thoroughly washed with de-ionized water to remove unreacted oxidant.

FIGURE 3.3

## SCHEMATIC ILLUSTRATION OF POLYANILINE / CLAY SYNTHESIS



The complete recipe of the synthesis is as follows: 4 grams of  $\text{Na}^+$ -MMT (Southern Clay Products, Inc.) was added to 200 ml of de-ionized water and stirred for 3.5 h at  $70^\circ\text{C}$ . Then, 0.82 ml of aniline and 1.4 ml of concentrated HCl were added. After stirring for 17 hours at  $70^\circ\text{C}$ , the mixture was washed with room temperature de-ionized water three times. More HCl was added to return the pH to 2, and the mixture was stirred for another hour. 2.023g of ammonium peroxydisulfate (0.0088 moles) was added. Polymerization lasted for approximately 15 hours. The precipitate was isolated by

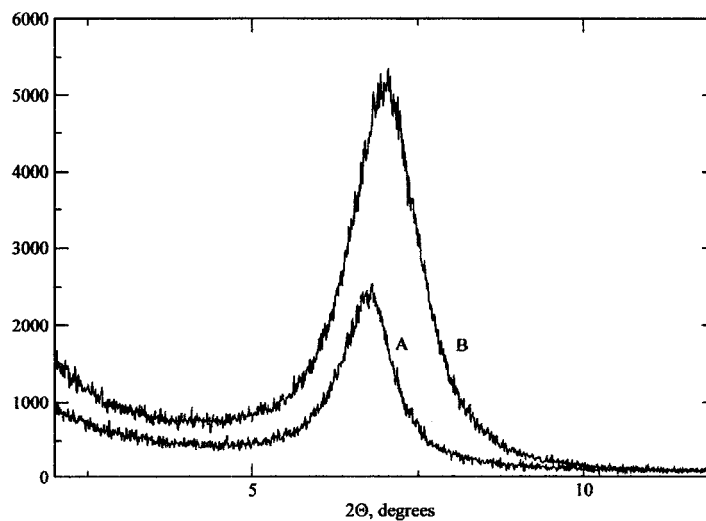
filtration, washed three times with de-ionized water and dried under vacuum at ambient temperature.

### 3.2 MATERIAL CHARACTERIZATION

Though nuclear magnetic resonance (NMR) was the primary tool of the research, x-ray diffraction (XRD) and Fourier transform Infrared spectroscopy (FTIR) were also employed to characterize the polymer samples.

FIGURE 3.4

XRD DATA FOR ANILINE AND POLYANILINE INTERCALATED INTO MMT  
CLAY LAYERS



XRD data for (A) aniline intercalated into MMT clay layers; (B) polyaniline/clay nanocomposite.

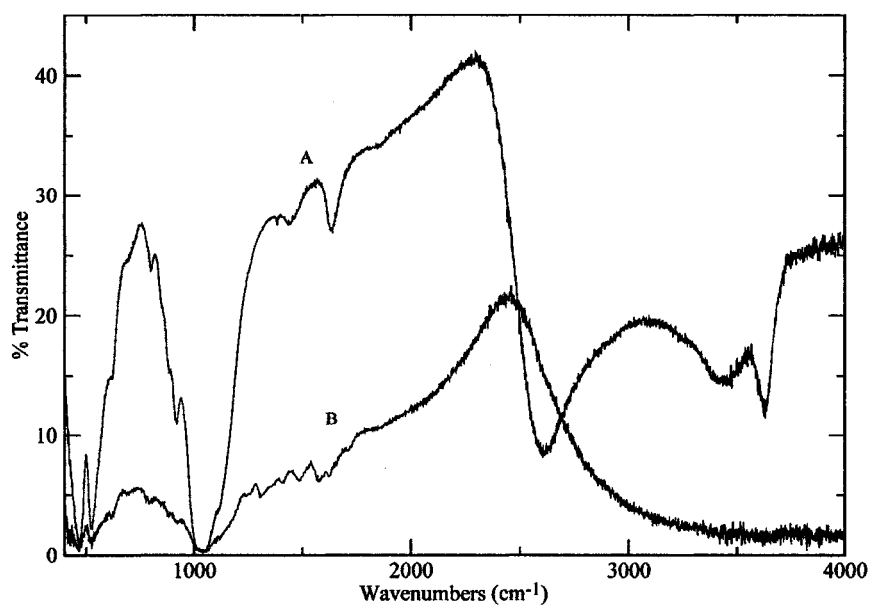
XRD measurements were carried out using a Scientag X1 diffractometer operating at 45 keV with a Cu source ( $\lambda = 15.4$  nm). The  $d_{001}$  spacing is commonly measured by x-ray diffraction for organoclays and includes the inner layer space and the thickness of one of the clay particles; in other words the  $d$ -spacing is the distance between two identical faces in the stack of clay particles. A pure MMT clay sample (not shown) had a broad peak at  $2\theta = 9^\circ$ . According to Bragg's law, which gives the relationship among the angular position of the diffracted beam, the wavelength  $\lambda$  of the incoming x-ray radiation and the interplanar distance  $d_{hkl}$ ,  $\lambda = 2d_{hkl}\sin\theta$ , the measured angle corresponds to interlayer spacing of 7.8 Å. The spacing increased to 13.06 Å upon intercalation of aniline into clay layers. This suggests that aniline rings are oriented approximately perpendicular to the clay layers (Figure 3.3 and 3.4). After polymerization, the spacing was slightly smaller, 12.66 Å, in agreement with the suggestion<sup>66</sup> of single layer intercalation and extended chain conformation (Figure 3.3 and 3.4).

The percent crystallinity of partially crystalline polymer samples, such as polyanilines, can be determined by powder x-ray diffraction technique. XRD spectra of emeraldine base and salt are similar to those reported earlier<sup>24</sup>. A broad, featureless pattern was found for EB; this is characteristic of amorphous polymers. The ES samples exhibited well-defined peaks at  $2\theta = 9^\circ, 15^\circ, 20^\circ, 26^\circ, 28^\circ$  and  $31^\circ$ , superimposed on a broad amorphous background. The fraction of crystallinity for ES/HCl and ES/CSA/m-cresol samples, determined by estimating the integrated intensity of the peaks above the amorphous background, is approximately  $25 \pm 1\%$  and  $30 \pm 6\%$  respectively.

FTIR spectroscopy was performed on pressed disks of Pani/clay dispersed in KBr using a Nicolet DXB 20 spectrometer. The spectra are consistent with results reported by Wu *et al.*<sup>66</sup>, and exhibit characteristic absorption lines for emeraldine [1563 and 1489  $\text{cm}^{-1}$ ] and clay (Figure 3.5).

FIGURE 3.5

## FTIR MEASUREMENTS FOR CLAY AND PANI/CLAY NANOCOMPOSITE



FTIR measurements for (A) clay and (B) Pani/clay nanocomposite.

Ambient temperature, four-probe dc resistivities of protonated polyaniline ES/HCl, EB and the polyaniline/clay nanocomposite were measured using MMR Technologies' computer-controlled Low Temperature Hall system. The resistivity measurements were based on a method which holds for any flat sample of arbitrary

shape<sup>67</sup>. Four conditions must be fulfilled in order for the method to work: (a) the sample must be homogeneous in thickness, (b) the sample must not have isolated holes, (c) electrical contacts must be made at the circumference of the sample, (d) the contacts must be sufficiently small. Thin pellets for conductivity measurements were pressed from powder, using a press with hydraulic pressure of 1700 psi. Electrical contacts were made with conductive silver epoxy (EPO-TEK). Linearity checks were performed to insure Ohmic contact. Conductivities of ES/HCl, EB and Pani/clay were found to be 0.15 S/cm,  $1 \times 10^{-9}$  S/cm and  $1 \times 10^{-4}$  S/cm respectively. The relative error for conductivity measurements was 2 %.

### 3.3 NMR EXPERIMENTS

The NMR experiment is technically quite difficult. The main challenges are resolution and sensitivity. First, the Larmor frequencies must be measured with extremely high accuracy (better than 1 part in  $10^9$ ) to allow the resolution of small differences in the nuclear Larmor frequency, due to interactions of nuclei and the surrounding medium. Second, the NMR signal is very weak. The occupation of each eigenstate of the Hamiltonian is subject to constraints of thermal equilibrium; the population of  $i$ -th quantum state is given by the Boltzmann relation

$$p_i = \frac{e^{-\frac{E_i}{k_B T}}}{Z} \quad [3.1]$$

where  $Z$  is the partition function,  $E_i$  is the energy of  $i$ -th state,  $T$  is the temperature of a sample and  $k_B$  is Boltzmann constant. The intensity of the observed transition between

nuclear spin energy levels in a bulk sample is proportional to the difference in populations, which can be written as

$$p_i - p_j = \frac{1}{Z} \left( e^{\frac{-E_i}{k_B T}} - e^{\frac{-E_j}{k_B T}} \right) \quad [3.2]$$

For example, the difference in populations between two energy levels for protons ( $I=1/2$ ) at ambient temperature in the magnetic field of 7 T is

$$P_{-1/2} - P_{1/2} = \frac{1 - e^{\frac{-\gamma \hbar B_0}{k_B T}}}{1 + e^{\frac{-\gamma \hbar B_0}{k_B T}}}$$

Since the Boltzmann factor appearing in this equation is very small (which justifies expansion of exponential factors in a Taylor series and disregard of all terms beyond the first) one can approximate the population difference to be  $\frac{\gamma \hbar B_0}{2k_B T} \approx 3.8 \cdot 10^{-6}$ . This result implies that only 30-40 spins in 10,000,000 will contribute to the observable microscopic magnetic moment.

Moreover, the individual nuclear magnetic moments are very small compared to those of electrons. For solid samples, the sensitivity is further decreased by the presence of anisotropic interactions, which, in general, lead to the spread of intensity over a broad frequency range.

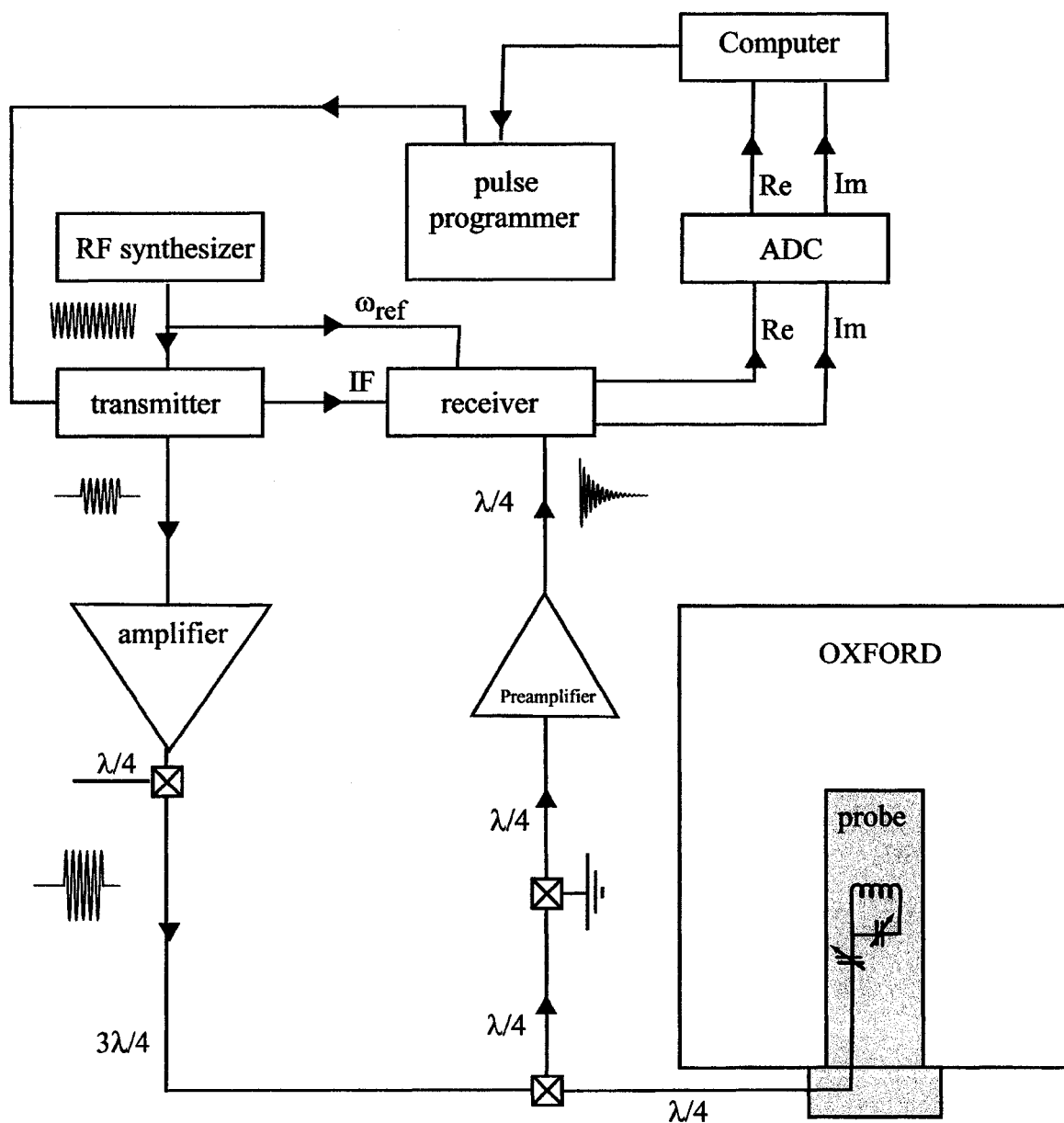
The low sensitivity of NMR experiments requires rather large amounts of sample (~0.1 g), compared to other spectroscopic techniques, and the development of technically demanding equipment and special experimental procedures. In the following section, the operation of the solid state NMR spectrometer is outlined. Experimental techniques and pulse sequences relevant to the study are discussed.

### 3.3.1 NMR SPECTROMETER AND PROBE

The NMR experiments require a high magnetic field, which is homogeneous within at least 1 part per  $10^9$ , to remove the degeneracy of the nuclear energy levels. The magnetic field homogeneity must be maintained over the entire volume of the sample. The magnetic field must also be very stable with respect to time. The data presented in this work were acquired using a superconducting magnet with the field strength of 7.048 T (OXFORD). This field is produced by a current of 36 A flowing through about one kilometer of wire made of a niobium and titanium alloy. The wire windings are immersed in a bath of liquid helium (4K), which is itself insulated by a reservoir of liquid nitrogen (77K). The reservoirs are separated from each other and from the outside environment by vacuum and radiation shields to reduce thermal leakage. The magnet is also provided with both superconducting and room temperature shim coils for adjusting the homogeneity of the field <sup>43</sup>.

To collect the data presented in this dissertation Tecmag (Apollo or Libra) and home-built hardware components were used. A schematic diagram of the spectrometer is presented in Figure 3.6. A precise and stable radio frequency synthesizer produces a continuous oscillating electrical signal at a spectrometer reference frequency, denoted  $\omega_{ef} = \omega_0 + \omega_{IF}$ , which is the sum of nuclear Larmor frequency and some intermediate frequency. This signal then travels to the transmitter section of the spectrometer, which is controlled by a timing device, called the pulse programmer. In most NMR experiments the RF phase is switched rapidly between different pre-defined values. The discontinuous phase shifts are accomplished in the transmitter section of the spectrometer, where the

FIGURE 3.6  
BLOCK DIAGRAM OF THE NMR SPECTROMETER



spectrometer reference signal is phase shifted with respect to the intermediate frequency. A fast switch or gate is opened at defined moments to allow the IF signal to pass through. The gating pulses at intermediate frequency are mixed with the continuous spectrometer reference frequency, then electronically filtered (to remove upper side-band  $\omega_{ref} + \omega_{IF}$ ), which produces Larmor frequency pulses. The duration of an RF pulse is referred to as the pulse width ( $t_p$ ).

The Larmor frequency pulse is then amplified and transmitted via coaxial cables ( $50 \Omega$ ) and a duplexer to the probe. To achieve uniform excitation of wide line deuteron spectra, the power levels in excess of kilowatt were applied to the probe.

The duplexer's functions are, first, to divert the strong RF pulse from the amplifier to the probe and not to the sensitive signal detection circuitry and, second, to direct the small NMR signal into the receiver rather than the transmitter. Crossed diodes and cables, cut to precise lengths ( $\lambda/4$ ) which depend on the Larmor frequency, play the role of the duplexer.

The most important characteristic of a  $\lambda/4$  line is that it acts as an impedance transformer with the transformation given by

$$Z_i Z_o = |Z|^2$$

where  $Z_i$  and  $Z_o$  are the input and the output impedances and where  $Z$  is the characteristic impedance of the cable being used ( $50 \Omega$ ). The crossed diodes act like switches which close for large signals but not for small signals. During the transmitter pulse the diodes are closed so that all the transmitter power is transformed to the probe. The low impedance of the diode switch (in the on condition) on the input of the quarter wave line, connected to the receiver, gets transformed to a high output value. When the transmitter

pulse is off, diode switches are opened and the NMR signal gets transformed by the quarter wave transformer. The transformed value is matched to the impedance of the receiver by a conventional transformer.

The NMR probe is a complex apparatus, which has several functions. First of all, it holds sample in the region of a homogeneous magnetic field. Second, it houses the resonance radio-frequency circuit, which consists of a 5 mm coil and several capacitors. The circuit is tuned to match the output impedance of the amplifier and cables at the resonance frequency of 46.06 MHz. This impedance matching minimized the reflected power and maximizes power transmitted to the probe. During the RF pulse, electrical currents in the coil generate an oscillating magnetic field at the sample. This magnetic field rotates nuclear the spin polarization creating transverse magnetization. When the RF pulse is terminated, the precessing nuclear magnetization induces electrical currents in the coil, which give rise to a small but detectable signal ( $\sim 1\text{-}100\ \mu\text{V}$ ). This free induction decay (FID) signal passes via the duplexer into a preamplifier (30dB). The amplified FID signal travels to the receiver.

Two different probes were used to collect the data. A home-built static deuterium probe was capable of withstanding high pulse power ( $\geq 500\ \text{V pp}$ ), so that a typical  $90^\circ$  pulse length was  $1.6\ \mu\text{s}$ . The  $Q$  factor of the probe was experimentally determined by matching experimental and simulated powder patterns of polyethylene test sample. The  $Q$ -value for the static probe was found to be 105.

The triple resonance Chemagnetics probe, which was used in a single channel mode, has magic angle spinning capabilities. In this probe, the sample is contained in a 5 mm zirconia cylindrical rotor (Chemagnetics). The rotor fits into a cylindrical stator in

the probe. Clean dry air or nitrogen forced through small holes in the stator blows over a fluted end-cap of the rotor, making it turn. The spinning frequency is controlled by a tachometer circuit, which monitors changes in the intensity reflected by a black mark painted on the top of the rotor. The tachometer output regulates the air valve of the Chemagnetics spin rate controller. Spin rates used for the experiments were 7.5 – 8.0 kHz. A typical pulse width in the magic angle spinning probe was in the range of 3.0 – 3.2  $\mu$ s. The  $Q$ -factor of this probe was determined to be 220.

The temperature around the coil is regulated by passing preheated or precooled air (20°C to 60°C) or nitrogen (lower than 20°C or higher than 60°C) gas. The temperature is adjusted and maintained to 0.01°C by a DRC-91CA LakeShore temperature controller. In the high power deuteron probe, a platinum resistor sensor is placed  $\sim$  1 cm away from the coil. For this probe calibration showed that the measured and real sample temperature were equal (within 0.5°C) after 15 –20 minutes of thermal equilibration<sup>57</sup>. The accessible temperature range for this probe is from –50°C to +100°C. In the magic angle spinning (MAS) probe, the temperature sensor is placed in the removable variable temperature (VT) stack at least 3 cm above the coil. The VT stack provides better thermal isolation since ambient temperature purge gas can be passed through the outer tube of the stack, which provide the isolation from the inner tube, where the heater element is contained. Since the VT gas path is different from the spinning gas path, heating or cooling the sample does not interfere much with the spinning stability. The operational range for the Chemagnetics probe is from –150°C to 250°C. The real sample temperature had to be determined through calibration since the spinning causes frictional heating of the sample<sup>57</sup>. The heater elements for both probes are nickel wires with magnesium oxide

insulation (ARI Industries). They are capable of carrying 1.9 and 5 A of current for the deuteron and MAS probe respectively. Adequate current levels and heater powers (115 W and 500 W) are provided by Kepco power supply (model ATE 150 – 3.5M). It's output current is regulated by the input voltage from (0 to 10 V) from the LakeShore temperature controller, changing in response to the resistance reading from the platinum resistor sensor (110 $\Omega$ ). The bore of the magnet has a home-built temperature monitoring system to insure safe operational conditions during variable temperature experiments. For the optimum regime of operation, the bore temperature must be maintained within the range +4 to +40°C.

After the FID signal passes through the preamplifier it is fed into the quadrature receiver, where it is further amplified (60 dB) to a more convenient voltage. In the receiver, the signal is divided into two components, one of which is mixed with the intermediate frequency wave  $S_A \propto \cos(\omega_{IF} + \phi)$ , and the other with the IF signal given additional 90° phase shift  $S_B \propto \cos(\omega_{IF} + \phi + \frac{\pi}{2})$ . The receiver also accomplishes frequency conversion by mixing the detected signal with a spectrometer reference wave at frequency  $\omega_{ref}$ , supplied by the RF synthesizer, and filtering out the high frequency side band. The heterodyne signal  $\Omega_0 = \omega_0 - \omega_{IF}$  oscillates in the audio frequency range (0 to ~500 kHz). This demodulation of the signal effectively corresponds to the observation of magnetization in the rotating reference frame, whose x-axis is defined as reference phase 0.

Each of the two outputs of the quadrature receiver is sent to analog-to-digital (ADC) converters. Here, their voltage is sampled periodically and the values are stored on a computer. The time interval between sampling, dwell time ( $t_d$ ), determines the width

of the spectrum. The highest frequency that can be accurately represented is the Nyquist frequency,  $\nu_N = \frac{1}{2t_d}$ . The use of quadrature receiver allows unambiguous detection of signals with negative frequencies in the rotating reference frame. Wide deuteron spectra required spectral widths of  $\pm 200$  or  $\pm 250$  kHz. Consequently, the appropriate dwell time was less than  $2.5 \mu\text{s}$ .

### 3.3.2 NMR DATA MANIPULATION

A digitized signal, collected as described in the previous section, is processed to produce an NMR spectrum. The frequencies in the spectrum correspond to the differences between spin energy levels for which spectroscopic transitions are allowed. Nuclei that resonate at the same frequency have identical magnetic environment. In simple experiments, the intensity observed at particular frequency is proportional to the number of nuclei that resonate at that frequency.

As was discussed in the introduction to the section 3.3, NMR signal is very weak. The signal emerging from the probe also contains noise. To increase the signal and minimize the noise, the technique known as “signal averaging” (strictly speaking, the signal is summed rather than averaged) is employed. The technique exploits the different statistical properties of the NMR signal and the noise and consists of adding FIDs. The NMR signal is reproducible, so that its intensity grows in proportion to the number of scans  $N$ . On the other hand, the noise is random and grows only as  $\sqrt{N}$ <sup>43</sup>. If one wishes

to double signal to noise ratio, the penalty is four fold increase in the number of scans, and thus, in time.

Spectral lines are sometimes artificially broadened in an effort to boost the apparent signal to noise ratio and save experimental time. In this process, known as apodization, the time-domain signal is multiplied by a weight function, usually a decaying exponential,  $\exp(-\Delta\omega t)$ , prior to Fourier Transform (FT). The multiplication of functions in time-domain corresponds to the convolution of their Fourier transforms in a frequency domain<sup>68</sup>. The result of the convolution is smoother but broader spectrum. The apodization procedure may be applied and quantitative characterization of the spectra should be still possible when the broadening does not compromise resolution, i.e. does not smear the difference between distinct resonances in the spectra. The amount of line broadening in Hz,  $\Delta\omega$ , applied to the spectrum is the full width at the half-maximum intensity of the Fourier transform of the apodizing function. Moderate broadening (a few hundred hertz) is usually acceptable for most solid state static deuteron NMR spectra, since it is smaller than the line width associated with the anisotropic quadrupole interactions.

Another procedure, known as zero-filling, can be used to digitally increase spectral resolution. In general, there are two kinds of uses for zero-filling. First, zeroes may be added to a time-domain data set, in order to increase the digital resolution of the discrete frequency spectrum resulting from a subsequent Fourier transform. Alternatively, one may filter out noise by substituting (rather than adding) zeroes for some of the data points in the time-domain.

A few spectral artifacts may arise due to hardware limitations. A common artifact in quadrature detection is the presence of a (false) peak at the center of the spectrum. The artifact arises from a difference in offset between the two time-domain quadrature signals<sup>68</sup>. A baseline correction is applied to bring each channel offset to zero before FT in such cases.

Spectrometer electronics also gives rise to unavoidable phase shifts of zero- ( $\phi_0$ ) and first- ( $\phi_1$ ) order. Term  $\phi_1$  is associated with experimental time delays, such as the delay which must be left after RF pulse before the NMR signal can be sampled, in order to allow the pulse energy to dissipate. The shift in time-domain leaves magnitude of the Fourier transformed spectrum unaffected but the real and imaginary parts of the spectrum are phase-shifted. If  $\phi_0$  and  $\phi_1$  are not too large, the pure absorption spectrum can be recovered by a computerized phase correction procedure, where instead of displaying the real part of the spectrum  $S(\omega)$  one displays  $s_{corrected}(\omega) = S(\omega)e^{-i(\phi_0 + \phi_1\omega)}$ .

### 3.3.3 PULSE SEQUENCES AND EXPERIMENTAL TECHNIQUES

The ability to precisely control the creation of population differences and coherent superpositions of eigen-states makes NMR a very powerful spectroscopic tool. Pulses of various lengths, intensities and phases are used to prepare the system in a particular coherent state. The system is then allowed to evolve under the influence of a specific

Hamiltonian. After evolution, observable single quantum coherences are created by the pulses during mixing time. Finally, the signal is acquired during the detection time.

This section of the dissertation describes briefly NMR pulse sequences and techniques employed for characterization of polyanilines. The full details, including artifact suppressing phase cycles, limitations and hardware requirements can be found references <sup>57,60,69-71</sup>.

In the absence of molecular motion, the spin evolution can be calculated using the reduced density matrix expanded in a set of basis operators <sup>49</sup>. In general a basis set of  $(2I + 1)^2 - 1$  independent orthogonal operators is used. The one conventional frequently used basis set for spin  $I = 1$  is comprised of the operators  $I_x, I_y, I_z, Q_x = I_z I_x + I_x I_z, Q_y = I_z I_y + I_y I_z, Q_z = \frac{1}{\sqrt{3}}(3I_z^2 - I^2), D_x = I_x^2 - I_y^2, D_y = I_x I_y + I_y I_x$ . The two quadrupole transitions can be pictured as two magnetization vectors, with precession frequencies  $\pm \omega_Q$  in the rotation reference frame. The vector sum of these two transitions is proportional to  $I_i$  while the vector difference is proportional to  $Q_i$ , where the subscript  $i$  describes the orientation  $(\vec{x}, \vec{y}, \vec{z})$ . Magnetizations  $I_x, I_y, Q_x$  and  $Q_y$  describe single quantum coherences, which are detectable by NMR. The operators  $D_x$  and  $D_y$  describe double quantum coherences between the  $|+1\rangle$  and  $|-1\rangle$  states and can be inferred only by conversion into one of the observable quantum states.

The simplest pulse sequence consists of a single RF pulse of flip angle  $\beta^\circ$ , which rotates the equilibrium magnetization away from the  $\vec{z}$  axis. The RF Hamiltonian (in units of rad/s) for a  $x$  phase pulse of amplitude  $\omega_1$  is  $H_1 = \gamma_D B_1 I_x = \omega_1 I_x$ . A pulse duration  $t_p$  has a flip angle  $\beta = \omega_1 t_p = 2\pi\nu_1 t_p$ . The initial state (thermal equilibrium) of

the spin ensemble in the static magnetic field is  $\rho_{initial} = \frac{e^{-\frac{H}{k_B T}}}{Z} \approx \frac{1}{(2I+1)} (1 + \gamma_D \hbar B_0 I_z)$  in

high temperature approximation. The constant term with no time dependence can be disregarded, and the reduced normalized density operator can be thought as  $\rho(0^-) = I_z$ .

Then, according to the Equation 2.16 the density matrix immediately after the pulse is:

$$\rho(0^+) = e^{-i\beta I_x} I_z e^{i\beta I_x} = I_z \cos\beta - I_y \sin\beta \quad [3.3]$$

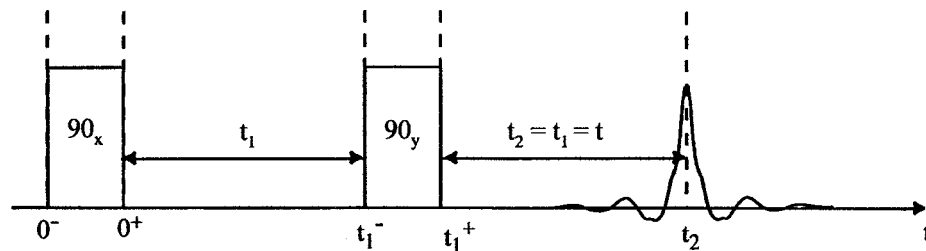
Maximum conversion of  $I_z$  to  $I_y$  occurs if  $\beta = 90^\circ$ , so that  $\rho(0^+) = -I_y$ .

The deuteron powder patterns are reasonably broad, which results in rapid dephasing of the FID. Thus, much signal intensity is lost due to the electrical dead time right after the pulse. If undistorted FIDs are to be recorded, it is necessary to refocus the magnetization outside the dead time interval. This is achieved by using two-pulse quadrupole echo (QE) sequence,  $90_x - t_1 - 90_y - t_2 - ACQ$ , shown in Figure 3.7. During the pulse spacing  $t_1$ , the density matrix evolves under quadrupole Hamiltonian  $H_Q$  (Eq. 2.28):

$$\rho(t_1^-) = -e^{-iH_Q t_1} I_y e^{iH_Q t_1} = -I_y \cos(\omega_Q t_1) + Q_x \sin(\omega_Q t_1) \quad [3.4]$$

FIGURE 3.7

QUADRUPOLE ECHO PULSE SEQUENCE



The application of a second  $90^\circ$  pulse with  $y$ -phase results in a density matrix of the form

$$\rho(t_1^+) = e^{-i\beta I_y} \rho(t_1^-) e^{i\beta I_y} = -I_y \text{Cos}(\omega_Q t_1) - Q_x \text{Sin}(\omega_Q t_1) \quad [3.5]$$

During  $t_2$ , free precession under the quadrupole Hamiltonian causes the density matrix to oscillate between single quantum operators,

$$\begin{aligned} \rho(t_1 + t_2) = & -\text{Cos}(\omega_Q t_1) \{I_y \text{Cos}(\omega_Q t_2) - Q_x \text{Sin}(\omega_Q t_2)\} - \\ & - \text{Sin}(\omega_Q t_1) \{Q_x \text{Cos}(\omega_Q t_2) + I_y \text{Sin}(\omega_Q t_2)\} \end{aligned} \quad [3.6]$$

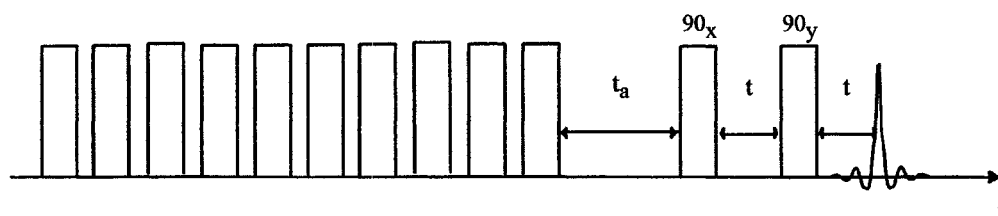
When  $t_1 = t_2 = t$ , the magnetization refocuses, and the density matrix identical to that following the first  $90^\circ$  pulse,

$$\rho(2t) = \rho(0^+) = -I_y \quad [3.7]$$

This way an undistorted FID can be acquired (ignoring relaxation that occur during  $2t$  period). Since the QE echo sequence avoids distortion and allows observation of  $I_z$  by converting it into  $I_y$ , it is of general use for signal detection as a part of more complicated pulse sequences.

FIGURE 3.8

PRESATURATION QUADRUPOLE ECHO SEQUENCE

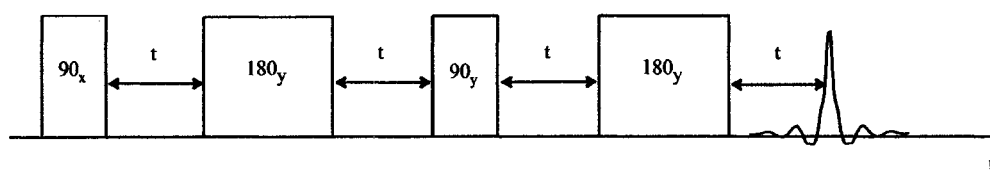


Experimentally, pulse imperfections and DC offsets are impossible to avoid, which leads to undesirable spectral artifacts. These effects are minimized by phase cycling the pulses. A phase cycle works by selectively changing the sign of specific terms in the density matrix. This allows unwanted coherences to sum to zero and the desired signal to be coherently averaged. Details of phase cycle for the QE sequence can be found in Ph.D. dissertations of M. Brown and T. Tse<sup>60,69</sup>.

If the observed line shape of a sample can be described in terms of fast and slow rate dynamic processes, selective observation of the more quickly relaxing component can be achieved with a presaturation pulse sequence. The sequence consist of three parts: (a) a  $90^\circ$  pulse train to saturate the entire spin system; (b) a delay,  $t_a$ , to allow the observed component to relax (generally 3 times longer that the  $T_{1Z}$  of the quickly relaxing component); and (c) the regular quadrupole echo sequence to detect the magnetization. For Pani, ten saturation pulses separated by 1 ms suffice to prepare the system. Then, spins were allowed to relax for 40 ms before QE pulses were applied.

FIGURE 3.9

## PARAMAGNETIC QUADRUPOLE ECHO SEQUENCE

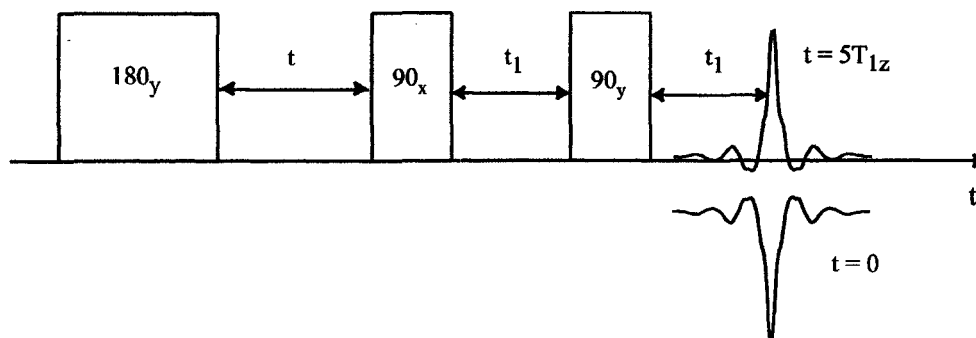


Since the clay sample has paramagnetic impurities, two  $180^\circ$  refocusing pulses were interleaved in the QE sequence to refocus paramagnetic shifts<sup>71</sup>:

$90_x^\circ - t - 180_y^\circ - t - 90_y^\circ - t - 180_y^\circ - t - ACQ$  (Figure 3.9). Deuterons close the paramagnetic centers, experience coupling to the electron magnetic moment. Since typically electron relaxation rate is fast, the precession rate of deuterons in different parts of the sample can differ. As a result, additional refocusing is needed in order to observe the echo.

FIGURE 3.10

## INVERSION RECOVERY QUADRUPOLE ECHO SEQUENCE



To measure the spin-lattice relaxation time,  $T_{1z}$ , an initial  $180^\circ$  pulse applied to invert equilibrium populations of the energy levels

$$\rho(0^+) = e^{-i\pi I_x} I_z e^{i\pi I_x} = -I_z \quad [3.8]$$

Then, spins left to relax for a variable delay time,  $t$ , during which spins reestablish thermal equilibrium by interaction with fluctuating local fields in the lattice

$$\rho(t) = \rho(0^-) (1 - 2e^{-\frac{t}{T_{1z}}}) = I_z (1 - 2e^{-\frac{t}{T_{1z}}}) \quad [3.9]$$

The quadrupole echo sequence is used after the inversion pulse and the relaxation delay to convert z-magnetization into observable single quantum coherences. The three-pulse

inversion recovery quadrupole echo (IRQE) pulse sequence,  $180_x^\circ - t - 90_x^\circ - t_1 - 90_y^\circ - t_1 - ACQ$ , is illustrated on Figure 3.10. The  $T_{Iz}$  analysis is performed at a variety of positions on the powder line shape. The variation of the relaxation time as a function of frequency gives the anisotropy.

In practice, finite RF power allows only a limited frequency bandwidth to be excited, where the bandwidth of a pulse is determined by the Fourier frequency components of the pulse envelope. Short pulses have more Fourier components than longer pulses, and excite a broader frequency spectrum. For deuteron powder patterns the bandwidth of 200 – 300 kHz is often needed, thus it is essential to provide very short  $90^\circ$  pulses. The problem of non-uniform spectrum excitation even more pronounced for inversion pulses in the measurements of the spin-lattice relaxation time anisotropy. Composite pulses with flip angles of  $90^\circ$  and  $180^\circ$  have been developed to address this problem<sup>70</sup>. The following pulse sequence was used for  $T_{Iz}$  measurements in Chemagnetics probe:

$$[90^\circ]_\phi - [90^\circ]_{\phi \pm 90^\circ} - [90^\circ]_\phi - t - 90_x^\circ - t_1 - 90_y^\circ - t_1 - ACQ$$

The use of square brackets signifies a composite  $90^\circ$  pulse,  $[90^\circ]_\phi = 135_\phi^\circ - 90_{\phi+90^\circ}^\circ - 45_\phi^\circ$ . The phase,  $\phi$ , of the inversion pulse must be cycled through  $x, \bar{x}, y, \bar{y}$  in order to select just longitudinal components of magnetization<sup>70</sup>.

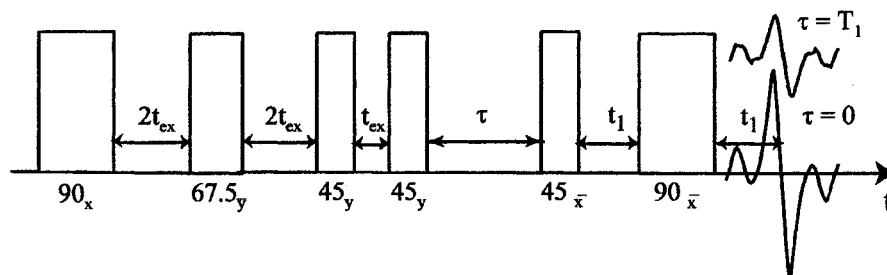
Quadrupolar order,  $Q_z$ , is described by a state in which only one of the two transitions has been inverted. For spin-1 system,  $Q_z$  relaxes independently if  $I_z$  with the relaxation time  $T_{IQ}$ . The broadband Jeener – Broekaert (BBJB) pulse sequence,

$$90_x^\circ - 2t_p - 67.5_{\bar{y}}^\circ - 2t_p - 45_y^\circ - t_p - 45_y^\circ - \tau - 45_{\bar{x}}^\circ - t_1 - 90_{\bar{x}}^\circ - t_1 - ACQ$$

(Figure 3.11), is capable of uniform excitation of quadrupolar order over wide frequency range without producing Zeeman order <sup>60</sup>. The excitation bandwidth is controlled by changing the excitation delay,  $t_{ex}$ . The first four pulses prepare quadrupolar order <sup>60</sup>. During the relaxation delay,  $\tau$ , this order decays

FIGURE 3.11

## BROADBAND JEENER – BROEKAERT (BBJB) PULSE SEQUENCE

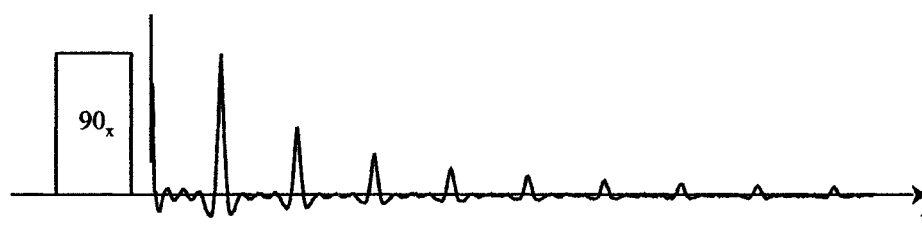


exponentially  $\langle M(t) \rangle \propto \langle Q_z(0) \rangle e^{-\frac{\tau}{T_{1Q}}}$ . Then, the fifth and sixth pulses create and refocus the detectable single quantum coherences. Appropriate phase cycles are used to remove unwanted coherences <sup>60</sup>.

An alternative to the use of quadrupole echo is provided by the deuteron magic angle spinning experiment. This experiment retains information about the quadrupole coupling (from sideband intensities) and provides additional information about small chemical shifts, obscured in the QE spectra. Deuteron MAS is performed with application of a single  $90^\circ$  excitation pulse. During acquisition the density matrix evolves under quadrupole Hamiltonian, which is periodically modulated by MAS (Eq. 2.73). Thus,

every rotor period the magnetization is refocused to  $-I_y$  since at that time  $v_Q(nt_r) = v_Q(0)$  (Eq. 3.7,  $t = t_r/2$ ). The MAS single pulse sequence with a rotary echo train is shown in Figure 3.12.

FIGURE 3.12  
SINGLE PULSE MAGIC ANGLE SPINNING EXPERIMENT

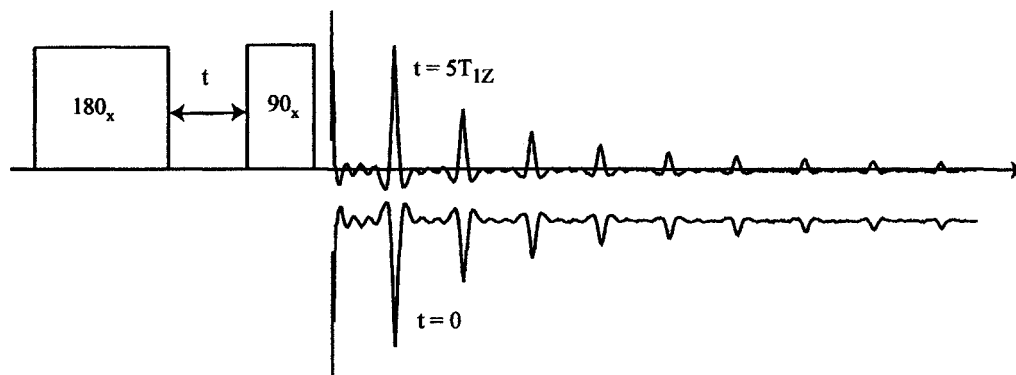


Due to transverse relaxation, the echo amplitudes are attenuated after increasing number of rotor periods. Measurements of the intensity of each rotary sideband reveal the average dephasing time  $T_2$  of the transverse magnetization. The Fourier transform of the experimental FID produces a line shape consisting of the sidebands at multiples of the rotor frequency, whose width is determined by the rate of echo attenuation, and an intensity profile reminiscent of the QE line shape.

The spin – lattice relaxation time,  $T_{1z}$ , can also be measured using  $^2\text{H}$  MAS technique. As described before, a  $180^\circ$  pulse is applied to invert the initial magnetization and the spins relax during a variable time  $t$ , after which one  $90^\circ$  pulse is applied to detect

FIGURE 3.13

## INVERSION RECOVERY MAGIC ANGLE SPINNING EXPERIMENT



the rotary echo train (Figure 3.13). This technique can be especially useful if magic angle spinning provides enough resolution to distinguish several shifted overlapping sidebands due to different magnetic environments in the sample (chemical shift, Knight shift, paramagnetic shift). It reveals relaxation time information for each set of the shifted sidebands.

## CHAPTER 4

### QUADRUPOLE ECHO LINESHAPES

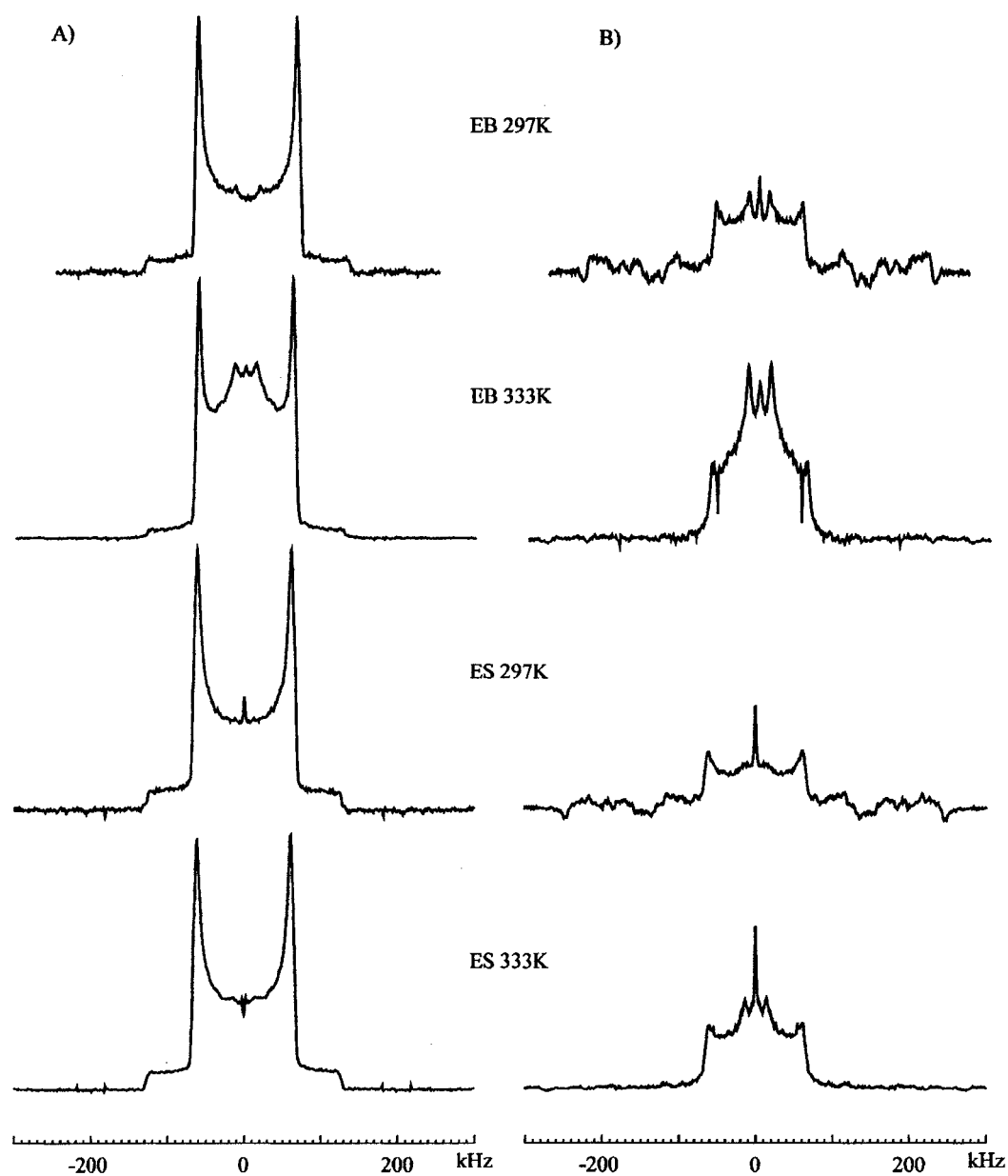
Knowledge of the types and timescales of molecular motion in solid polymers should provide a better understanding of their bulk properties. This chapter is devoted to the first experimental NMR characterization of polyanilines, using  $^2\text{H}$  quadrupole echo lineshapes. Models for interpreting of the experimental results are introduced and validated.

#### 4. 1 EXPERIMENTAL RESULTS

Experimental quadrupole echo (A) and presaturation (B) line shapes of ring deuterated emeraldine base and emeraldine salt at 297 K and 333K are shown in Figure 4.1. A recycle delay (RD) of 12 s was used for emeraldine base, while 10 s proved adequate for the salt sample.

The QE line shape is a superposition of spectra of fast flipping and rigid rings, as seen in Figure 4.1. However, as pointed out by Kaplan *et al.*<sup>32</sup>, this

FIGURE 4.1

 $^2\text{H}$  QUADRUPOLE ECHO AND SPECTRA PRESATURATION SPECTRA OF RING-DEUTERATED EMERALDINE BASE AND SALT $^2\text{H}$  quadrupole echo (A) and spectra presaturation (B) spectra of ring-deuterated emeraldine base and salt at  $T = 297$  and  $333$  K.

apparent bimodal distribution of flip rates is probably an artifact of the QE experiment, arising from its selective suppression of rapidly dephasing spins with intermediate jump rates. In polymers dynamic heterogeneity is usually interpreted as a manifestation of differences in packing densities<sup>72</sup>. Our experimental results agree qualitatively with data reported by Kaplan *et al.*<sup>32</sup>.

A presaturation experiment suppresses the slowly relaxing “rigid” powder pattern and the residual spectrum is dominated by a lineshape, characteristic of rings undergoing rapid 180° flips. The minor static component in these lineshapes can be accounted for by incomplete saturation of the rigid deuteron.

As can be seen from Figure 4.1, powder samples of emeraldine base and emeraldine hydrochloride have similar quadrupole echo spectra. For both samples, the relative amount of the fast flipping component increases as temperature increases. Presumably, as temperature rises, the free volume increases and rings are less constrained by neighboring chains. At all temperatures EB has a higher fraction of fast flippers than ES/HCl. The fraction of fast flippers in the emeraldine salt sample can be influenced by several factors. First, earlier studies of semicrystalline polymers containing aromatic rings in the backbone showed that the phenyl rings in the crystalline region are static on the spectral timescale<sup>73</sup>. While the XRD spectrum for EB, described in Chapter 3.2, was characteristic of an amorphous polymer, the ES/HCl sample was determined to be 25% crystalline. Another factor that can influence ring flips is partial double-bond character of nitrogen-aromatic bond, which would prevent rapid flips in amorphous regions of

ES/HCl. It was also suggested<sup>32</sup> that electrostatic interaction with chloride counter-ions may be an important factor that constrains flipping.

The parameters of observed lineshapes can be simulated using irreducible spherical tensors. In the principal axis system of the electric field gradient tensor, the quadrupole coupling and asymmetry parameters are defined by the constant tensor components  $T_0^{(2)}(PAS)$  and  $T_{\pm 2}^{(2)}(PAS)$  (Eq. 2.27). These quantities are related to their counterparts in the laboratory fixed coordinate system by a series of Euler rotations:

$$T_m^{(2)}(LAB) = \sum_{l=-2}^2 D_{lm}^{(2)}(\Omega_{ML}) \sum_{k=-2}^2 D_{kl}^{(2)}(\Omega_{PM}) T_k^{(2)}(PAS) \quad [4.1]$$

Here  $D_{ij}^{(2)}(\Omega)$  denotes the  $(i,j)$  element of the second rank Wigner rotation matrix for the transformation  $\Omega$ . The transformation which rotates the principal axis system into a set of molecule fixed axes is denoted  $\Omega_{PM} = (\alpha_{PM}, \beta_{PM}, \gamma_{PM})$ , while  $\Omega_{ML} = (\alpha_{ML}, \beta_{ML}, \gamma_{ML})$  denotes the rotation from the molecule fixed frame to laboratory axes.

As was noted in section 2.3.1, to describe an NMR powder pattern, it is appropriate to average the spin interactions over all motions that are faster than the spectral time-scale.

$$\langle T_m^{(2)}(LAB) \rangle = \sum_{l=-2}^2 D_{lm}^{(2)}(\Omega_{ML}) \sum_{k=-2}^2 \langle D_{kl}^{(2)}(\Omega_{PM}) \rangle T_k^{(2)}(PAS) \quad [4.2]$$

Thus, for  $m = 0$ , which is the only component needed to compute the lineshape, one obtains

$$\langle T_0^{(2)}(LAB) \rangle = \frac{\sqrt{6}}{8} \langle \Omega_M \rangle (3 \cos^2 \beta_{ML} - 1 + \langle \eta_M \rangle \sin^2 \beta_{ML} \cos 2\alpha_{ML}) \quad [4.3]$$

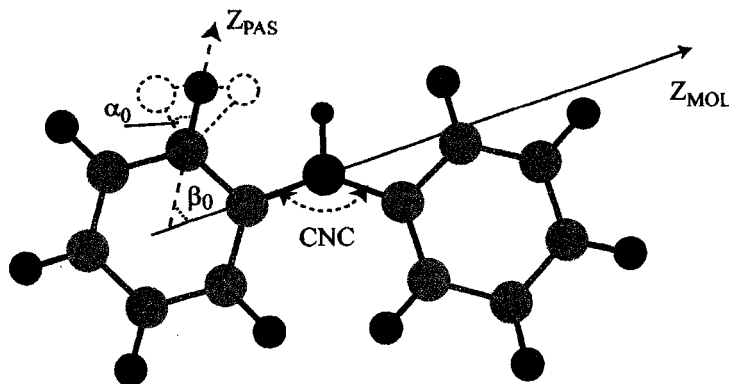
where the angular brackets mean ensemble average due to fast molecular motion, and  $\langle \Omega_M \rangle, \langle \eta_M \rangle$  are the observed average quadrupole coupling and asymmetry parameters, respectively.

## 4.2 FAST 180° JUMPS

In polymers containing backbone phenyl rings 180° ring-flips are common and the rate of motion reflects local variations in free volume<sup>72,73</sup>. In Pani, ring flip rates are also influenced by electrostatic interactions with counter-ions and partial double bond character of the C–N bonds in the quinoid moieties<sup>32</sup>.

FIGURE 4.2

SCHEMATIC ILLUSTRATION OF A PART OF POLYANILINE MOLECULE



A simple two-site model was used to simulate the fast flipping component. The orientations of the jump sites were  $\Omega_1 = (0, \beta_0, 0)$  and  $\Omega_2 = (180, \beta_0, 0)$  with equal probability to find a ring in either orientation. The molecule's fixed  $\bar{z}$ -axis is chosen to

pass through the C-N bond, and it is assumed that the deuteron EFG tensor has its largest component along the C-D bond direction (see Figure 4.2). The averaged quadrupole coupling parameters can be found to be

$$\langle \Omega_M \rangle = \frac{\omega_Q}{2} (\eta_{PAS} \sin^2 \beta_0 + 3 \cos^2 \beta_0 - 1) \quad [4.4]$$

$$\langle \eta_M \rangle = \frac{\eta_{PAS} (1 + \cos^2 \beta_0) + 3 \sin^2 \beta_0}{\eta_{PAS} \sin^2 \beta_0 + 3 \cos^2 \beta_0 - 1} \quad [4.5]$$

Thus, when  $\beta_0 = 60^\circ$  and  $\eta_{PAS} = 0$ , the  $^2\text{H}$  NMR lineshape has distinct singularities separated by  $\Omega_Q/4$  (see Eq. 2.31). Note that fast  $180^\circ$  flips produce a motionally averaged z- axis of the PAS that is shifted away from C-D bond. This effect is discussed in Appendix C.

### 4.3 CONE LIBRATION

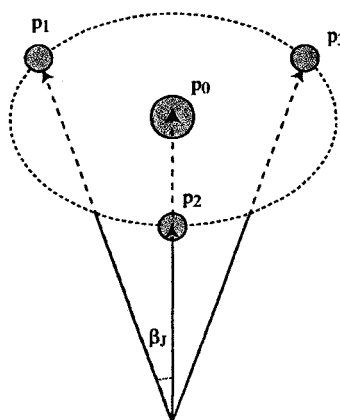
It was shown previously, that a pure  $180^\circ$  flip model is not adequate to explain the motion of phenyl rings in polymers<sup>73</sup>. Fast librational motion has to be incorporated into theoretical lineshape calculations. A model of jumps between four cone sites  $\Omega_1 = (0,0,0)$ ,  $\Omega_2 = (0, \beta_J, 0)$ ,  $\Omega_3 = (120, \beta_J, 0)$ ,  $\Omega_4 = (240, \beta_J, 0)$  is one possibility. If the probability of jumps is uniform  $P(\Omega) = 1/4$ , then the average asymmetry parameter is zero and the quadrupole coupling constant reduces to

$$\langle \Omega_M \rangle = \frac{\omega_Q}{4} \sum_{i=1}^4 \frac{1}{2} (3 \cos^2 \beta_i - 1) = \frac{\omega_Q}{4} \left( 1 + \frac{3}{2} (3 \cos^2 \beta_J - 1) \right) \quad [4.6]$$

This model can reflect the existence of motionally induced asymmetry by assuming unequal populations of four cone sites,  $(p_0, p_1, p_2, p_3)$ , as illustrated in Figure 4.3.

FIGURE 4.3

## ORIENTATIONAL SITES FOR THE SIMULATION OF MOTION IN A CONE



C-D bonds are assumed to jump among the four orientations indicated by the four vectors. The site populations, indicated by the size of the balls, may be different.

## 4.4 LIBRATIONS ON AN ARC

Librations along restricted arcs are another plausible class of motion in polyaniline. Two types of arc librations are considered here.

a) Phenyl rings undergo small angle librations along the same arc, which defines the  $180^\circ$  jump trajectory, but restricted to the range  $-\alpha_0 \leq \alpha(t) \leq \alpha_0$  (see Figure 4.2). The transformation  $\Omega_{pM} = (\alpha(t), \beta_0, 0)$  and the effect of libration on the observed quadrupole coupling parameters can be evaluated<sup>57</sup> by averaging equation 4.1 over the

one-dimensional arc, with uniform probability  $P(\Omega_{PM}) = \frac{1}{2\alpha_0}$ . The averaged quadrupole

coupling parameters in this case are

$$\langle \Omega_M \rangle = \omega_Q \left( \frac{1}{2} (3 \cos^2 \beta_0 - 1) + \frac{\eta_{PAS}}{4\alpha_0} \sin^2 \beta_0 \sin 2\alpha_0 \right) \quad [4.7]$$

$$\langle \eta_M \rangle = \frac{\frac{\eta_{PAS}}{4\alpha_0} \{ \sin 2\alpha_0 (1 + \cos^2 \beta_0) \} + 3 \sin^2 \beta_0}{\frac{\eta_{PAS}}{2\alpha_0} \sin 2\alpha_0 \sin^2 \beta_0 + 3 \cos^2 \beta_0 - 1} \quad [4.8]$$

b) Phenyl rings undergo small angle libration in the  $yz$  – plane (about x-axis), which means that  $C\hat{N}C$  angle (Figure 4.2) undergoes small changes. In this case, the transformation  $\Omega_{PM} = (0, \phi(t), 0)$ , averaged over the fast motion  $-\phi_0 \leq \phi(t) \leq \phi_0$  with

$P(\Omega_{PM}) = \frac{1}{2\phi_0}$  leads to

$$\langle \Omega_M \rangle = \frac{1}{2} \omega_Q \left[ \left( \frac{\sin 2\phi_0}{4\phi_0} - \frac{1}{2} \right) (1 - \eta_{PAS}) + 1 + \frac{\sin 2\phi_0}{2\phi_0} \right] \quad [4.9]$$

$$\langle \eta_M \rangle = \frac{\eta_{PAS} \left( \frac{\sin 2\phi_0}{4\phi_0} + \frac{3}{2} \right) - 3 \left( \frac{\sin 2\phi_0}{4\phi_0} - \frac{1}{2} \right)}{\left( \frac{\sin 2\phi_0}{4\phi_0} - \frac{1}{2} \right) (1 - \eta_{PAS}) + 1 + \frac{\sin 2\phi_0}{2\phi_0}} \quad [4.10]$$

c) Since the lineshape simulations using either of the above models could not reproduce the experimental lineshapes, a composite model of simultaneous librations in two arcs was considered. The coordinate transformation is schematically illustrated as

$$PAS \xrightarrow{(\alpha(t), \beta_0, 0)} MOL_1 \xrightarrow{(0, \phi(t), 0)} MOL_2 \xrightarrow{(\alpha_{ML}, \beta_{ML}, \gamma_{ML})} LAB$$

The averaged quadrupole parameters are found as follows:

$$\begin{aligned} \langle T_0^M \rangle = & \langle D_{00}^{M_1 M_2} \rangle \left( \langle D_{00}^{PM_1} \rangle T_0^{PAS} + \langle (D_{20}^{PM_1} + D_{-20}^{PM_1}) \rangle T_2^{PAS} \right) + \\ & \langle (D_{20}^{M_1 M_2} + D_{-20}^{M_1 M_2}) \rangle \left( \langle D_{02}^{PM_1} \rangle T_0^{PAS} + \langle (D_{-22}^{PM_1} + D_{22}^{PM_1}) \rangle T_2^{PAS} \right) \end{aligned} \quad [4.11]$$

$$\begin{aligned} \langle T_2^M \rangle = & \langle D_{02}^{M_1 M_2} \rangle \left( \langle D_{00}^{PM_1} \rangle T_0^{PAS} + \langle (D_{20}^{PM_1} + D_{-20}^{PM_1}) \rangle T_2^{PAS} \right) + \\ & \langle (D_{22}^{M_1 M_2} + D_{-22}^{M_1 M_2}) \rangle \left( \langle D_{02}^{PM_1} \rangle T_0^{PAS} + \langle (D_{-22}^{PM_1} + D_{22}^{PM_1}) \rangle T_2^{PAS} \right) \end{aligned} \quad [4.12]$$

So that,

$$A \equiv \frac{\text{Sin}2\phi_0}{2\phi_0}$$

$$\langle \Omega_M \rangle = \frac{\omega_Q}{8} \left\{ \begin{aligned} & (3A+1) \left( \frac{\eta_{PAS}}{2\alpha_0} \sin 2\alpha_0 \sin^2 \beta_0 + 3 \cos^2 \beta_0 - 1 \right) + \\ & + (1-A) \left( \frac{\eta_{PAS}}{2\alpha_0} \{ \sin 2\alpha_0 (1 + \cos^2 \beta_0) \} + 3 \sin^2 \beta_0 \right) \end{aligned} \right\} \quad [4.13]$$

$$\langle \eta_M \rangle = \frac{(3+A) \frac{\eta_{PAS}}{4\alpha_0} (\sin 2\alpha_0 (1 + \cos^2 \beta_0) + 3 \sin^2 \beta_0) + 3(1-A) \left( \frac{\eta_{PAS}}{2\alpha_0} \sin 2\alpha_0 \sin^2 \beta_0 + 3 \cos^2 \beta_0 - 1 \right)}{(6A+1) \left( \frac{\eta_{PAS}}{2\alpha_0} \sin 2\alpha_0 \sin^2 \beta_0 + 3 \cos^2 \beta_0 - 1 \right) + (1-A) \left( \frac{\eta_{PAS}}{2\alpha_0} \{ \sin 2\alpha_0 (1 + \cos^2 \beta_0) \} + 3 \sin^2 \beta_0 \right)} \quad [4.14]$$

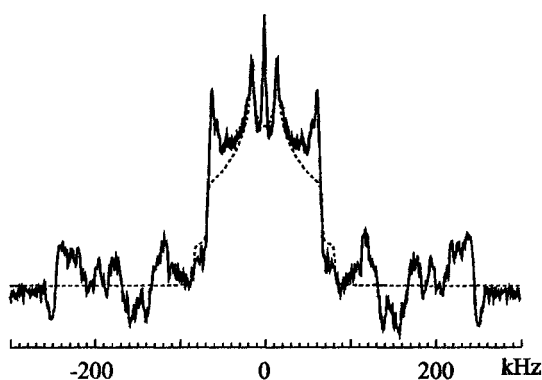
## 4.5 EXPRESS LINESHAPE SIMULATIONS

Data manipulations and simulations were performed on O2 Silicon Graphics workstations using the commercially available data visualization package PV-WAVE, and locally written programs. Exponential apodization corresponding to 1000 Hz Lorentzian broadening was applied to the time domain signal. The data then were left shifted, by spline interpolated fractions of a dwell time if necessary, so that a point

occurred precisely at the top of the echo. A zero order phase correction was used to minimize signal in the out-of phase channel. The small residual asymmetry in the Fourier transform spectra probably arises from instrumental artifacts not fully eliminated by phase cycling. All simulated lineshapes were multiplied by a factor

$$f(\nu) = \frac{\nu_0^2}{(\nu_0^2 + Q(\nu - \nu_0)^2)}, \text{ to correct for the finite bandwidth of the probe.}$$

FIGURE 4.4  
PRESATURATION POWDER PATTERN OF DEUTERATED EMERALDINE  
BASE AT AMBIENT TEMPERATURE



Experimental presaturation (solid line) and simulated (dashed line) spectra of deuterated emeraldine base at ambient temperature. Best fit was achieved with the following parameters:  $\omega_Q = 180$  kHz,  $\eta_{PAS} = 0.029$ ,  $k_{flip} \geq 3 \times 10^7$  s<sup>-1</sup>.

Simulated and experimental spectra of fast flipping rings for emeraldine base at ambient temperature are shown in Figure 4.4. Presumably, a more accurate representation could be obtained by including distributions of jump angles and rates<sup>72</sup>.

Since the powder pattern for fast flippers is fully narrowed at and above room temperature, lineshape analysis yields only a lower limit to the rate of flips,  $k_{flip} \geq 3 \times 10^7$  s<sup>-1</sup>. In view of the computer time required to generate one powder pattern (~50 sec of CPU time on a SGI O2 workstation), no attempt was made to automate the fitting procedure. Best fit quadrupole coupling and rate parameters for polyanilines are given in Table 4.1. The listed parameters give the best visual match to the observed lineshape. Quoted error bounds correspond to changes in quadrupole parameters, which noticeably increase the difference between experimental and simulated lineshapes.

TABLE 4.1

BEST FIT PARAMETERS FOR 180° FLIPS OF PHENYL RINGS IN POLYANILINES

$T, K$	material	$\omega_Q, \text{kHz}$	$\eta_{PAS}$	rate, s <sup>-1</sup>
297±0.05	EB	180±1	0.029±0.001	(1.5±0.1)×10 <sup>10</sup> (a)
	ES/HCl	180±1	0.043±0.001	>3 × 10 <sup>7</sup>
333±0.05	EB	180±1	0.029±0.001	>3 × 10 <sup>7</sup>
	ES/HCl	180±1	0.043±0.001	>3 × 10 <sup>7</sup>

(a) the rate listed here is based on  $T_{1Z}$  experiments described in Chapter 6.2

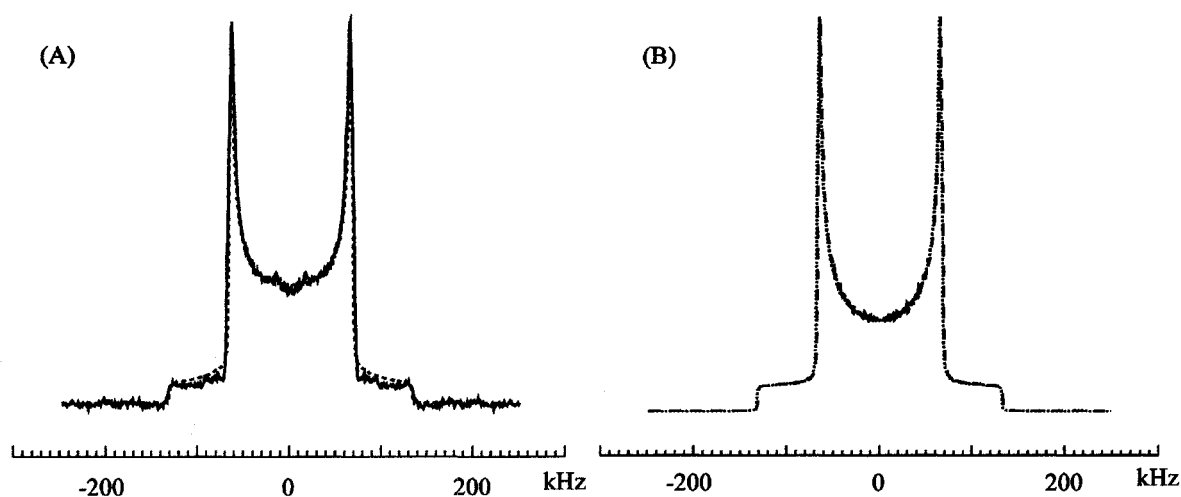
Comparison of the experimental room temperature emeraldine base powder pattern and the calculations for the four-site cone model is illustrated in Figure 4.5 (A). The dashed lines are simulated spectra, calculated using EXPRESS<sup>59,60</sup>. The fractions noted

in the figure caption represent the relative (integrated) intensities of the simulated line shapes for rigid and fast flipping phenyl rings, which best reproduce the observed equilibrium QE spectrum. The model of jumps among four unequally populated sites, ( $p_0, p_1, p_2, p_3$ ), defining a restricted asymmetric cone, was used for the rigid fraction. This model was necessary to reproduce the reduced intensity in the middle of the powder pattern relative to the horns. The asymmetric cone model insures a non-zero asymmetry parameter, and reproduces the curvature of the horns well. The input value of quadrupole coupling constant ( $\omega_Q$ ), 180 kHz, was reduced by the simulation algorithm to match the experimentally observed value, which was  $\Omega_Q = 171 \pm 1$  kHz for EB at ambient temperature. This corresponds to a cone angle  $15^\circ \pm 1^\circ$ . A distribution of cone angles (full width at half height of Gaussian distribution  $\sigma = 8^\circ$ ) was necessary to reproduce the broadening of the lineshape. Lineshapes simulated with a larger number of librational cone sites were not noticeably different from those with four sites.

As can be seen from Figure 4.5 (B), there are widely different values of the libration rate, which fit the lineshape equally well. The reason for this behavior can be understood by considering two typical isochromats, whose precession frequency differ by  $\Omega_Q$  radians in absence of jump motion. When they are interchanged by jumps, the deuteron powder pattern is a weighed sum of quadrupolar doublets, whose width is determined by the relative magnitudes of jump rate,  $k$ , and  $\Omega_Q(\alpha, \beta, \gamma)$  as outlined in theory of motional narrowing (Chapter 2.3.1). Thus the “best” fit value  $2.5 \times 10^9 \text{ s}^{-1}$  corresponds to librational collapse of the doublets, while  $3 \times 10^5 \text{ s}^{-1}$  implies broadening due to slow motion.

FIGURE 4.5

COMPARISON OF EXPERIMENTAL QE SPECTRUM OF EMERALDINE BASE  
WITH EXPRESS SIMULATIONS FOR FOUR-SITE CONE MODEL

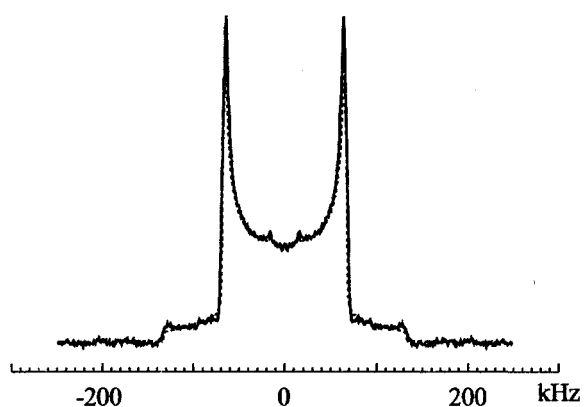


(A): Experimental (solid line) quadrupole echo spectrum of ring-deuterated emeraldine base at ambient temperature compared to EXPRESS simulations (dashed line) of the four-site cone model. The best fit achieved with the parameters:  $\omega_Q = 180$  kHz,  $\eta_{PAS} = 0.029$ ,  $k_{lib} = 3 \times 10^5$  s<sup>-1</sup>, cone angle = 15° with distribution  $\sigma = 8^\circ$ ,  $p_0 = 0.82$ ,  $p_1 = p_2 = p_3 = 0.06$ ,  $k_{flip} = 1.5 \times 10^{10}$  s<sup>-1</sup>, with 3% fast flippers. (B): Comparison of simulated powder patterns for the four-site cone model with all the same input parameters except the libration rate. The libration rate constant for the dashed line was  $k_{lib} = 3 \times 10^5$  s<sup>-1</sup>, and  $k_{lib} = 2.5 \times 10^9$  s<sup>-1</sup> for the dotted line.

The experimental spectrum with the two-frame model of libration in arcs, described in section 4.4 c) is shown in Figure 4.6. The simulation parameters are given in the caption. As can be seen by comparing Figures 4.5 and 4.6, both libration in a cone, with the distribution of the cone angles, and the libration in two arc frames describe the experimental data equally well. Therefore, the experimental lineshapes for the rigid component of emeraldine base at 333 K, emeraldine salt and polyaniline intercalated into clay nano-particles were described using the computationally less intensive four-site cone

model. The temperature dependence of the quadrupole coupling constant, asymmetry parameter, population distribution and cone angles for emeraldine base and salt are summarized in Table 4.2.

FIGURE 4.6  
COMPARISON OF EXPERIMENTAL QE SPECTRUM OF EMERALDINE BASE  
WITH EXPRESS SIMULATIONS FOR TWO-FRAME ARC LIBRATION MODEL



Experimental (solid line) quadrupole echo spectrum of ring-deuterated emeraldine base at ambient temperature compared to EXPRESS simulations (dashed line) of two-frame model of arc librations in a plane. The best fit achieved with the parameters:  $\omega_Q = 180$  kHz,  $\eta_{PAS} = 0.029$ ,  $\phi_0 = 5^\circ$ ,  $k_1 = 5 \times 10^5 \text{ s}^{-1}$ ,  $\alpha_0 = 5^\circ$ ,  $k_2 = 3 \times 10^9 \text{ s}^{-1}$ ,  $k_{flip} = 1.5 \times 10^{10} \text{ s}^{-1}$ , with 3% fast flippers.

A quadrupole echo spectrum of Pani intercalated into MMT clay is shown in Figure 4.7. The narrow feature in the middle of the spectrum is probably due to a small amount of relatively mobile, unreacted aniline- $d_5$  trapped in the clay during polymerization. Simulations of the rigid lattice powder pattern show that its quadrupole coupling constant ( $\omega_Q$ ) is 208 kHz, 15% larger than observed for ES and EB. This is also significantly larger than values reported for highly rigid crystalline materials<sup>74</sup>,

TABLE 4.2  
BEST FIT PARAMETERS FOR FOUR-SITE CONE MODEL OF RIGID  
COMPONENT OF POLYANILINES

T, K	material	% R <sup>(1)</sup>	$\omega_Q$ , kHz	$\eta_{PAS}$	$k_{lib}$ , s <sup>-1</sup>	$\langle\beta_J\rangle$ <sup>(2)</sup>	$p_0$
297±0.05	EB	97	180	0.029	$3\times 10^5$	15 ± 1	0.82
	ES/HCl	98.5	180	0.043	$2.7\times 10^5$	18 ± 1	0.85
333±0.05	EB	60	180	0.029	$8.5\times 10^4$	19 ± 1	0.85
	ES/HCl	82	180	0.043	$7\times 10^4$	18 ± 1	0.85

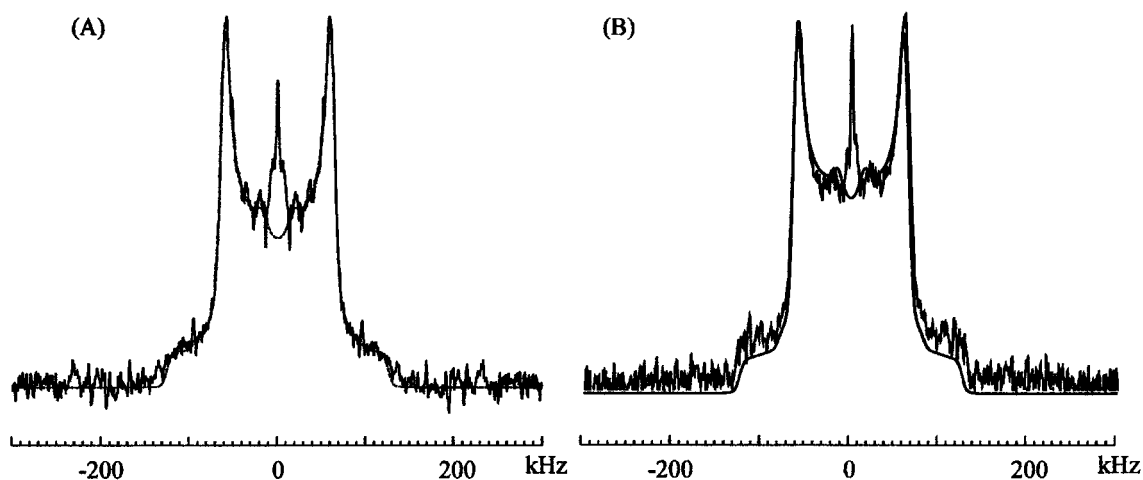
<sup>(1)</sup> %R is the fraction of rigid component

<sup>(2)</sup>  $\langle\beta_J\rangle$  is the mean cone angle; the distribution width was 8° for all samples at both temperatures

and probably reflects intermolecular contributions to the deuteron electric field gradient arising from nearby charges in the clay layers. These depend inversely on the cube of the distance from the deuteron to the center of charge, and the unusually large Gaussian broadening (9.6 kHz) needed to fit the line shapes is consistent with a dispersion of relevant distances and hence  $\omega_Q$  values. Some of the observed broadening may also be due to paramagnetic impurities in the clay.

FIGURE 4.7

EXPERIMENTAL QE SPECTRUM OF PANI/CLAY AT  $T = 297\text{K}$  AND  $333\text{K}$   
 COMPARED TO SIMULATIONS WITH THE FOUR-SITE CONE MODEL



Experimental (solid line) quadrupole echo spectrum of Pani/Clay nanocompound at  $T = 297\text{K}$  (A) and  $T = 333\text{K}$  (B) compared to EXPRESS simulations (dashed line) with the four-site cone model. The best fit for (A) was achieved with the parameters:  $\omega_Q = 208$  kHz,  $\eta_{PAS} = 0.033$ ,  $k_{lib} = 1.5 \times 10^7 \text{ s}^{-1}$ , cone angle =  $20^\circ \pm 4.7^\circ$ ,  $p_0 = 0.04$ ,  $p_1 = p_2 = p_3 = 0.32$ ,  $k_{flip} = 1 \times 10^7 \text{ s}^{-1}$ , with 15% fast flippers. The parameters for the best fit of the lineshape (B) were  $\omega_Q = 208$  kHz,  $\eta_{PAS} = 0.033$ ,  $k_{lib} = 1.5 \times 10^7 \text{ s}^{-1}$ , cone angle =  $20^\circ \pm 5.7^\circ$ ,  $p_0 = 0.04$ ,  $p_1 = p_2 = p_3 = 0.32$ ,  $k_{flip} = 1 \times 10^7 \text{ s}^{-1}$ , with 30% fast flippers.

For the Pani/clay sample the signal to noise ratio is not good enough to permit detection of a small fraction of fast flipping aromatic rings, and attempts to selectively saturate the wide powder pattern failed completely due to its short relaxation times ( $T_{1Z} \sim 6$  ms). The short relaxation times are an unfortunate consequence of the fact that montmorillonite clay has  $\sim 3$  wt % iron incorporated as defects in the silica layers. Another possible reason, which can account for both the broad  $\omega_Q$  distribution and short relaxation times is that Pani is incorporated in the clay in its electrically conducting salt form. Formation of a polaron band could increase the average value of electric field

gradients and the distribution width, and fast relaxation could arise from a Korringa-like relaxation mechanism. However, in view of the results described in Chapter 5, we believe that the latter possibility is unlikely.

## CHAPTER 5

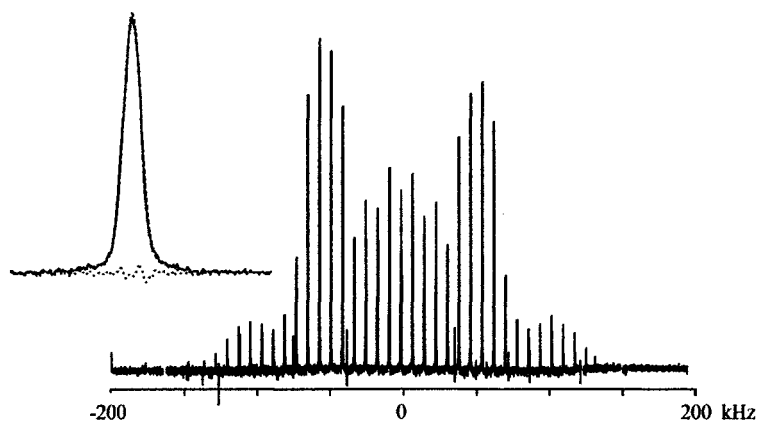
### MAGIC ANGLE SPINNING EXPERIMENTS

Magic angle spinning (MAS) is widely used technique designed to remove the line broadening due to anisotropic interactions in powder samples. It has been noted in Section 2.3.2 that a high resolution spectrum is retrieved provided that the spinning axis makes the “magic angle” with the direction of the static magnetic field and that the rotation frequency is much larger than the interaction to be removed. It turns out that the largest spinning frequency currently available (60-70 kHz) is still far too small to completely suppress the effects of quadrupolar coupling. Instead, one observes a set of narrow sidebands at integer multiples of the rotation frequency. The envelope of sideband intensities resembles the static powder pattern arising from quadrupole coupling, while the frequencies and width of the individual sidebands are independent of this interaction. Thus, small interactions, which are normally obscured by the much larger first order quadrupole coupling, are revealed in the MAS spectrum.

## 5.1 EMERALDINE BASE

The MAS spectra of EB at 263 K is shown in Figure 5.1. One spinning sideband is expanded in the inset; the others have similar shapes. The dashed line on the inset represents the best fit of the lineshape achieved by non-linear Levenburg-Marquardt least square fitting. A weighted sum of two Gaussians was chosen as the best model function. Details of simulations and analysis of the “goodness” of fit of the model function are summarized in Appendix A.

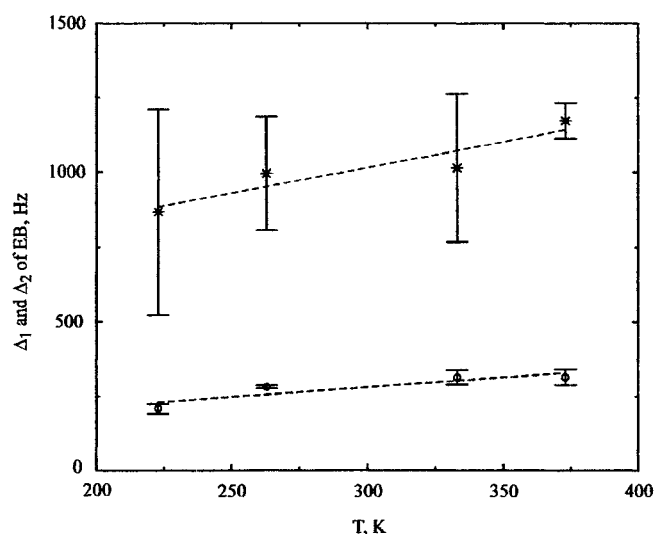
FIGURE 5.1  
EXPERIMENTAL DEUTERON MAS SPECTRUM OF EMERALDINE BASE AT  
263K



The spinning speed was 8 kHz. Insert illustrates a typical spinning sideband from the spectrum. The dashed line is the best fit, achieved by non-linear Levenburg-Marquardt iterations on a normalized, weighted sum of two Gaussians. The dotted line displays the residual.

To exclude possible influence of the “fast flippers” on data analysis (see Chapter 4.1), only sidebands at frequencies of absolute value greater than 48 kHz were analyzed. The center frequencies of the two Gaussians ( $\nu_1$  and  $\nu_2$ ) of the EB sample are the same within experimental error ( $\pm 22$  Hz) and do not depend on temperature. The relative integrated intensity of the wide peak is  $0.22 \pm 0.06$  and is temperature independent. In principle, this intensity might be underestimated due to more rapid, irreversible dephasing of the wide component at the time of the first rotational echo  $\tau_R = 125 \mu\text{s}$ .

FIGURE 5.2  
TEMPERATURE DEPENDENCE OF THE FULL WIDTHS AT HALF HEIGHT OF  
TWO PEAKS OF SPINNING SIDEBANDS OF EMERALDINE BASE



Temperature dependence of the full width at half heights of narrow  $\Delta_1$  (circles) and wide  $\Delta_2$  (stars) Gaussian components of emeraldine base. Dashed lines are drawn to guide the eye.

However, the two components were found to decay as single exponentials with the same time constant  $T_2$ , which decreases from  $2.00 \pm 0.004$  ms to  $0.95 \pm 0.02$  ms as temperature

increases from 223 to 373K. Presumably, the equality of  $T_2$  values for the two components is due to rapid spin diffusion.

The temperature dependence of the full widths at half height,  $\Delta$ , of both peaks is shown in Figure 5.2. Libration of C – D bonds over a range of angles results in an inhomogeneous spread of (quadrupolar) site frequencies,  $\Delta\omega_Q$ . If the libration rates are larger than the distribution width,  $k \gg \Delta\omega_Q$ , the MAS sideband linewidth should be proportional to  $(\Delta\omega_Q)^2/k$ <sup>58</sup>. Thus, for both broad and narrow components of the EB spectra, the observed increase in MAS linewidth can be ascribed to increasing librational amplitude (i.e. larger  $\Delta\omega_Q$ ) which more than compensates for the expected<sup>75</sup> linear temperature dependence of  $k$ . Alternatively, the MAS linewidth could be due to slow libration, in which case the linewidth is simply proportional to  $k$ . Discriminating between these two alternatives (slow libration versus fast) would require adopting untestable functional relations between the libration rate and amplitude. Due to low intensity of the wide Gaussian and consequently large uncertainties, a more detailed analysis of its linewidth is not warranted.

In the MAS spectra of emeraldine base, the observation of two components with the same frequency but different widths can be attributed to different librational rates and/or amplitudes of benzoid and quinoid rings. Since the relative intensities of the peaks do not change with temperature and the intensity ratio of narrow to wide peak is approximately equal to the ratio of amine to imine nitrogens (see Fig. 3.2), one can ascribe wide Gaussian to rigid quinoid rings, which are expected to have smaller libration amplitudes.

## 5.2 MAS OF CONDUCTIVE SAMPLES

Many authors have commented on the unfortunate loss of spectral resolution in  $^{13}\text{C}$  and  $^{15}\text{N}$  NMR of conducting polyaniline salts. For example, Kolbert *et al.*<sup>33</sup> reported observation of 60 ppm wide unresolved resonance for conductive emeraldine/CSA salt in  $^{13}\text{C}$  CP MAS NMR spectra. Any Knight shift, if present, would likely be obscured by the broadening. The origin of the broadening has never been convincingly determined. It has been suggested that it is due to the inhomogeneous distribution of charges over the polymer backbone<sup>40</sup>. In what follows, we show that the relatively narrow lines observed by deuteron MAS NMR are a welcome exception to this behavior, and can provide additional insight into the nature of the conductive polyaniline.

### 5.2.1 SPIN COUNT EXPERIMENTS

During our experimental work it was found that the highly conductive ES/CSA/m-cresol had an anomalously low  $^2\text{H}$  NMR signal. The loss of the signal intensity is due, at least in part, to high RF reflectance of the conductive sample, which is known as the “skin effect”. At high frequencies, electromagnetic waves propagating into a highly conductive medium show an exponential damping with distance<sup>51</sup>. This means that current flows only near the surface of the conductive sample and its penetration depth,  $d$ , is given by

$$d = \sqrt{\frac{2}{\mu\omega_0\sigma}} \quad [5.1]$$

TABLE 5.1  
BULK CONDUCTIVITY, CRYSTALLINITY AND  $^2\text{H}$  SPIN COUNTS<sup>1</sup>

Sample	$\sigma$ , (S/cm)	$I/I_0$ <sup>(1)</sup> , %	$I/I_0$ <sup>(1)</sup> $\times f$ , %	$C$ <sup>(2)</sup> , %
EB	$10^{-9}$	$100 \pm 2$	-	0
ES/HCl	0.15	$80 \pm 4$	$93 \pm 5$	$25 \pm 5$
50% ES/HCl in KBr	-	$80 \pm 6$	-	
25% ES/HCl in KBr	-	$74 \pm 3$	-	
ES/CSA/NMP	0.22	$49 \pm 5$	$60 \pm 6$	-
50 % ES/CSA/NMP in KBr	-	$56 \pm 4$	-	
ES/CSA/m-cresol	36.0	$\leq 5$	$\sim 45$	$30 \pm 6$
50% ES/CSA/m-cresol in KBr	-	$65 \pm 4$	-	
25% ES/CSA/m-cresol in KBr	-	$56 \pm 4$	-	

<sup>(1)</sup> Spin count experiments were conducted using quadrupole echo pulse sequence with  $3.2 \mu\text{s}$   $90^\circ$  pulses and  $\pm 250$  kHz spectral width. Integrated intensities,  $I$ , have been corrected for different number of acquisitions and different molar amount of material in the rotor, including doping of the repeat unit of EB ( $\text{C}_{24}\text{N}_4\text{D}_{16}\text{H}_2$ ).  $I_0$  refers to the intensity of a reference sample of emeraldine base.

<sup>(2)</sup>  $C$  stands for crystallinity

where  $\sigma$  is the conductivity of the sample,  $\mu$  is the magnetic permeability and  $\omega_0$  is the frequency of the penetrating radiation. The implication of the Eq. 5.1 is that the RF field strength, and hence the pulse flip angle, decreases exponentially with distance into the sample along the coil (rotor) axis. The skin effect can be minimized by dispersing the

sample in an inert (KBr) matrix as shown in Table 5.1. Confirmation that the loss of signal occurs, in part, due to RF reflectivity can be derived by assuming that spins in a small slab of thickness  $dx$  at a distance  $x$  from the end of the cylindrical rotor experience a flip angle  $\theta = \frac{\pi}{2} e^{-\frac{x}{d}}$ . It follows that the fraction of observable spins,  $f$ , is given by

$$f = \frac{I}{I_0} = \frac{1}{h} \int_0^h \text{Sin}\left(\frac{\pi}{2} e^{-\frac{x}{d}}\right) dx \quad [5.2]$$

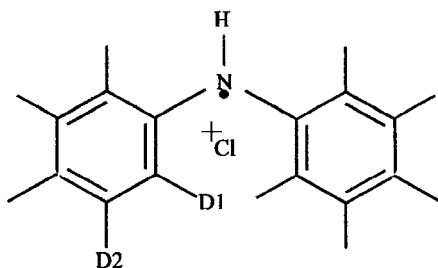
where  $I$  is the observed intensity,  $I_0$  is the intensity expected for infinite skin depth (non-conductive sample),  $h$  is the sample length and  $d$  is given by Eq. 5.1. Since the spin susceptibility of polyaniline is quite low ( $\chi = 2 \times 10^{-5}$  emu/mol (per two rings) at ambient temperature<sup>31</sup>), we can safely assume that  $\mu = (1 + \chi)\mu_0 \approx \mu_0 = 4\pi \times 10^{-7}$ . For our samples,  $h = 1.5 \pm 0.1$  cm and the calculated  $f$  drops from  $0.86 \pm 0.01$  for ES/HCl sample and  $0.82 \pm 0.01$  for ES/CSA/NMP to  $0.11 \pm 0.01$  for ES/CSA/m-cresol. Column 4 of the table 5.1 represents spin counts, corrected for signal loss due to skin effect ( $1/f$  is the correction factor). These data agree well with dilution spin count experiments within the experimental error (column 3).

It is evident from Table 5.1 that NMR experiments fail to see all of the spins in the conductive ES samples. Dilution of ES/HCl in KBr yields the same number of spins as in the pure sample, which implies that skin effect is not the reason for loss of signal in this sample. Dispersion of ES/CSA/m-cresol in the 50% of inert KBr, on the other hand, dramatically improves signal intensity but any further dilution (75 % KBr) produces the same number of spins as the 50% dispersion, within the experimental error. This observation can be interpreted as an effective removal of the skin effect by 50 % KBr dilution, for both the ES/CSA/m-cresol and ES/CSA/NMP samples.

The other reason for possible loss of signal intensity is fast irreversible dephasing before signal acquisition. This can be due to interaction between deuteron and the nearby unpaired electrons (localized polarons).

Experimental data for the spin count experiments were collected using the QE pulse sequence with  $t_1 = 50 \mu\text{s}$  (see Figure 3.8), so that signal was acquired 100  $\mu\text{s}$  after the initial pulse. Due to dipolar coupling with unpaired electrons,  $T_2$  of a deuteron in close proximity to the localized polaron can become very short, which would lead to

FIGURE 5.3  
SCHEMATIC REPRESENTATION OF TWO IN-PLANE RINGS OF THE  
CONDUCTIVE POLYANILINE



Geometric parameters, reported by Quillard *et al* are as follows: C-C = 1.41 Å, C-D = 1.06 Å, C=N = 1.42 Å. Bond angles have been chosen  $C\hat{N}C \approx C\hat{C}C = C\hat{C}D = C\hat{C}N = C\hat{N}H = 120^\circ$ .

rapid signal dephasing. The magnitude of  $T_2$  can be calculated from  $\frac{M(t)}{M_0} = e^{-t/T_2}$  (see

Chapter 2.3.3). If we assume that during first 100  $\mu\text{s}$  99 % or more of the signal is lost, then  $T_2$  for the “missing” spins must be less than  $2.2 \times 10^{-5}$  s.

Using the geometrical parameters for polyaniline, reported by Quillard *et al.*<sup>76</sup>, one can calculate distances N – D1  $\approx$  2.66 Å and N – D2  $\approx$  4.6 Å (see Figure 5.3). The dipolar coupling constant between localized electron spin and a deuteron 2.66 Å away (D1) is  $\omega_{D1} = \frac{\mu_0}{4\pi} \cdot \frac{\gamma_D \gamma_e \hbar}{r_{De}^3} = 4.33 \times 10^6$  rad/s, and  $\omega_{D2} = 0.785 \times 10^6$  rad/s for a deuteron 4.6 Å away (D2). Measurements of electron paramagnetic resonance<sup>39</sup> reveal that the electron spin-lattice relaxation time,  $T_{1e}$ , is between  $1.1 \times 10^{-7}$  and  $0.8 \times 10^{-7}$  s in powder ES/HCl samples with conductivities ranging from 1.7 to 56 S/cm. This time parameter is short relative to the reciprocal of dipolar splitting. According to the general theory of motional narrowing<sup>58</sup>, in the fast exchange limit (see Chapter 2.3.1) the spin-spin relaxation of the nucleus is given by

$$\frac{1}{T_2} = \frac{\omega_D^2}{2k_{1e}} \cdot p_1 \cdot p_2 \quad [5.3]$$

where  $k_{1e} = \frac{1}{T_{1e}}$  is the electron spin-lattice relaxation rate,  $p_1$  and  $p_2$  are populations of two electron energy levels. Since  $\frac{\hbar\omega_e}{k_B T} < 1$  (electron Larmor frequency,  $\omega_e$ , in the magnetic field of 7 T is  $1.24 \times 10^{12}$  Hz), one can show (see calculations in Chapter 3.3) that  $p_1 \cong p_2 \approx \frac{1}{2}$ . Thus, the spin-spin lattice relaxation time is simply  $\frac{1}{T_2} = \frac{\omega_D^2}{8k_{1e}}$ .

Calculations thus show that for deuterons 2.66 Å away from an unpaired electron charge  $T_2$  is  $5.83 \times 10^{-6}$  s, which make these deuterons invisible in our experiments. Moreover, any deuteron located within a sphere of radius = 3.3 Å from a localized electron will contribute less than 1% to NMR signal. Only 52% of the signal will be

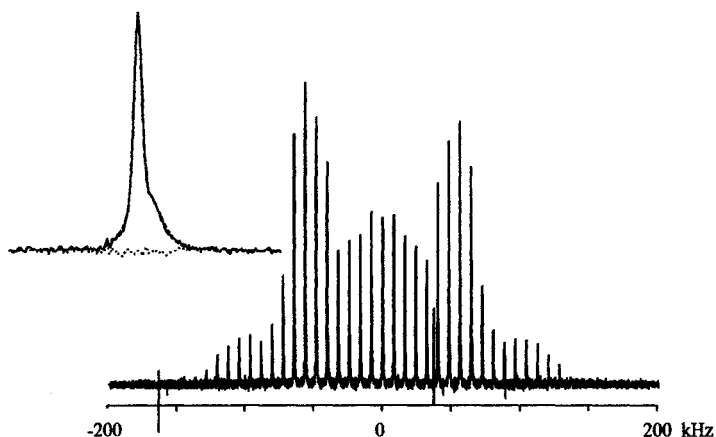
observed from the deuteron 5 Å away from the unpaired electron due to irreversible dephasing.

It was previously suggested <sup>42</sup>, that because of close correlation between the percent crystallinity and the percent of “missing” spins, the substantial signal decrease in the conductive Pani samples is due to the presence of delocalized unpaired electrons primarily in ordered crystalline regions, as well as in adjacent amorphous domains less than 50 Å away from the metallic crystalline islands. Calculations showing signal loss even from amorphous region were based on data, which were not corrected for skin effect. Our calculations described above, show that after corrections for high rf reflection, the low intensity of NMR signal in ES samples is due to coupling of localized unpaired electron spin with a deuteron. Since localized charge in the samples is thought to be disorder-induced <sup>24</sup>, we believe that that the signal is lost primarily from the amorphous region of the samples. This conclusion is also confirmed by our spin-lattice relaxation data, which will be described in Chapter 6.

## 5.2.2 EMERALDINE SALTS

The deuteron MAS spectrum of ES/HCl at 263K is shown in Figure 5.4. Individual sidebands of the conductive polymer have two Gaussian peaks (see inset), which are at the same frequency as those of EB. In addition they have a distinctive feature: a partially resolved third Gaussian peak whose center frequency is shifted upfield by  $5.7 \pm 1$  ppm (for simulation details see Table A1, Appendix A). Table 5.2 lists the temperature dependence of the fit parameters for the ES/HCl sample.

FIGURE 5.4  
 EXPERIMENTAL DEUTERON MAS SPECTRUM OF EMERALDINE  
 HYDROCHLORIDE



The spinning speed was 8 kHz, the temperature 263 K. The inset illustrates a typical spinning sideband. The dashed line is the best fit, achieved by non-linear Levenburg-Marquardt iterations on a normalized, weighted sum of three Gaussian functions. The dotted line displays the residuals.

The two unshifted peaks of ES are very similar to those of non-conductive EB, except the broad, unshifted Gaussian is wider (at 263K linewidth of the base is  $\Delta_2 = 997 \pm 190$  Hz, of the salt is  $\Delta_2 = 2915 \pm 1657$  Hz). The existence of the wide unshifted Gaussian in ES can be attributed to interaction of deuterons with localized polarons and/or bipolarons in emeraldine salt. The width of the line arises from the dipolar coupling between these spins, averaged by fast electron relaxation time,  $T_{1e}$ . The possibility of several overlapping Gaussians here, with small chemical shifts of their center frequency, cannot be excluded.

TABLE 5.2  
BEST FIT PARAMETERS FOR TEMPERATURE DEPENDENT  $^2\text{H}$  MAS SPECTRA  
OF EMERALDINE HYDROCHLORIDE

$T, \text{K}$	$I_1^a$	$\Delta_j^c, \text{Hz}$	$\Delta_3, \text{Hz}$	$\delta_3^d - \delta_j, \text{Hz}$	$\Delta_2, \text{Hz}$
223	$0.45 \pm 0.02^b$	$228 \pm 12$	$981 \pm 90$	$236 \pm 79$	$2465 \pm 2009$
263	$0.41 \pm 0.02$	$240 \pm 11$	$950 \pm 47$	$246 \pm 43$	$2915 \pm 1657$
333	$0.29 \pm 0.06$	$407 \pm 56$	$1077 \pm 120$	$303 \pm 83$	$2245 \pm 1573$
373	$0.24 \pm 0.03$	$371 \pm 39$	$1051 \pm 220$	$277 \pm 33$	$4000 \pm 3350$

<sup>a</sup>  $I_1$  is the normalized integrated intensity of the 1st (unshifted, narrow) Gaussian. The intensity of the unshifted wide peak ( $I_2$ ) was fixed at 25% of  $I_1$ . See Appendix A for the detailed explanation

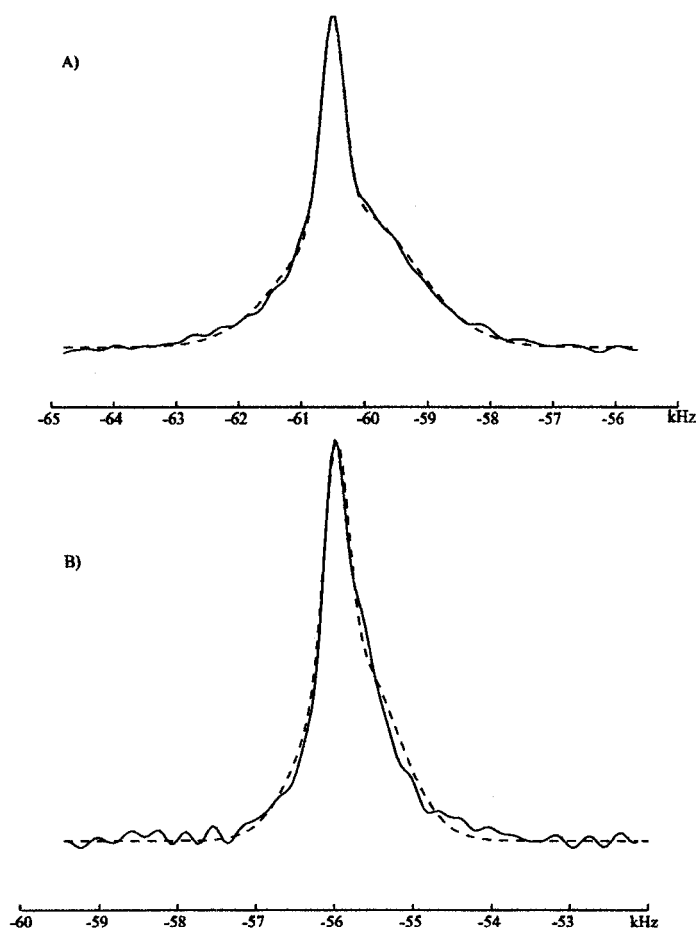
<sup>b</sup> uncertainty limits are the observed range of values measured independently from fits of three pairs of sidebands

<sup>c</sup>  $\Delta_j$  is the full width at the half height of Gaussian peak  $j$

<sup>d</sup>  $\delta_j$  is the shift from zero. The shift of a peak from zero frequency was calculated as an average of center frequencies of symmetric peaks on opposite site sides of the spectrum.

Even though samples of highly conductive ES/CSA/NMP and ES/CSA/m-cresol were diluted in KBr, the low signal-to-noise ratio in our experiments makes it difficult to obtain accurate quantitative results from the data. Room temperature spectra for ES/CSA/NMP and ES/CSA/m-cresol, where the intensity of the non-shifted narrow peak is less than 10%, were not simulated. The same consideration apply to the broad unshifted Gaussian peak, which was observed for ES/HCl (see Appendix A): if it exists,

FIGURE 5.5  
COMPARISON OF REPRESENTATIVE SPINNING SIDEBANDS OF ES/CSA/M-  
CRESOL AT TWO FIELD STRENGTHS



(A) Spinning sideband of ES/CSA/m-cresol at 223 K. Spinning speed was 10 kHz. The Spectrum was kindly obtained for us in Karlsruhe, Germany by Dr. Hans Foerster (Bruker Biospin, Inc.) using a 89 mm bore, 750 MHz Bruker magnet with AVANCE™ electronics. (B) Spinning sideband of ES/CSA/m-cresol at 223 K obtained on 300 MHz spectrometer. Spectra were fit with parameters listed in Table 5.3.

its intensity would be on the same level as noise, which does not allow any meaningful quantitative analysis for these samples. Therefore, spinning sidebands of ES/CSA/NMP

and ES/CSA/m-cresol were simulated as a sum of at most two Gaussians. To allow direct comparison of results from all three salt samples, ES/HCl was also simulated as a weighed sum two Gaussians, even though a low intensity peak(s), arising from fast dephasing spins, can be distinguished for this sample.

TABLE 5.3

BEST FIT PARAMETERS OF A SPINNING SIDEBAND OF ES/CSA/M-CRESOL,  
MEASURED USING 17.6 AND 7.0 T MAGNETIC FIELDS

$\omega_0$ , MHz	$I_1^{a,b}$	$\Delta_1^c$ , Hz	$\Delta_2$ , Hz	$\delta_1^d - \delta_2$ , ppm
115	$0.21 \pm 0.03$	$431 \pm 30$	$2325 \pm 229$	$4.9 \pm 1.5$
46	$0.21 \pm 0.02$	$305 \pm 21$	$1121 \pm 146$	$4.9 \pm 1.5$

<sup>a</sup>  $I_1$  is the normalized integrated intensity of the unshifted, narrow Gaussian peak.

<sup>b</sup> uncertainty limits are the observed range of values measured independently from fits of three pairs of sidebands

<sup>c</sup>  $\Delta_j$  is the full width on the half heights of Gaussian peak  $j$

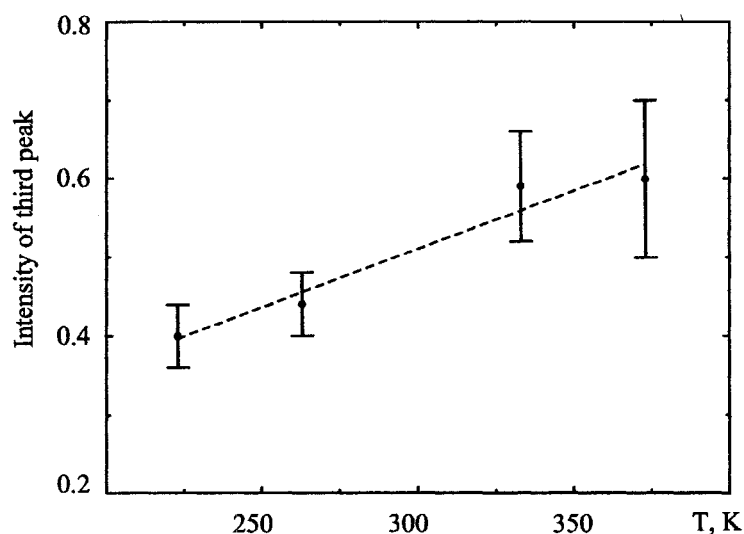
<sup>d</sup>  $\delta_j$  is the shift from zero. The shift of a peak from zero frequency was calculated as an average of center frequencies of symmetric peaks on opposite site sides of the spectrum.

An attractive solution, which would allow signal-to-noise ratio improvement, is the use of higher magnetic fields. Preliminary experiments at 115 MHz show significant resolution improvement for a 50% mixture of ES/CSA/m-cresol and KBr at 223 K as illustrated in Figure 5.5. It is clear that the improved resolution is (at least partially) due to the fact that the width of the shifted, broad peak scales approximately with the field ( $46 \text{ MHz} / 115 \text{ MHz} = 1 / 2.5$ ), while that of the narrow peak does not. The width at the

half maximum of the shifted peak is approximately 20 ppm and independent of temperature. It is likely that this arises from a heterogeneous charge density distribution  
77,78

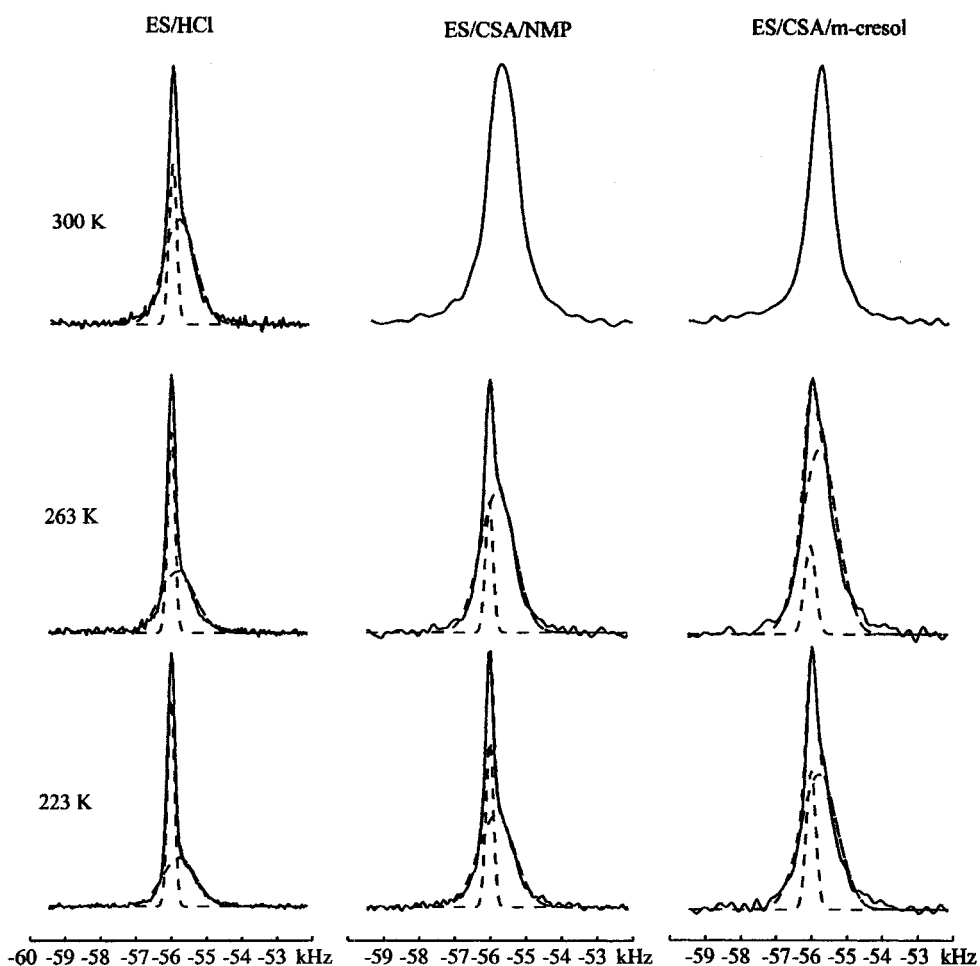
Temperature dependence of the relative integrated intensity of the shifted peak for ES/HCl sample is shown in Figure 5.6. These intensities have not been corrected for  $T_2$ ; the calculations described in Appendix B show that the correction (5%) would be inconsequential. It is interesting and important to note that the conductivity of the sample increases as temperature is raised.

FIGURE 5.6  
TEMPERATURE DEPENDENCE OF THE INTEGRATED INTENSITY OF THE  
SHIFTED PEAK OF SPINNING SIDEBANDS OF ES/HCL



Comparison of individual spinning sidebands of all three conductive samples at different temperatures is illustrated in Figure 5.7. At room temperature only the shifted

FIGURE 5.7  
 COMPARISON OF INDIVIDUAL SPINNING SIDEBANDS OF THREE  
 CONDUCTIVE SALTS AT DIFFERENT TEMPERATURES



Individual spinning sidebands of ES/HCl ( $\sigma = 0.15$ ), ES/CSA/NMP ( $\sigma = 0.22$ ) and ES/CSA/m-cresol ( $\sigma = 36$ ), at 223 K, 262K and 300 K. Solid lines represent experimental data. Dashed lines are the best fits, achieved by nonlinear Levenburg-Marquart iterations on a normalized sum of two Gaussians, which are shown with appropriate weights. The spinning speed was 8 kHz.

set of sidebands is observed for the more conductive ES/CSA/NMP and ES/CSA/m-cresol samples (within the experimental error). Solid lines represent experimental data, and dashed lines are best fits (nonlinear Levenburg-Marquart iterations) on a normalized Gaussian (EB) or weighted sum of Gaussians (ESs).

For all three samples the intensity of the narrow Gaussian, whose center frequency occurs at the same frequency as for non-conductive base, decreases as temperature increases. The reverse is observed for the shifted Gaussian: its intensity increases as temperature increases. Also, it becomes obvious that the intensity of the shifted peak increases with increasing bulk conductivity of a sample.

The magnitude and direction of the shift are consistent with a small hyperfine interaction between aromatic deuterons and spins of delocalized electrons (Knight shift). However, interpretation of this observation as a Knight shift is controversial.

Before accepting the Knight shift hypothesis, it is necessary to consider whether the observed shift in conductive ES arises from bound polarons (paramagnetic shift) or delocalized ones (Knight shift).

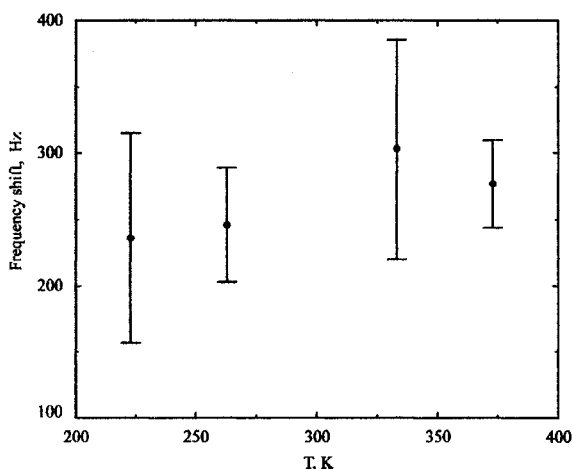
The susceptibility of doped Pani shows both temperature dependent and temperature independent components:

$$\chi = \chi_{Pauli} + \chi_{Curie} = \chi_{Pauli} + \frac{C}{T} \quad [5.4]$$

These components arise from isolated polarons and conduction electrons respectively. The equation 5.4 is not valid over the entire temperature range<sup>31</sup>; a qualitative change in spin susceptibility behavior is usually observed at some critical temperature,  $T_c$ . The value of  $T_c$  depends on conductivity of the sample, which is highly dependent on the conditions of the synthesis and processing methodology.

As the Knight shift is a function of the interaction between the nuclei and the conduction electrons, the magnitude of the Knight shift is a function of the magnitude of the Pauli susceptibility. In the ES/CSA/m-cresol system with conductivity and percent crystallinity similar to our material, Joo<sup>24</sup> found that the susceptibility does not change, within error, over the temperature range of 223 – 300 K.

FIGURE 5.8  
TEMPERATURE DEPENDENCE OF THE SHIFT FROM ZERO FREQUENCY FOR  
EMERALDINE HYDROCHLORIDE



It was calculated as an average of center frequencies of symmetric shifted sidebands on opposite sides of the spectrum:  $(\delta_n - \delta_n)/2$ , where  $n$  is the sideband number.

The temperature dependence of the shift frequency for the least conductive ES/HCl sample is illustrated in Figure 5.8. Within the experimental error it does not depend on temperature or, at most, increases slightly with temperature, within the measured temperature range. If the shift was due to interaction of a deuteron with

localized electrons, according to the Equations 2.55a and 2.56 the shift frequency would decrease and temperature was raised.

These considerations support the hypothesis that the origin of the shift in conductive Pani is the hyperfine coupling of deuterons with the delocalized charge carriers, i.e. a Knight shift.

A shifted broad peak in  $^{13}\text{C}$  CP/MAS NMR was observed previously by researchers, studying another conductive polymer, polyacetylene. Peo *et al* <sup>79</sup> have reported an observation of a sudden change in the spectrum of  $\text{AsF}_5$  – doped  $(\text{CH})_x$  as doping concentration reached 7%, where a broad downfield shifted peak appeared. This was attributed to a Knight shift, in accord with the observation of an abrupt increase in the Pauli susceptibility at the same doping concentration. Clarke and Scott <sup>80</sup>, however, observed a broad shifted peak for doping levels below 7% of  $\text{AsF}_5$ , and suggested that the primary cause of the downfield shift is the removal of electrons from the  $\pi$  system, and that the Knight shift presents a much smaller contribution superimposed on this chemical shift. Later on, Terao <sup>78</sup> and coworkers investigated  $\text{AsF}_5$ -,  $\text{K}$ -,  $\text{I}$ - and  $\text{Br}$ -doped polyacetylene. Their theoretical calculations and experimental results confirmed that the magnitude, width and direction of the observed shifted peak are consistent with chemical shifts originating from changes in  $\pi$  electron density.

On the other hand, in our study we analyzed the half-oxidized state of polyaniline, emeraldine. The base form of emeraldine is intrinsically insulating. Protonation of emeraldine base leads to increase of conductivity but does not change the number of electrons in the  $\pi$  system, thus, insulating emeraldine base and highly conductive emeraldine salt have the same number of  $\pi$  electrons. Moreover, the relative intensity of

chemically shifted peak does not depend on temperature, unlike the observed behavior of the shifted peak intensity, described above (Figure 5.6).

Accepting the fact that the origin of the shift is the hyperfine coupling of deuterons and delocalized electron spins, the experimental temperature dependence of the shifted peak intensity can be explained using models of amorphous semiconductors, described in Chapter 1.2. At low temperatures, because of inhomogeneous morphology of the polymer, disorder-induced localization of charge carriers is dominant; this results in low intensity of the shifted peak. As temperature increased, phonon-induced delocalization and percolation among “conductive islands” occurs. Consequently, more deuteron spins are coupled with charge carriers, producing a more intense shifted peak. With improved processing, samples with higher conductivity could have larger “metallic islands” and they could be situated closer to each other<sup>24</sup>. Thus lower temperature would be required to induce charge delocalization and the intensity of the shifted peak is expected to be higher at lower temperatures as compared to less conductive samples, which could be directly observed by NMR (Figure 5.7). The observation that at ambient temperature the highly conductive ES/CSA/NMP and ES/CSA/m-cresol films have most of the intensity in the shifted peak implies that the charge is delocalized over the entire samples.

This interpretation agrees with Joo *et al.*<sup>24</sup>, who suggested, based on measurements of microwave dielectric constant and XRD measurements, that the charge delocalization occur over several metallic islands. In his model, as temperature increases, quasi-1D polymer chains in disordered inter-island regions can become more aligned, thereby contributing to charge delocalization.

At the same time relatively small magnitude of the observed Knight shift suggests that only a small fraction of the charge carriers is delocalized. This agrees with Kohlman's <sup>19</sup> conclusions based on an unscreened free carrier plasma frequency measurements.

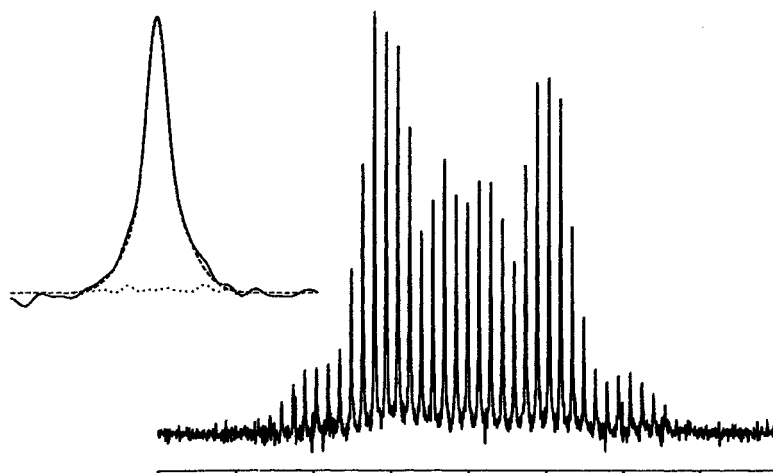
On the other hand, there is a possibility that as temperature increases spinless localized bipolarons, if present, may dissociate to form polarons, and the local polarons may become part of a polaron band. Even though the transition of a bipolaron to two polarons is not energetically favorable for many conductive polymers <sup>29</sup>, formation of an ordered array of polarons can be stabilized by the energy gained through delocalization and decreased Coulomb repulsion. In this case the number of conduction electrons increases slightly with temperature. Thus, one might expect a small increase in the Knight shift frequency in accordance with Bloembergen's formula (Equation 2.57), which states that the Knight shift is proportional to the charge carrier density. Quantitative analysis of this effect is impossible because of limited temperature range of the experimental instrumentation and low signal-to-noise ratio of the samples. These limitations may be improved with the use of higher magnetic field and improved MAS probes.

The observation of the deuteron Knight shift in NMR experiments has an important implication for the theory of electrical conduction in polyaniline: it proves that polarons are the charge carriers.

### 5.3 PANI/CLAY INCLUSION COMPOUND

A typical MAS spectrum of Pani/Clay is shown in Figure 5.9. The best model function for simulating this spectrum was found to be a weighted sum of two Gaussians (dashed line in the insert of Fig. 5.9, for details see Appendix A). The best fit parameters

FIGURE 5.9  
EXPERIMENTAL DEUTERON MAS SPECTRUM OF PANI/MMT CLAY  
NANOCOMPOSITE AT 263K



The insert illustrates a spinning sideband of the spectrum. Dashed line is the best fit, achieved by non-linear Levenburg-Marquardt iterations on a normalized, weighted sum of two Gaussian functions. Dotted line is the difference between the experimental and calculated data. The spinning speed was 7.5 kHz.

are listed as functions of temperature in Table 5.4. Due to the low concentration of deuterated polymer in the clay quantitative analysis of the Pani/Clay MAS spectra was

complicated by very low signal-to-noise ratio. Furthermore, Montmorillonite clay contains a small weight percent of iron ( $Fe^{2+}$  and  $Fe^{3+}$ ) which significantly broadens the deuterium NMR spectra.

TABLE 5.4  
BEST FIT PARAMETERS FOR TEMPERATURE DEPENDENT  $^2H$  MAS SPECTRA  
OF PANI/CLAY

$T, K$	$I_1^a$	$I_2^a$	$\Delta_1^c, Hz$	$\Delta_2, Hz$	$\delta_1^d, Hz$	$\delta_2^d, Hz$
223	$0.36 \pm 0.04^b$	$0.64 \pm 0.04^b$	$559 \pm 83$	$1960 \pm 559$	$27 \pm 5$	$15 \pm 18$
263	$0.39 \pm 0.07$	$0.61 \pm 0.07$	$555 \pm 58$	$1831 \pm 437$	$15 \pm 10$	$50 \pm 22$
333	$0.42 \pm 0.06$	$0.58 \pm 0.06$	$626 \pm 79$	$2089 \pm 457$	$18 \pm 9$	$20 \pm 24$
373	$0.44 \pm 0.06$	$0.56 \pm 0.06$	$714 \pm 70$	$2124 \pm 468$	$22 \pm 10$	$19 \pm 15$

<sup>a</sup>  $I_j$  is the normalized integrated intensity of the  $j$ -th Gaussian.

<sup>b</sup> uncertainty limits are the observed range of values measured independently from fits of tree pairs of sidebands

<sup>c</sup>  $\Delta_j$  is the full width on the half heights of Gaussian peak  $j$

<sup>d</sup>  $\delta_j$  is the shift from zero. The shift of a peak from zero frequency was calculated as an average of center frequencies of symmetric peaks on the opposite site sides of the spectrum.

The width of the narrow peak increases with temperature from  $\Delta_1 = 559 \pm 83$  Hz at 223K to  $\Delta_1 = 714 \pm 70$  Hz at 373K. The width of the wide peak exhibits at most a very weak temperature dependence (see Table 5.4). Fast relaxation in the sample ( $T_{1z} = 6ms$ ) can account for the temperature dependence of the linewidth. The center frequencies of

both peaks are the same and are temperature independent. One might expect to observe a third, shifted peak for ES intercalated into MMT. Unfortunately, poor signal to noise ratio and pronounced broadening of the sidebands precludes this level of the spectral analysis. If present, the extra set of shifted spinning sidebands would be difficult to observe due to high intensity of the broad unshifted Gaussian (see Table 5.4). Qualitatively, the Pani/Clay sidebands are similar to those of non-conductive EB, even though the conditions of synthesis were optimized for formation of conductive emeraldine salt. The lack of an observable Knight shift in Pani/Clay may possibly be a consequence of quasi-2D confinement of the polymer, which prevents formation of three dimensional metallic islands<sup>24</sup>.

## CHAPTER 6

# DEUTERON RELAXATION TIME ANISOTROPY OF POLYANILINES

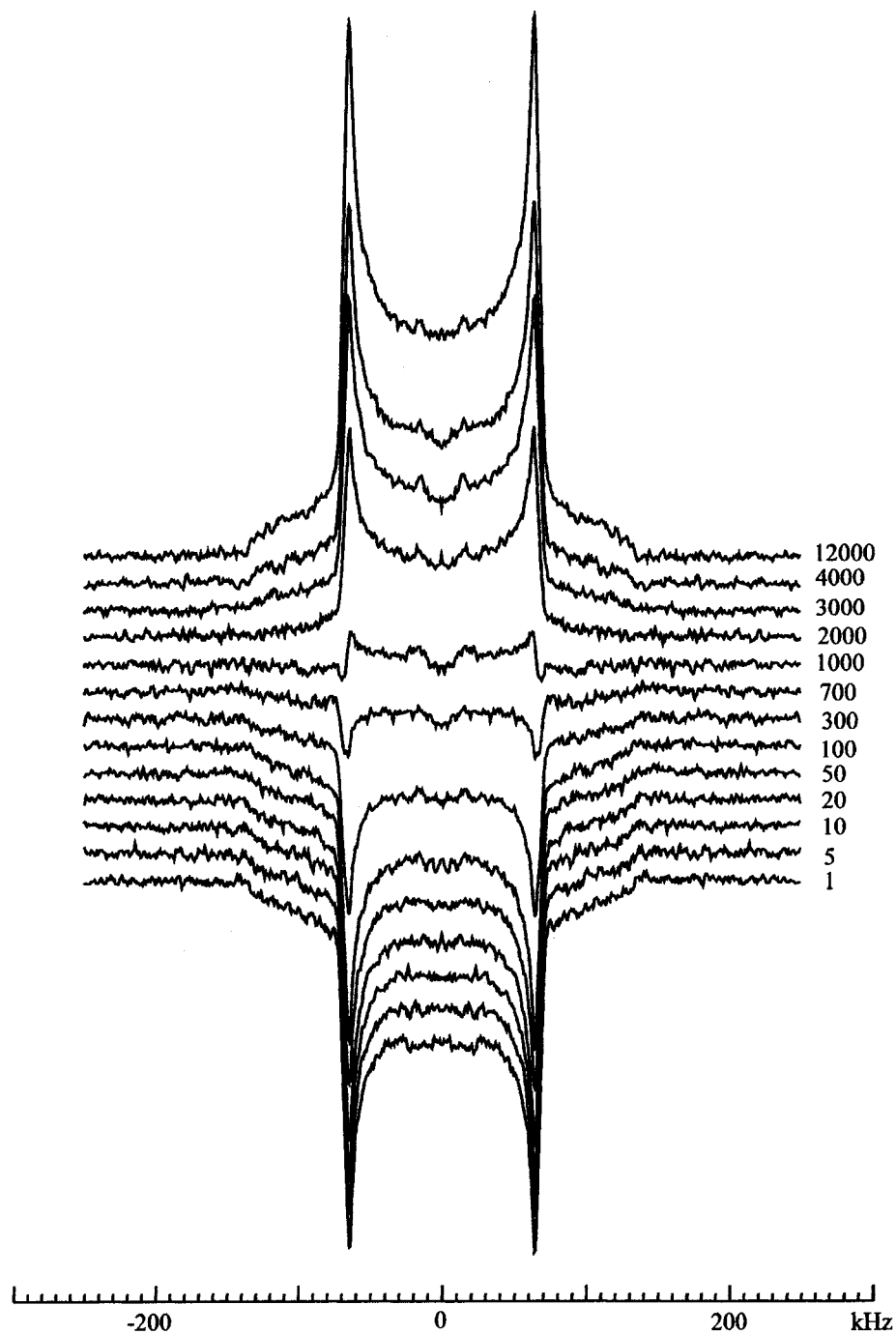
In this chapter motional models, described in Chapter 4, are used to simulate the anisotropic  $T_{1Z}$  and  $T_{1Q}$  relaxation data. For polymeric molecules, where molecular motion can occur on a wide range of timescales, interpreting quadrupole echo lineshape combined with Zeeman relaxation times,  $T_{1Z}$ , can still yield ambiguous results. Simultaneous measurements of the orientation dependence of the quadrupole order relaxation time,  $T_{1Q}$ , are required to provide a more accurate description<sup>60,81</sup>.

### 6.1 EXPERIMENTAL DATA

For all  $T_{1Z}$  experiments the standard non-selective inversion recovery pulse sequence was used with quadrupole echo detection (Figure 3.8) and a 16 step phase cycle<sup>60</sup>. For experiments done with the Chemagnetics probe with quality factor

FIGURE 6.1

EXPERIMENTAL INVERSION RECOVERY SPECTRA OF EMERALDINE BASE  
AT AMBIENT TEMPERATURE AS A FUNCTION OF THE RELAXATION DELAY

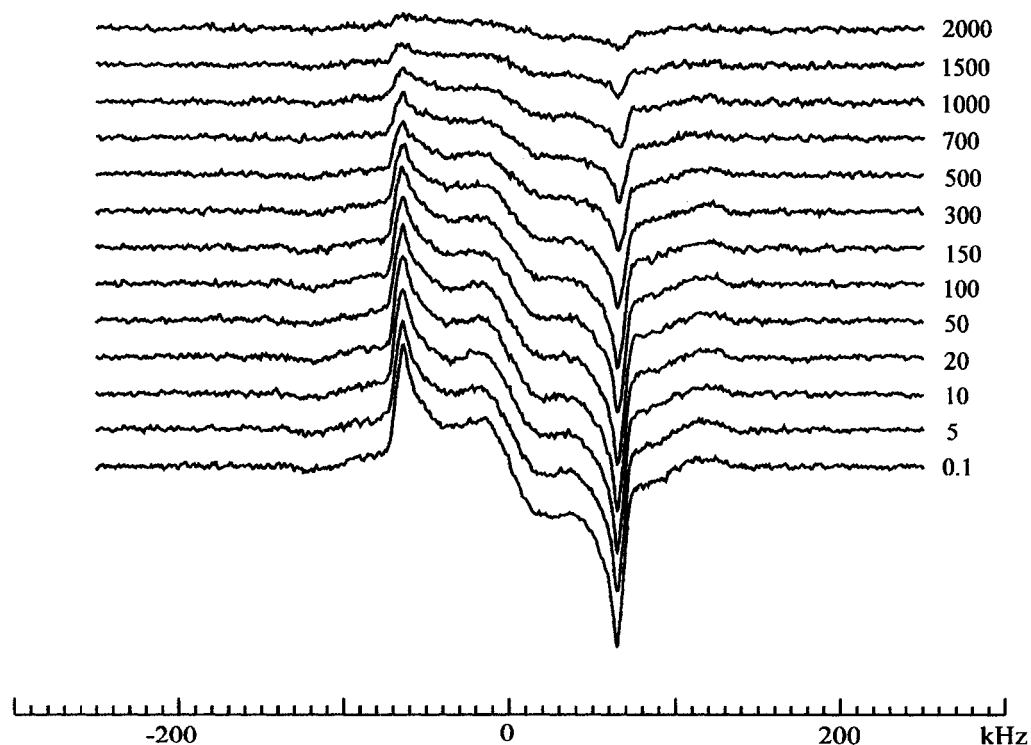


Relaxation delay,  $\tau$ , for each partially relaxed spectrum is shown in milliseconds

of 220, composite  $180^\circ$  pulses<sup>70</sup> were necessary (Chapter 3.3.3) to achieve uniform spectral excitation. Typically, adequate signal to noise ratios were obtained by accumulating 800 transients of 1024 complex data points for 13 different  $\tau$ -delays. The pre-acquisition delay was varied so as to place a sampling point precisely at

FIGURE 6.2

EXPERIMENTAL  $T_{1\rho}$  LINESHAPES OF EMERALDINE BASE AT AMBIENT TEMPERATURE AS A FUNCTION OF THE RELAXATION DELAY



Relaxation delay,  $\tau$ , for each partially relaxed spectrum is shown in milliseconds.

the top of the quadrupole echo. In most experiments a 40 or 50  $\mu\text{s}$  delay between pulses was needed to shift the echo outside the spectrometer dead time. A representative partially relaxed spectra collected from inversion recovery experiment for emeraldine base are illustrated in Figure 6.1.

Since each relaxation experiment took approximately 2 days, only ambient temperature measurements could be performed with reasonable accuracy.

The broad-band Jeener-Broekaert pulse sequence (Figure 3.12) with 32 step phase cycle<sup>60</sup> was used for  $T_{IQ}$  anisotropy measurements (Figure 6.2). The experimental conditions for  $T_{IQ}$  experiments were the same as those described above for  $T_{IZ}$ . A  $t_{ex}$  value (Figure 3.12) of 3  $\mu\text{s}$  was chosen to achieve uniform excitation of the quadrupole order across the frequency range from 30 to 100 kHz.<sup>60</sup> The last delay before acquisition was adjusted to obtain a point at the zero crossing for the imaginary signal component. A representative partially relaxed spectra from a  $T_{IQ}$  experiment is illustrated in Figure 6.2.

## 6.2 EMERALDINE BASE RELAXATION

For linear polymers, such as polyaniline, wide distributions of motional parameters are typical and can in many cases result in non-exponential relaxation behavior. However, phenomenological distribution functions, which can be used to parameterize the relaxation of the total magnetization, are often not adequate to account for orientational anisotropy of the relaxation times<sup>59,60,81</sup>. Due to high polydispersity of the studied Pani materials, a substantial distribution of motional parameters was expected. As a first step of analysis, the observed multi-exponential character of the

recovery curves can be assumed to originate from single exponential contributions of overlapping spectral features:

$$M_{\infty}(\nu) - M_{\tau}(\nu) = \sum_{i=1}^N I_i (m_{\infty}^{(i)} - m_{\tau}^{(i)}) e^{-\frac{\nu}{T_{1z}^{(i)}}} \quad [6.1]$$

Here,  $M(\nu)$  is the overall spectral signal intensity at frequency  $\nu$  (with maximum intensity normalized to 1),  $m(\nu)$  is the signal intensity of a contributing feature (with integrate intensity normalized to 1),  $I^{(i)}$  is a weight of  $i$ -th overlapping component, which was determined from the static QE lineshape deconvolution, described in Chapter 4.

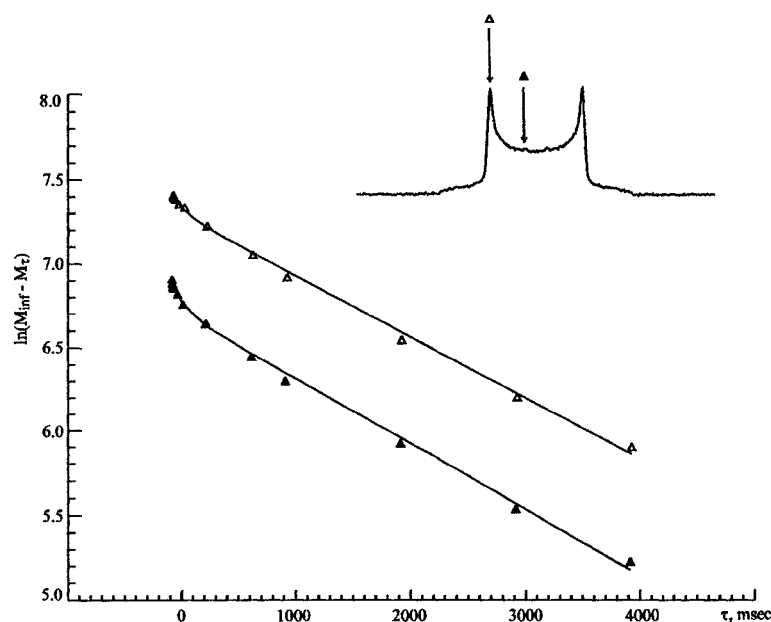
As can be seen from Chapter 4, emeraldine base lineshape consists of at least two overlapping powder patterns ( $N = 2$ ), one of which can be ascribed to fast  $\pi$ -flippers, while the other corresponds to rigid rings. The motional model for the rigid component as well as the rate of motion cannot be determined unambiguously from QE lineshape simulations alone. For example, it was shown (Chapter 4.5) that the two-frame model of correlated jumps in two arcs and the model of asymmetric four-site cone give superimposable powder patterns. Furthermore, the experimental rigid powder pattern of emeraldine base at room temperature could be fit equally well with cone librational rates  $k_{lib} = 3 \times 10^5$  and  $2.5 \times 10^9$ .

Typical recovery curves for emeraldine base at two different points on the lineshape ( $\nu = 15.38$  and  $64.21$  kHz) are shown in Figure 6.3. It can be seen that the experimental recovery curve at frequency  $15.38$  kHz has more pronounced multi-exponential character, with higher percentage of the fast component. The solid line represents the best fit to the experimental data (symbols), obtained using an unconstrained bi-exponential function of the form:  $A_f e^{-\frac{t}{T_{1z}^f}} + (1 - A_f) e^{-\frac{t}{T_{1z}^s}}$ , where

subscripts  $f$  and  $s$  denote fast and slow components respectively. The fit was accomplished by first choosing the slope change point,  $t_c$ , for a recovery curve, and fitting the data for  $t > t_c$ , the slowly relaxing magnetization component  $M_t^s$ , to a single exponential using least square fit procedure. Then, the calculated contribution of  $M_t^s$  was

FIGURE 6.3

COMPARISON OF EXPERIMENTAL AND UNCONSTRAINED BI-EXPONENTIAL  
 $T_{1Z}$  RECOVERY CURVES FOR EMERALDINE BASE



Experimental (symbols) and unconstrained bi-exponential (solid lines)  $T_{1Z}$  recovery curves for emeraldine base. Filled symbols correspond to data from 15.38 kHz, and open symbols to 64.21 kHz.

subtracted from the total experimental intensity at  $t < t_c$ , and a single exponential fit was performed for the remaining fast relaxing component  $M_t^f$ . This procedure is mathematically rigorous only if  $T_{1Z}^s \gg T_{1Z}^f$  and it is described in detail in ref. <sup>57</sup>.

Unconstrained bi-exponential fitting provides fast and slow relaxation rates at each frequency point, but the best fit rates depend on the choice of the “crossover” time,  $t_c$ . When bi-exponential fitting is performed for experimental and EXPRESS simulated data sets for a few  $t_c$  values chosen around the middle of the recovery curves, the best approximation to  $T_{IZ}$  values is obtained when resulting experimental and simulated anisotropies coincide for as many  $t_c$  's as possible. This procedure also yields an estimate of the uncertainty in  $T_I$ , associated with the fitting protocol.

Even though unconstrained bi-exponential fits do not bear much physical significance, they provide a first approximation to two “effective” relaxation anisotropies. This allows comparison of experimental  $T_{IZ}$  and  $T_{IQ}$  relaxation data with anisotropies simulated using different models, and makes it possible to visualize the accuracy of the models and fit parameters. The calculation of relaxation time anisotropies is computationally intensive and takes, on average, 40 minutes of CPU time on SGI O2 to compute one set of recovery curves. Thus, the quadrupole coupling parameters, librational amplitudes and relative intensities of spectral features, originating from fast-flipping and rigid rings, were held constant and only the relevant motional rates were varied.

Analysis of relaxation anisotropies of emeraldine base was accomplished in several stages. First, simulations of the orientation dependence of  $T_{IZ}$  and  $T_{IQ}$  for the slow component from the bi-exponential fit were tried for all models described in chapter 4. The two-frame model of correlated jumps in two arcs, which produces a good fit of experimental lineshape for rigid rings, failed to simultaneously reproduce qualitatively or quantitatively the behavior of  $T_{IZ}$  and  $T_{IQ}$ . However, the unequally populated four-site

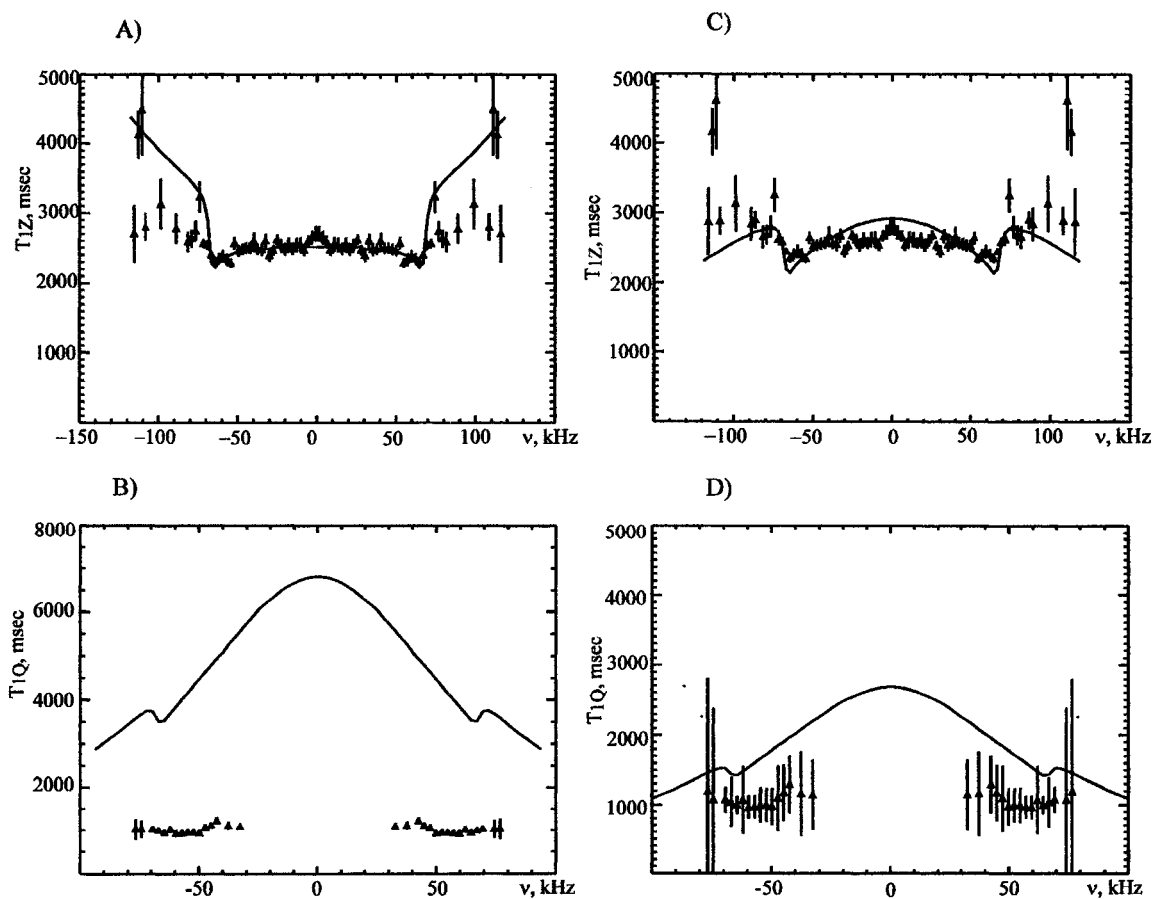
cone model provided an adequate description of both deuteron relaxation time anisotropies.

An illustrative example of the efficiency of data analysis by the bi-exponential deconvolution method is illustrated in Figure 6.4. As can be seen (Fig. 4.5 and Fig. 6.4 (A) and (B)), even though lineshape and  $T_{1Z}$  orientation dependence of a four-site cone jump model with  $k_{lib} = 2.5 \times 10^9 \text{ s}^{-1}$  describes the experimental data satisfactory, the predicted  $T_{1Q}$  is too long. On the other hand, slow librational motion in a cone with the rate  $k_{lib} = 3 \times 10^5 \text{ s}^{-1}$  is in satisfactory agreement with all three experiments (Fig. 4.5 and Fig. 6.4 (C) and (D)). More complex models, where slow cone libration is accompanied by fast libration in an arc or slow  $\pi$ -flips did not improve the fit of  $T_{1Q}$  relaxation anisotropy.

As the next step in the analysis of relaxation behavior, one can add a rate distribution to the slow rate found as described above. This can be done best by comparing the experimental and simulated recovery curves across the lineshape, trying to minimize the global differences. For frequencies  $|\nu| > 65 \text{ kHz}$  the intensity of fast  $\pi$ -flippers is negligible (Figure 4.4), so that a distribution of four-cone jump is appropriate. Experimental  $T_{1Z}$  recovery curves for emeraldine base at ambient temperature for three representative frequencies are shown in Figure 6.5. For each frequency, single exponential (dashed lines) fits, with the parameters given in figure caption, are compared to constrained multi-exponential fits (solid lines). The multi-exponential fit was found as described below.

Most descriptions of relaxation rates and motional processes in polymers are based on log-normal distribution of rates or its empirical variations<sup>57</sup>.

FIGURE 6.4  
 UNCONSTRAINED BI-EXPONENTIAL FIT FOR EXPERIMENTAL AND  
 SIMULATED  $T_{1Z}$  AND  $T_{1Q}$  DATA FOR EMERALDINE BASE AT AMBIENT  
 TEMPERATURE



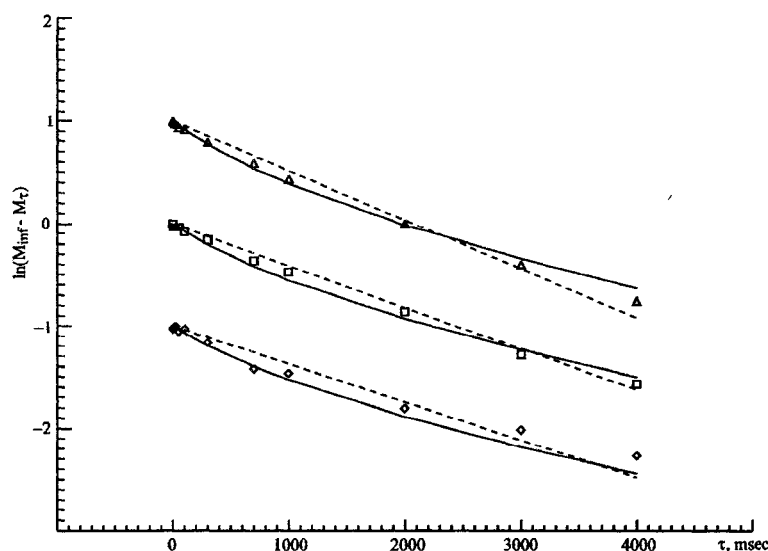
Unconstrained bi-exponential fit for experimental (triangles) and EXPRESS simulated (solid lines)  $T_{1Z}$  (A and C) and  $T_{1Q}$  (B and D) data for emeraldine base at ambient temperature. EXPRESS simulations are done for the model of unevenly populated jumps in a cone with rate  $k_{lib} = 2.5 \times 10^9 \text{ s}^{-1}$  (A and B) and  $k_{lib} = 3 \times 10^5 \text{ s}^{-1}$  (C and D). Other relevant parameters for this model are discussed in Chapter 4.5. Error bars are shown only for the fit to the experimental data and reflect the bi-exponential formalism not the experimental scatter (see <sup>57</sup>).

These distributions are normal on the “log” scale, and therefore skewed, with tails toward higher rates, on the linear scale. The form of the distribution is

$$G(k_i) = \frac{\exp\left(-\frac{1}{2}\left(\frac{\log_{10}(k_i) - \log_{10}(k_{mp})}{\sigma}\right)^2\right)}{\sum_{i=0}^{n-1} \exp\left(-\frac{1}{2}\left(\frac{\log_{10}(k_i) - \log_{10}(k_{mp})}{\sigma}\right)^2\right)} \quad [6.2]$$

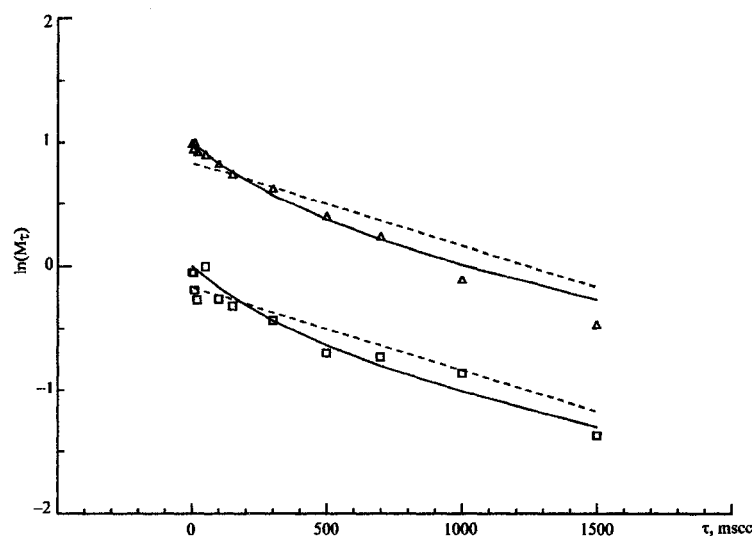
FIGURE 6.5

EXPERIMENTAL AND EXPRESS SIMULATED  $T_{1Z}$  RECOVERY CURVES FOR EMERALDINE BASE FOR FREQUENCIES HIGHER THAN  $\pm 64$  kHz



Experimental (symbols) and EXPRESS simulated (solid lines)  $T_{1Z}$  recovery curves for emeraldine base. Triangles correspond to a 64.21 kHz slice, squares to 69.09 kHz, and diamonds to 73.97 kHz. Dashed lines correspond to a single exponential  $T_{1Z}$  recovery for four-site cone model with parameters listed in Table 4.2 and rate  $k_{lib} = 3 \times 10^5 \text{ s}^{-1}$ . Solid lines are constrained multi-exponential recovery curves with  $\sigma = 0.5$  and  $k_{mp} = 3 \times 10^5 \text{ s}^{-1}$  (see text for explanation).

FIGURE 6.6  
 EXPERIMENTAL AND EXPRESS SIMULATED  $T_{1\rho}$  RECOVERY CURVES FOR  
 EMERALDINE BASE



Experimental (symbols) and EXPRESS simulated (solid lines)  $T_{1\rho}$  recovery curves for emeraldine base. Triangles correspond to a 69.09 kHz slice, squares to 71.53 kHz. Dashed lines correspond to a single exponential  $T_{1\rho}$  recovery for four-site cone model with parameters listed in Table 4.2 and rate  $k_{lib} = 3 \times 10^5 \text{ s}^{-1}$ . Solid lines are constrained multi-exponential recovery curves with  $\sigma = 0.5$  and  $k_{mp} = 3 \times 10^5 \text{ s}^{-1}$  (see text for explanation).

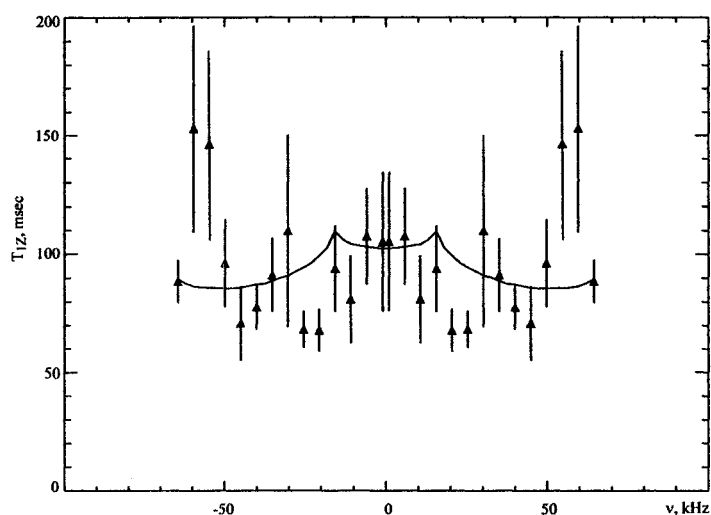
where  $k_{mp}$  is the most probable rate. For each rate,  $k_i$ , the simulated spectrum has to be normalized to unit integrated intensity before multiplying by the corresponding weight  $G(k_i)$ . Then the total spectrum is calculated as a sum of sub-spectra for  $n$  values of  $k_i$

sampled from the distribution  $I(\nu) = \sum_{i=0}^{n-1} I(\nu, k_i) G(k_i)$ . According to the log-normal

distribution, the most probable rate is always less than the average rate,  $\langle k \rangle = \sum k_i G(k_i)$ .

The solid lines in Figure 6.5 represent EXPRESS fits with five rates ( $n = 5$ ) sampled from a log-normal distribution with  $\sigma = 0.5$ , and the  $k_{mp}$  is the same as  $k_{lib}$  for the “dashed” fits.

FIGURE 6.7  
UNCONSTRAINED BI-EXPONENTIAL FIT TO EXPERIMENTAL AND EXPRESS  
SIMULATED FAST RELAXING  $T_{1Z}$  COMPONENT OF EMERALDINE BASE AT  
AMBIENT TEMPERATURE



Unconstrained bi-exponential fit to experimental (triangles) and EXPRESS simulated (solid lines) fast relaxing  $T_{1Z}$  component of emeraldine base at ambient temperature. EXPRESS simulations are done for the model of fast two-site  $\pi$ -flips of phenyl rings with rate  $k_{flip} = 1.5 \times 10^{10} \text{ s}^{-1}$ . Other relevant parameters for this model are discussed in Table 4.1. Error bars are shown only for the fit to the experimental data and reflect the bi-exponential formalism more than experimental scatter (see <sup>57</sup>).

$T_{1Q}$  data are known to be more sensitive to the presence of the rate distribution and slow motion <sup>60,81</sup>. The fit of  $T_{1Q}$  anisotropy to the model of two-exponential decay is oversimplification, which can explain overall discrepancies observed in Figure 6.4 (D). In

Figure 6.6, experimental (symbols) and simulated  $T_{1Q}$  recovery curves are compared at two frequencies outside the region of fast flippers. The use of log-normal rate distribution (solid lines) improves the fit dramatically as compared to single exponential decay (dashed lines). The fit parameters are identical to those used for the  $T_{1Z}$  anisotropy (see figure caption).

The experimental  $T_{1Z}$  value of the fast component from the bi-exponential fit is illustrated in Figure 6.7. The small integrated intensity (3%) of fast flipping rings and overlapping anisotropies from both powder patterns at frequencies  $|\nu| < 65$  kHz greatly complicate the analysis. Even though the maximum intensity of the flipping component is high in this frequency region, a noticeable fraction of intensity still comes from rings undergoing small angle libration. Librational motion has relatively narrow rate distribution but nevertheless, changing the rate from  $k_{lib} = 1 \times 10^5 \text{ s}^{-1}$  to  $k_{lib} = 1 \times 10^6 \text{ s}^{-1}$  leads to approximate change of relaxation time from 6000 to 500 ms at 15 kHz.

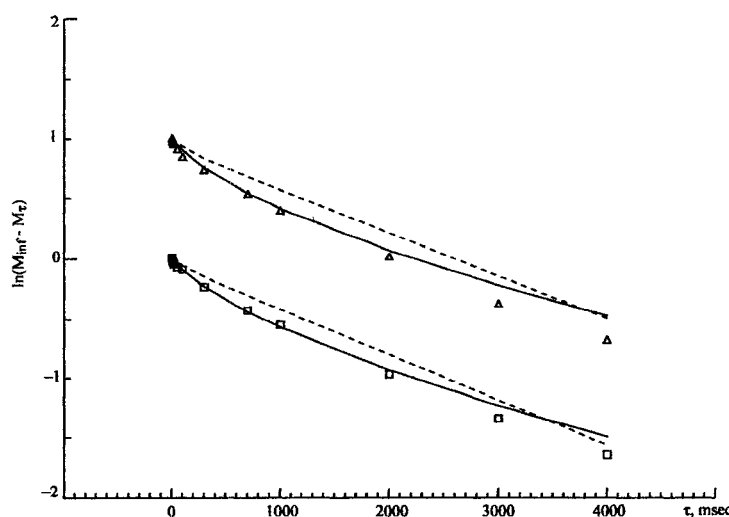
The fast component of the bi-exponential fit model yielded a flip rate  $k_{flip} = 1.5 \times 10^{10} \text{ s}^{-1}$  when the rest of the parameters were fixed from the lineshape simulations. But it is emphasized again that based on arguments above and the fact that  $T_{1Q}$  was not excited within the frequency range  $|\nu| < 30$  kHz, the parameters cannot be confirmed.

Experimental (symbols) and simulated (dashed and solid lines)  $T_{1Z}$  recovery curves for two frequencies within the spectral region  $|\nu| < 30$  kHz are shown in Figure 6.8. The dashed lines correspond to the bi-exponential  $T_{1Z}$  recovery, whose slow component (97%) was simulated with the four-site cone model with listed parameters (Table 4.2) and rate  $k_{lib} = 3 \times 10^5 \text{ s}^{-1}$ , and the fast component (3%) is simulated with  $180^\circ$  ring flips with the rate  $k_{flip} = 1.5 \times 10^{10} \text{ s}^{-1}$ . Solid lines reflect 97% slow and 3% fast

components as well, but also they incorporate the multi-exponential character of the slow cone librational motion with most probable rate  $k_{mp} = 3 \times 10^5 \text{ s}^{-1}$  and distribution width  $\sigma = 0.5$ , as was found for regions  $|\nu| > 64 \text{ kHz}$ . It is clear that within this frequency range, the bi-modal rate distribution is plausible, with some fraction of  $\pi$ -flipping rings having long relaxation times (see figure 6.8).

FIGURE 6.8

EXPERIMENTAL AND EXPRESS SIMULATED  $T_{1Z}$  RECOVERY CURVES FOR EMERALDINE BASE FOR FREQUENCIES LOWER THAN  $\pm 64 \text{ kHz}$



Experimental (symbols) and EXPRESS simulated (solid, dashed lines)  $T_{1Z}$  recovery curves for emeraldine base. Triangles correspond to a 15.38 kHz slice and squares to 34.9 kHz slice. Dashed lines correspond to the bi-exponential  $T_{1Z}$  recovery, with a slow component (97%) simulated using the four-site cone model with parameters (Table 4.2) and rate  $k_{lib} = 3 \times 10^5 \text{ s}^{-1}$ , and the fast component (3%) simulated with  $180^\circ$  ring flips with the rate  $k_{flip} = 1.5 \times 10^{10} \text{ s}^{-1}$ . Solid lines also reflect slow and fast components, as described above, but include a distribution of cone libration rates with most probable rate  $k_{mp} = 3 \times 10^5 \text{ s}^{-1}$  and rate distribution width  $\sigma = 0.5$ .

Based on acquired experimental data, it is impossible to analyze quantitatively the rate distribution for fast  $\pi$ -flippers. Adequate fit of relaxation anisotropies in this spectral range would require the presence of a larger fraction of  $180^\circ$  flippers, which might be achieved at higher temperatures. Qualitatively, recalling that MAS sidebands of emeraldine salt revealed two components with very different widths (which could correspond to two very different motional frequencies) and based on  $T_{1Z}$  recovery curve analysis, the distribution of flip rates could be very broad. This assumption agrees with data reported by Kaplan<sup>40</sup>. Slow  $180^\circ$  flips would yield powder patterns superimposable with those for the slow cone libration.

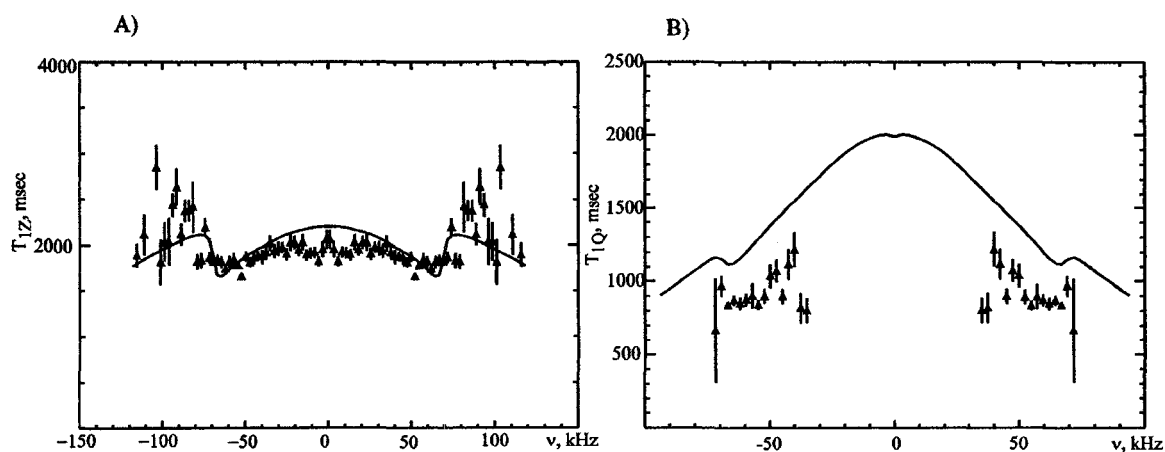
### 6.3 EMERALDINE HYDROCHLORIDE RELAXATION

For emeraldine hydrochloride the procedure of fitting relaxation data is further complicated by overlapping powder patterns from conductive and non-conductive regions of the sample. The conductive regions are heterogeneous and arise from crystalline domains, where conductivity is close to metallic, and amorphous matrix, which connects these domains and limits the conductivity. Furthermore, as was shown in the previous chapter, there are localized unpaired electrons in emeraldine salt samples. Electron-nuclear dipolar coupling will make the relaxation time of deuterons in close proximity to a polaron very short.

Applying the same approach, the bi-exponential procedure was used to find the best fit  $T_{1Z}$  and  $T_{1Q}$  relaxation rate anisotropies for the slow relaxing component.

FIGURE 6.9

UNCONSTRAINED BI-EXPONENTIAL FIT FOR EXPERIMENTAL AND EXPRESS  
SIMULATED  $T_{1Z}$  AND  $T_{1Q}$  DATA FOR EMERALDINE HYDROCHLORIDE AT  
AMBIENT TEMPERATURE

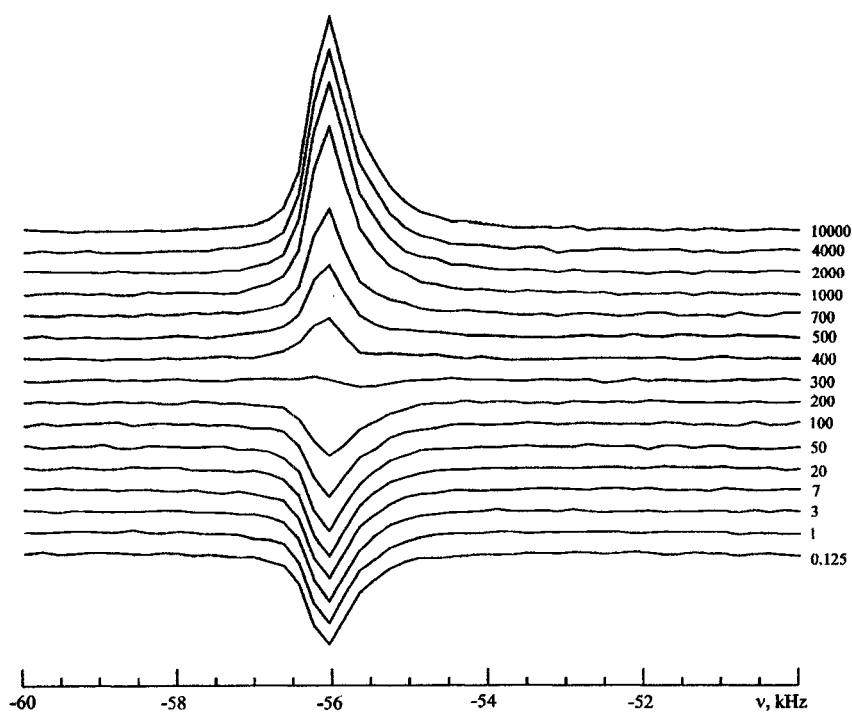


Unconstrained bi-exponential fit for experimental (triangles) and EXPRESS simulated (solid lines)  $T_{1Z}$  (A) and  $T_{1Q}$  (B) data for emeraldine hydrochloride at ambient temperature. EXPRESS simulations are done for the model of unevenly populated jumps in a cone with rate  $k_{lib} = 2.7 \times 10^5 \text{ s}^{-1}$ . Other relevant parameters for this model are listed in Table 4.2. Error bars are shown only for the fit to the experimental data and reflect the bi-exponential formalism.

Based on QE lineshape simulations (Chapter 4.5), only 1.5% of the intensity from fast  $\pi$ -flippers is observed for this material at this temperature, so that no reliable fit for this component can be expected. Figure 6.9 illustrates unconstrained bi-exponential fits (solid lines) of  $T_{1Z}$  and  $T_{1Q}$  orientation for the slow component. The model of unequally populated cone libration was used to calculate anisotropies.

A  $T_{1\rho}$  experiment was conducted for emeraldine salt sample at ambient temperature with magic angle spinning (Figure 6.10). Intensities of spinning sidebands at

FIGURE 6.10  
 REPRESENTATIVE SPINNING SIDEBAND OF EXPERIMENTAL MAS  
 INVERSION RECOVERY SPECTRA OF ES/CHI AT AMBIENT TEMPERATURE  
 AS A FUNCTION OF THE RELAXATION DELAY



Relaxation delay,  $\tau$ , for each partially relaxed spectrum is shown in milliseconds. The spinning speed was 8 kHz.

the top of each Gaussian component were analyzed as a function of relaxation delay  $\tau$ .

For the spinning sample, the spin-lattice relaxation rates were much faster than for static

samples. This is due to dipolar spin diffusion between orientationally unequivalent deuterium nuclei. Pines and coworkers showed<sup>82</sup> that in crystals containing both rapidly reorienting and rigid deuterons, spin diffusion tends to bring both types into internal equilibrium at a common spin temperature. However, in static a sample the dependence of quadrupole coupling on orientation in the external magnetic field quenches the spin diffusion and different deuterons relax at independent and widely different rates. For spin diffusion to be effective neighboring deuterons, which have different orientations of their principal axis system of the electric field gradient with respect to the static magnetic field, must fall at such an orientation in the lab frame where they have the same quadrupole splitting,  $\Omega_Q$  (see Equation 2.31). Only a negligible fraction of the deuterons will meet this condition. When sample is rotated about the magic angle, the quadrupole splitting of the deuterons is modulated harmonically. At some point during the rotation cycle the quadrupole splittings of the two deuterons must become equal and during this crossing spin diffusion occurs. The width of the crossing depends on the magnitude of the dipolar coupling between the crossing deuteron and steepness at which quadrupole splittings cross<sup>82</sup>.

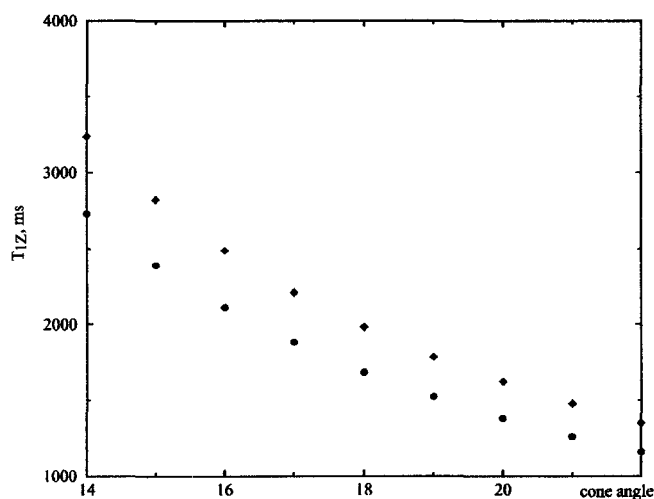
Since dipolar coupling is inversely proportional to the cube of the distance between nuclei (equation 2.32), one can safely assume that spin diffusion between deuterons in two distinct regions (conductive and non-conductive), observed for emeraldine hydrochloride, is negligible.

Within the non-conductive region, the experimental  $T_{1Z}$  relaxation time averages to  $737 \pm 181$  ms. One would expect this region of emeraldine salt sample be mostly amorphous and have a lot of defects such as, for example, localized charges. In static

samples only deuterons in close proximity to the charge are influenced, but if the sample rotates at high speed then magnetization flow by spin diffusion to these “sinks” becomes more effective. Moreover, the amorphous morphology of this part of the sample as well as the presence of  $Cl$  ions should lead to larger librational amplitudes than those for either emeraldine base or the partially crystalline, well ordered conductive regions. As

FIGURE 6.11

DEPENDENCE OF  $T_{1Z}$  RELAXATION TIME FROM LIBRATIONAL ANGLE FOR THE MODEL OF DISCRETE JUMPS IN A CONE



Simulated dependence of  $T_{1Z}$  relaxation time from librational angle at 62 kHz (diamond) and 40 kHz (circles), simulated (EXPRESS) for the model of discrete jumps in a cone with  $k_{lib} = 2.7 \times 10^5 \text{ s}^{-1}$ ,  $\omega_2 = 180 \text{ kHz}$ ,  $\eta_{PAS} = 0.043$ ,  $p_0 = 0.85$ ,  $p_1 = p_2 = p_3 = 0.05$  (see chapter 4.5).

illustrated in Figure 6.11, an increase in the librational amplitude leads to decrease of spin-lattice relaxation time. We believe that these two effects account for the

unexpectedly low  $T_{1Z}$  relaxation time in non-shifted component of the spinning ES/HCl sample.

Within the conductive region (shifted line), the average spin lattice relaxation time is  $T_{1Z} = 1481 \pm 132$  ms. For the charge to be delocalized effectively, the structure of emeraldine salt has to be close to ideal, so that one would expect less localized charge defects in this region. Consequently, effect of localized polarons on relaxation time can be neglected. Using data from bi-exponential deconvolution of the spin lattice relaxation time for static experiments, one can crudely estimate “averaged”  $T_{1Z}$  relaxation time for the spinning sample:

$$\left\langle \frac{1}{T_{1Z}} \right\rangle = c_f \cdot \frac{1}{T_{1z}^{(f)}} + c_s \cdot \frac{1}{T_{1z}^{(s)}} = 0.985 \cdot \frac{1}{T_{1z}^{(f)}} + 0.015 \cdot \frac{1}{T_{1z}^{(s)}} = 1556 \text{ms} \quad [6.3]$$

Here,  $c_f$  and  $c_s$  are fractions of fast and slowly relaxing components respectively. These fractions were determined from lineshape simulations (Table 4.2). The calculated value agrees well with the measured one within the experimental error.

In highly conducting PANI-CSA films, using  $^{13}\text{C}$  NMR Kolbert *et al.*<sup>33</sup> found a constant value  $T_1 T \sim 100$  s·K over a 200 degree temperature range. Using the formula<sup>41</sup> for the relaxation rate in organic conductors

$$\frac{1}{T_{1Z}^{\text{Korringa}} T} = \left( \frac{\Delta B}{B_0} \right)^2 \left( 1 + \frac{1}{2} \varepsilon \right) C_0 S_K \quad [6.4]$$

one can estimate Korringa-like contribution to relaxation rate in emeraldine hydrochloride. In this formula  $\left( \frac{\Delta B}{B_0} \right)$  is the Knight shift,  $S_K$  is Korringa scaling factor which takes into account the low dimensionality of the charge transport,

$C_0 = \frac{4\pi k}{\hbar} \cdot \left( \frac{\gamma_n}{\gamma_e} \right)^2$ ,  $\varepsilon = \frac{(a_{33} - a)^2}{a_{iso}^2}$  is the ratio of the square of anisotropic and isotropic

contributions to the hyperfine interaction, respectively (see equation 2.51). For classical metals  $\varepsilon = 0$  and  $S_K = 1$ , and the Korringa relation is recovered. In organic conductors, however, the anisotropic part is often important ( $0 < \varepsilon < 4$ ) and the scaling factor is  $50 < S_K < 500$ . Using Kolbert's estimate of the relevant parameters and correcting for the lower gyromagnetic ratio of deuterons, the 10-15 ppm  $^{13}\text{C}$  Knight shift in the conducting film would be consistent with a Korringa-like contribution to  $^2\text{H}$  relaxation in our sample with  $T_{1Z}^{(Korringa)} = 2.5 - 6$  s at 300 K. Since the observed rate is a sum of Korringa and quadrupole contributions, then

$$\frac{1}{T_{1Z}^{Quadrupole}} = \frac{1}{T_{1Z}^{obs}} - \frac{1}{T_{1Z}^{Korringa}} \quad [6.5]$$

Calculations show, that  $T_{1Z}^{Quadrupole} = 2.1 - 4.1$  s. This relaxation time agrees very well with one found for non-conductive emeraldine base.

## CHAPTER 7

### CONCLUSIONS

$^2\text{H}$  NMR results obtained in this study are summarized in this chapter, and their implications for charge transport properties of polyaniline are discussed.

Powder samples of ring deuterated emeraldine base and emeraldine hydrochloride have similar quadrupole echo spectra, which consist of a superposition of lineshapes for nearly rigid aromatic rings and a small fraction of rings which undergo fast  $180^\circ$  flips.

The fraction of rapidly flipping rings increases with temperature for both non-conductive (base) and conductive (salt) samples. Presumably, as the temperature rises, the free volume increases and rings can undergo  $\pi$ -flips more easily because they are less constrained by neighboring chains. At all temperatures EB has a larger fraction of fast flippers than ES/HCl. This can be attributed to several factors. Better packing in semicrystalline emeraldine hydrochloride reduces free volume in comparison to amorphous emeraldine base. In addition, local chain conformations in ES/HCl, which promote electron delocalization by increasing  $\pi$ -electron overlap, also produce increased

potential barriers for ring flips. Finally, ring flips may be sterically hindered by nearby bulky acid counter-ions.

Simultaneous measurements of quadrupole echo lineshapes and the orientation dependence of  $T_{1Z}$  and  $T_{1Q}$  anisotropies allowed an accurate description of motional models and parameters for polyanilines. Slow, small-angle libration in an asymmetric cone provided the best qualitative and quantitative description for the “rigid” fractions of EB and ES/HCl. A relatively narrow distribution of librational rates ( $\sigma = 0.5$ ) was adequate for the emeraldine base sample.

For the ES/HCl sample, the existence of two resolved signals in magic angle spinning spectra with different  $T_{1Z}$  relaxation rates is ascribed to microscopic domains with very different electrical properties. The unexpectedly short relaxation rate found for nonconductive domains in ES/HCl can be explained by the presence of localized, unpaired electrons there. In static samples only deuterons in close proximity to the electron spin are influenced, but if the sample rotates at high speed then magnetization flow by spin diffusion to these relaxation “sinks” becomes more effective. Moreover, the amorphous environment and the presence of  $Cl^-$  ions should lead to larger librational amplitudes than those for either emeraldine base or the partially crystalline, well ordered conductive regions of emeraldine salt. Larger librational amplitudes also lead to shorter relaxation rates.

Spin count experiments proved that in highly conductive emeraldine salt samples loss of NMR signal intensity occurs not only because of high rf reflectance but also because there is irreversible dephasing before signal acquisition. The latter can arise from dipolar interaction between deuterons and nearby unpaired electrons. Calculations show

that deuterons within about 3 Angstroms of an unpaired electron will be NMR-invisible in our deuteron experiments. There is no simple correlation between the degree of crystallinity as determined by X-ray powder diffraction and the fraction of missing NMR signal. Our results suggest that NMR is capable of detecting spins in both crystalline and non-crystalline regions, but unlike polyethylene and other nonconductive, partially crystalline polymers, these signals are not resolved in polyaniline.

Deuteron MAS spectra provided unique information about small shifts, which is obscured in QE spectra. Individual spinning sidebands of nonconductive emeraldine base can be fit by a weighted sum of two Gaussians with the same center frequency but different widths. The observation of two components in the MAS spectra of EB is attributed to different librational rates and/or amplitudes of benzoid and quinoid rings. Because of the low intensity of the wide Gaussian, ascribed to quinoid moieties, and consequently large uncertainties, a detailed analysis of its line width was not warranted. The combination of quadrupole echo,  $T_{1Z}$  and  $T_{1Q}$ , and  $^2\text{H}$  MAS techniques facilitates discrimination between two alternative explanations for the width of the other peak, associated with benzoid rings: it is due to slow librational motion on the spectral time scale.

Conductive emeraldine salts have an additional manifold of spinning sidebands, shifted approximately 5.7 ppm towards higher frequencies. These shifted sidebands originate from quasi-metallic regions of the sample, where deuteron spins interact with delocalized electrons (Knight shift). For all three salt samples studied, the frequency of the shifted peak is independent of temperature, while its intensity increases with increasing temperature and conductivity. The relative intensity of the shifted and

unshifted components provides an approximate measure of the fraction of repeat units associated with delocalized electronic states. In the ES/HCl sample, this amounts to 40-60% within the measured temperature range, while for the more highly conducting samples doped with CSA, the fraction approaches unity at ambient temperature.

The experimental temperature dependence of the intensity of the shifted peak can be explained using models developed for amorphous semiconductors. At low temperatures, because of the inhomogeneous morphology of the polymer, disorder-induced localization of charge carriers is dominant, which results in low intensity of the shifted peak. As temperature increases, phonon-induced delocalization and percolation among “conductive islands” occurs. Consequently, more deuteron spins are coupled with charge carriers, producing a more intense shifted peak. With improved polymer processing, samples with higher conductivity could have larger “metallic islands” and they could be located closer to each other. A lower temperature would be required to induce charge delocalization and the intensity of the shifted peak is expected to be higher at lower temperatures as compared to less conductive samples. This picture is strongly supported by our NMR results. The observation that at ambient temperature the highly conductive ES/CSA/NMP and ES/CSA/m-cresol films have most of the intensity in the shifted peak implies that the charge is delocalized over the entire sample. At the same time, the relatively small frequency magnitude of the Knight shift suggests that only a small fraction of the charge carriers is delocalized.

The unambiguous observation of a Knight shift has an important consequence for the theory of electrical conduction in polyaniline: it implies that polarons are the charge carriers.

## APPENDIX A

### MAS LINE SHAPE FITTING PROCEDURE

Lineshapes of the individual sidebands in MAS spectra of the Pani samples were fit to a weighted sum of test functions by minimizing  $\chi^2$ , defined as

$$\chi^2 = \sum_{i=1}^N \frac{1}{\sigma_i^2} \left\{ S(\nu_i) - \sum_{j=1}^M I_j f_j(\nu_i, \delta_j, \Delta_j) \right\}^2 \quad [\text{A.1}]$$

Here,  $S(\nu_i)$  is the measured signal intensity at frequency  $\nu_i$  and  $f_j(\nu_i, \delta_j, \Delta_j)$  is the  $j$ -th Gaussian (or Lorentzian) component, centered at frequency  $\delta_j$  with full width at half-maximum intensity  $\Delta_j$ . The experimental integrated signal intensity as well as the intensity of each component are normalized to unity,

$$\sum_{i=1}^N f_j(\nu_i, \delta_j, \Delta_j) = 1 \quad [\text{A.2}]$$

$$\sum_{i=1}^N S(\nu_i) = 1 \quad [\text{A.3}]$$

$$\sum_{j=1}^M I_j = 1 \quad [\text{A.4}]$$

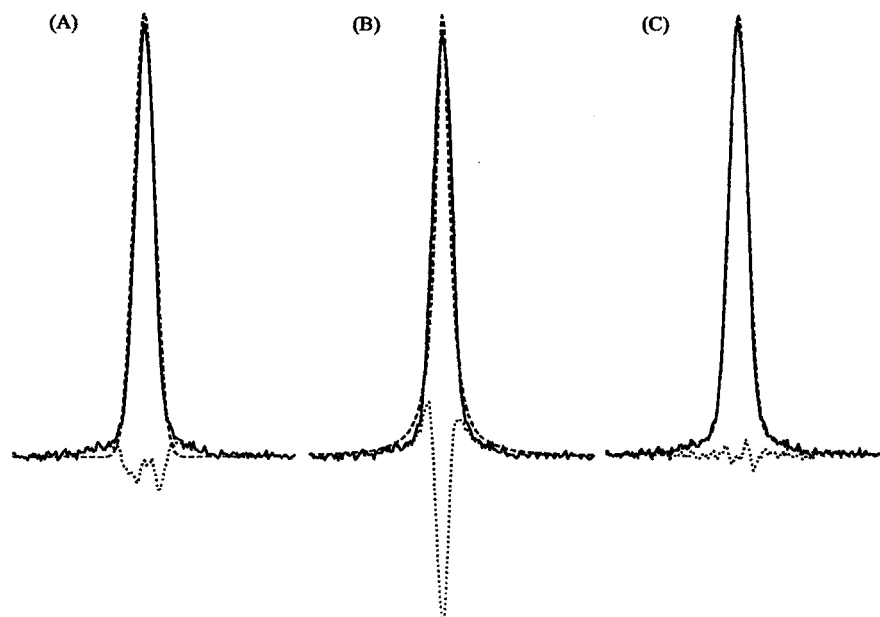
Thus, the relative weight of each  $f_j$  component is  $I_j$ . Fitting a sideband to a sum of three Gaussian functions, for example, requires that eight parameters be specified: three center frequencies, three line widths, and two relative intensities. The experimental uncertainty associated with  $S(\nu_i)$  is  $\sigma_i$ . In what follows, it is assumed that every point in the spectrum has the same absolute uncertainty, which was estimated from the noise level. With these definitions, the minimum value of  $\chi^2$  for an “acceptable” model should be on the order of  $N$ , the number of data points. Much larger values of  $\chi^2$  can be used to reject potential models, while smaller ones indicate an improper estimate of the experimental uncertainties<sup>83</sup>.

For EB and the Pani/Clay nanocomposite, fits to model functions consisting of a single Gaussian or Lorentzian function were compared with unconstrained, five parameter fits to a sum of two Gaussians. A typical visual comparison of fits to the different model functions for EB at 263 K is shown in Figure A.1.

The values of  $\chi^2$  summarized in Table A.1 show that two component fits are required for both samples, and relevant best fit parameters are listed in the main text. Error limits could be obtained as a byproduct of the Levenburg-Marquardt procedure used to minimize  $\chi^2$ , but the more realistic error limits listed in Tables 5.2 – 5.4 were obtained instead from the range of parameter values returned by independent fits to several sidebands in each spectrum.

FIGURE A.1

COMPARISON OF EXPERIMENTAL SPECTRUM OF A SPINNING SIDEBAND OF  
EMERALDINE BASE AT 263K WITH DIFFERENT FIT FUNCTIONS



Comparison of experimental spectrum (solid line) of a spinning sideband of EB at 263 K with different fit functions (dashed lines): Gaussian (A), Lorentzian (B), weighted sum of two Gaussians (C). The difference between experimental and calculated line shapes is represented by dotted lines.

For ES/HCl, a weighted sum of three Gaussians was required. However, the data are not of sufficient quality to permit an unconstrained fit to the eight parameters required for this model. Since the two Gaussians needed to fit EB were found to have the same center frequency, this constraint was applied to the first two Gaussians for ES/HCl. In addition, the fitting algorithm converged reliably only when an additional parameter was fixed,  $I_2 = 0.25 \times I_1$ . This resulted in only 6 adjustable parameters: the intensity  $I_1$  of a Gaussian function centered at frequency  $\delta_1$  with width  $\Delta_1$ , a second Gaussian at

frequency  $\delta_1 = \delta_2$ , and width  $\Delta_2$ , and a third Gaussian at frequency  $\delta_3$  with width  $\Delta_3$ . It is important to note that  $\delta_1$  frequency of the first Gaussian was found to be the same within  $\pm 10$  Hz as observed for the EB. Table 5.2 in the main text summarizes all the parameters determined for ES/HCl.

TABLE A.1  
CHI-SQUARE COMPARISON OF DIFFERENT MODEL FUNCTIONS FOR  
EMERALDINE BASE, EMERALDINE SALT AND PANI/MMT CLAY  
NANOCOMPOSITE AT 223K

Material	Model functions			
	Gaussian <sup>a</sup>	Two Gaussians <sup>a</sup>	Three Gaussians <sup>a</sup>	Lorentzian <sup>a</sup>
EB	12896	598	-	12555
ES/HCl	18695	352	231	3110
Pani / Clay	2965	299	-	734

<sup>a</sup> the number of points used in the fit was 151

## APPENDIX B

### T<sub>2</sub> CORRECTION FOR EMERALDINE HYDROCHLORIDE

The time origin of the MAS spectra is the top of the first rotational echo, and relative intensities determined by deconvolution of MAS sidebands are therefore affected by differential transverse relaxation during the first rotor period. As noted in the text, this is not a problem for emeraldine base, because the echo decay was well represented by one exponential (no differential relaxation). However, semilog plots of sideband intensity versus echo number for the emeraldine hydrochloride sample (not shown) revealed significant curvature. In principle, each of the Gaussian components needed to fit the ES/HCl line shape can decay at a different rate (or even a distribution of rates). However, since a single exponential sufficed to describe relaxation of both Gaussian components for EB, we assume here that only one more exponential is needed for ES/HCl.

First, a set of “ $T_2$ -relaxed” spectra was obtained by simple left shifts to the top of successive echoes. For each such spectrum, the line shape of a representative sideband was fit by unconstrained non-linear least squares to a sum of two Gaussian components. The fractional intensities of first and second Gaussians determined by fitting are denoted

by  $I_1^{obs}(n\tau_R)$  and  $I_2^{obs}(n\tau_R) = 1 - I_1^{obs}(n\tau_R)$  respectively, where  $n=1,2,3\dots$  is the echo number. Normalization gives

$$I_1(0)e^{-n\tau_R/T_2^{(1)}} + (1 - I_1(0))e^{-n\tau_R/T_2^{(2)}} = 1 \quad [\text{B.1}]$$

Here,  $T_2^{(1)}$  and  $T_2^{(2)}$  are the phenomenological transverse relaxation times of the first and second components, respectively, and  $I_1(0)$  is the true (integrated) intensity of the first Gaussian at  $t = 0$ . We note in passing that  $T_2$  defined in this fashion bears no simple relation to sideband line widths. The observed intensity of the first Gaussian component is then given by

$$I_1^{obs}(n\tau_R) = \frac{I_1(0)e^{-n\tau_R/T_2^{(1)}}}{I_1(0)e^{-n\tau_R/T_2^{(1)}} + (1 - I_1(0))e^{-n\tau_R/T_2^{(2)}}} \quad [\text{B.2}]$$

and hence,

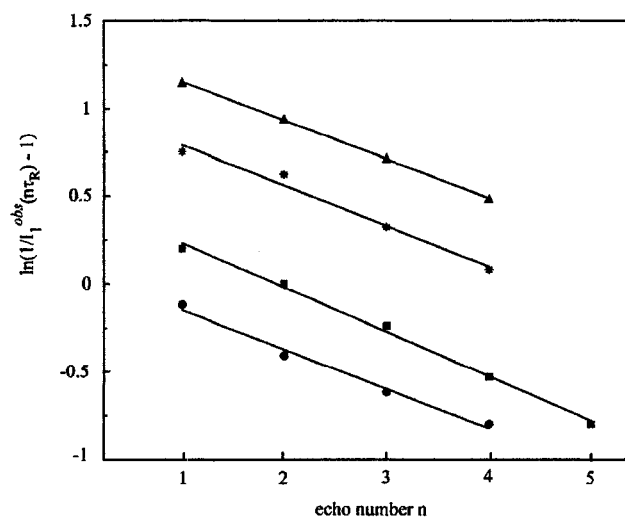
$$\left( \frac{1}{I_1^{obs}(n\tau_R)} - 1 \right) = \left( \frac{1}{I_1(0)} - 1 \right) e^{-n\tau_R \left( \frac{1}{T_2^{(2)}} - \frac{1}{T_2^{(1)}} \right)} \quad [\text{B.3}]$$

Thus, the intercept of a plot of  $\ln\left(\frac{1}{I_1^{obs}(n\tau_R)} - 1\right)$  verses echo number  $n$  yields the corrected intensity, while the slope gives the difference in relaxation rates. Application of this procedure to data for ES/HCl is illustrated in Figure B.1, with fit parameters listed in the figure caption.

The linearity of the plots at each temperature justifies the analysis in terms of just two exponentials. The relaxation time of the first Gaussian component,  $T_2^{(1)}$ , is on the order of 1 ms and that of the second component,  $T_2^{(2)}$ , is about 0.5 ms. It follows that the correction to fractional intensities arising from differential relaxation during the first 125  $\mu\text{s}$  rotor period is no more than about 5% and can be safely ignored.

FIGURE B.1

$T_2$  CORRECTION PLOT FOR EMERALDINE HYDROCHLORIDE FOR DIFFERENT TEMPERATURES



Symbols correspond to the following temperatures: 223 K (circles), 263 K (squares), 333 K (stars), 373 K (triangles). Solid lines are linear least square fits with parameters (intercept, slope) =  $(0.08 \pm 0.05, 1.80 \pm 0.48)$  at 223 K;  $(0.485 \pm 0.033, 2.02 \pm 0.08)$  at 263 K;  $(1.20 \pm 0.07, 1.85 \pm 0.19)$  at 333 K;  $(1.38 \pm 0.09, 1.79 \pm 0.03)$  at 373 K. Rotor period  $\tau_R = 125 \mu\text{s}$ .

## APPENDIX C

### DERIVATION OF CARTESIAN EFG TENSOR DEPENDENCE ON FAST 180° JUMP MOTION

Direct substitution of  $\beta_0 = 60^\circ$  and  $\eta_{PAS} = 0$  to Equation 4.5 yields that  $\langle \eta_M \rangle = -9$ .

Even though the formulas are correct, the averaged quadrupole parameters in the molecule fixed frame do not fit into convention, described in Chapter 2.2.2, where physical constraint on electric field gradient (EFG) tensor is  $0 \leq \eta \leq 1$ , when the following inequality is satisfied:

$$|V_{zz}| \geq |V_{yy}| \geq |V_{xx}| \quad [C.1]$$

The best way to understand which component of the tensor (Eq. C.1) is the biggest, is to consider active rotation between the coordinate frames in Cartesian form. According to the rule of transformation <sup>46</sup>

$$A_{NEW} = R(\alpha, \beta, \gamma) A_{OLD} R^{-1}(\alpha, \beta, \gamma) \quad [C.2]$$

where  $R(\alpha, \beta, \gamma)$  are Euler orthogonal matrices in Rose convention <sup>61</sup>, and  $R^{-1} = R^T$ . In the case of 180° jumps the transition from PAS to the molecule fixed frame is described by

$$R = R_z(\alpha)R_y(\beta) = \begin{pmatrix} \cos \alpha & -\sin \alpha & 0 \\ \sin \alpha & \cos \alpha & 0 \\ 0 & 0 & 1 \end{pmatrix} \begin{pmatrix} \cos \beta & 0 & \sin \beta \\ 0 & 1 & 0 \\ -\sin \beta & 0 & \cos \beta \end{pmatrix} \quad [\text{C.3}]$$

The components of Cartesian EFG tensor can be simplified if  $\eta_{PAS} = 0$

$$V_{PAS} = -\frac{V_{zz}}{2} \begin{pmatrix} 1 & 0 & 0 \\ 0 & 1 & 0 \\ 0 & 0 & -2 \end{pmatrix} \quad [\text{C.4}]$$

The Euler transformation according to the Eq. C.2 and averaging over equi-probable fast 180° jumps yields an expression for EFG tensor in the molecule fixed frame,

$$V_{MOL} = -\frac{V_{zz}}{2} \begin{pmatrix} -2 + 3 \cos^2 \beta & 0 & 0 \\ 0 & 1 & 0 \\ 0 & 0 & -3 \cos^2 \beta + 1 \end{pmatrix} \quad [\text{C.5}]$$

From the Eq. C.5 it follows that the motionally averaged  $z$ - axis of the PAS is now pointing along  $x$ -axis. Appropriate reassignment of axis gives  $\langle \eta_M \rangle = \frac{3}{5}$ .

## BIBLIOGRAPHY

- (1) Shirakawa, H.; Louis, E. J.; MacDiarmid, A. G.; Chiang, C. K.; Heeger, A. J. *Chemical Communications* **1977**, *1*, 578.
- (2) Chiang, C. K.; Fincher, C. R.; Park, Y. W.; Heeger, A. J.; Shirakawa, H.; Louis, E. J. *Phys. Rev. Lett.* **1977**, *39*, 1098.
- (3) MacDiarmid, A. G.; Epstein, A. J. *Mat. Res. Soc. Symp. Proc.* **1994**, *328*, 133-144.
- (4) Letheby, H. *J. Chem. Soc.* **1862**, *15*, 161.
- (5) Green, A. G.; Woodhead, A. E. *J. Chem. Soc. Trans* **1910**, *97*, 2388.
- (6) MacDiarmid, A. G. *Synthetic Metals* **1997**, *84*, 27-34.
- (7) Kumar, D.; Sharma, R. C. *Eur. Polym. J.* **1998**, *34*, 1053-1060.
- (8) Ray, A.; Asturias, G. E.; Kershner, D. L.; Richter, A. F.; MacDiarmid, A. G. *Synthetic Metals* **1989**, *29*, E141-E150.
- (9) Chiang, J. C.; MacDiarmid, A. G. *Synthetic Metals* **1986**, *13*, 193-205.
- (10) Ginder, J. M.; Richter, A. F.; MacDiarmid, A. G.; Epstein, A. J. *Solid State Communications* **1987**, *63*, 97-101.
- (11) Yang, C. Y.; Cao, Y.; Smith, P.; Heeger, A. J. *Synthetic Metals* **1993**, *53*, 293.

- (12) Cao, Y.; Smith, P.; Heeger, A. J. *Synthetic Metals* **1992**, *48*, 91 -97.
- (13) Pomfret, S. J.; Adams, P. N.; Monkman, A. P.; Comfort, N. P. *Synthetic Metals* **1999**, *101*, 724.
- (14) Roth, S.; Graupner, W. *Synthetic Metals* **1993**, *55-57*, 3623-3631.
- (15) Wessling, B. *Synthetic Metals* **1998**, *93*, 143-154.
- (16) MacDiarmid, A. G.; Epstein, A. J.; S.A. Jenekhe, K. J. W., Ed.; ACS: Washington D.C., 1997; Vol. 672, pp 395-407.
- (17) Shim, Y.-B.; Stilwell, D. E.; Park, S.-M. *Electroanalysis* **1991**, *3*, 31-36.
- (18) Kaneto, K.; Kaneto, M.; Min, Y.; MacDiarmid, A. G. *Synthetic Metals* **1995**, *71*, 2211-2212.
- (19) Kohlman, R. S.; Zibold, A.; Tanner, D. B.; Ihas, G. G.; Ishiguro, T.; Min, Y. G.; MacDiarmid, A. G.; Epstein, A. J. *Physical Review Letters* **1997**, *78*, 3915-3918.
- (20) Mott, N. F.; Davis, E. A. *Electronic Processes on Non-Crystalline Materials*, Second ed.; Clarendon Press: Oxford, 1979.
- (21) Pouget, J. P.; Jozefowicz, M. E.; Epstein, A. J.; Tang, X.; MacDiarmid, A. G. *Macromolecules* **1991**, *24*, 779-789.
- (22) Pouget, J. P.; Laridjani, M.; Jozefowicz, M. E.; Epstein, A. J.; Scherr, E. M.; MacDiarmid, A. G. *Mat. Res. Soc. Symp. Proc.* **1992**, *247*, 589.
- (23) Laridjani, M.; Pouget, J. P.; Scherr, E. M.; MacDiarmid, A. G.; Jozefowicz, M. E.; Epstein, A. J. *Macromolecules* **1992**, *25*, 4106-4113.
- (24) Joo, J.; Long, S. M.; Pouget, J. P.; Oh, E. J.; MacDiarmid, A. G.; Epstein, A. J. *Physical Review B* **1998**, *57*, 9567 - 9580.

- (25) Zuo, F.; Angelopoulos, M.; MacDiarmid, A. G.; Epstein, A. J. *Physical Review B* **1987**, *36*, 3475.
- (26) Nakhmedov, E. P.; Prigodin, V. N.; Samukhin, A. N. *Sov. Phys. Solid State* **1988**, *31*, 368.
- (27) Mizoguchi, K.; Mechtschein, M.; Travers, J. P.; Menardo, C. *Phys. Rev. Lett.* **1989**, *63*, 66.
- (28) Epstein, A. J.; MacDiarmid, A. G.; Pouget, J. P. *Phys. Rev. Lett.* **1990**, *65*, 664.
- (29) Bredas, J. L.; Street, G. B. *Accounts of Chemical Research* **1985**, *18*, 309 - 315.
- (30) Zhuang, L.; Zhou, Q.; Lu, J. *Journal of Electroanalytical Chemistry* **2000**, *493*, 135-140.
- (31) Sariciftci, N. S.; Heeger, A. J.; Cao, Y. *Physical Review B* **1994**, *49*, 5988.
- (32) Kaplan, S.; Conwell, E. M.; Richter, A. F.; MacDiarmid, A. G. *Macromolecules* **1989**, *22*, 1669-1675.
- (33) Kolbert, A. C.; Caldarelli, S.; Thier, K. F.; Sariciftci, N. S.; Cao, Y.; Heeger, A. *J. Physics Review B* **1995**, *51*, 1541-1545.
- (34) Stein, P. C.; Hartzell, C. J.; Jorgensen, B. S.; Earl, W. L. *Synthetic Metals* **1989**, *29*, E297 - E302.
- (35) Richter, A. F.; Ray, A.; Ramanathan, K. V.; Manohar, S. K.; Furst, G. T.; Opella, S. J.; MacDiarmid, A. G.; Epstein, A. J. *Synthetic Metals* **1989**, *29*, E243-E249.
- (36) Beau, B.; Travers, J. P.; Banka, E. *Synthetic Metals* **1999**, *101*, 772-775.
- (37) Mabboux, P. Y.; Beau, B.; Travers, J. P.; Nicolau, Y. F. *Synthetic Metals* **1997**, *84*, 985-986.

- (38) Beau, B.; Travers, J. P.; Genoud, F.; Rannou, P. *Synthetic Metals* **1999**, *101*, 778-779.
- (39) Pavesi, L.; Tedoldi, F. *Polymers for Advanced Technologies* **1996**, *8*, 30-34.
- (40) Kaplan, S.; Conwell, E. M.; Richter, A. F.; MacDiarmid, A. G. *Synthetic Metals* **1989**, *29*, E235-E242.
- (41) Mehring, M.; Rachdi, F.; Zimmer, G. *Philosophical Magazine B* **1994**, *70*, 787-794.
- (42) Espe, M. P.; Mattes, B. R.; Schefer, J. *Macromolecules* **1997**, *30*, 6307 - 6312.
- (43) Levitt, M. *Spin Dynamics. Basics of Nuclear Magnetic Resonance*; John Wiley & Sons: West Sussex, England, 2001.
- (44) Weaver, C. E.; Pollard, L. D. *The Chemistry of Clay Minerals*; Elsevier Scientific Publishing Company: Amsterdam, New York, London, 1973; Vol. 15.
- (45) Slichter, C. P. *Principles of Magnetic Resonance*; Springer-Verlag: Berlin Heidelberg New York, 1978; Vol. 1.
- (46) Thompson, W. J. *Angular Momentum*; John Wiley & Sons, Inc.: New York, 1994.
- (47) Sakurai, J. J. *Modern Quantum Mechanics*; Addison-Wesley Publishing Co, Inc.: Redwood City, CA, 1985.
- (48) Steigel, A.; Spiess, H. W. *Dynamic NMR Spectroscopy*; Springer-Verlag: Berlin, 1978.
- (49) Brink, D. M.; Satchler, G. R. *Angular Momentum*, Third ed.; Oxford Science Publications: Oxford, 1993.
- (50) Abragam, A. *The Principles of Nuclear Magnetism*; Oxford University Press: Oxford, 1961.

- (51) Jackson, J. D. *Classical Electrodynamics*; John Wiley & Sons: New York, 1975.
- (52) Lide, D. R., Ed. *CRC Handbook of Chemistry and Physics*, 83rd ed.: Boca Raton London New York Washington, D.C., 2002-2003.
- (53) Poupko, R.; Vold, R. L.; Vold, R. R. *Journal of Magnetic Resonance* **1979**, *34*, 67-81.
- (54) Haeberlen, U. *High Resolution NMR in Solids, Selective Averaging.*; Academic Press: New York, 1976.
- (55) Kittel, C. *Introduction to Solid State Physics*, 7th ed.; John Wiley & Sons: New York, 1996.
- (56) Bloembergen, N. *Physica* **1954**, *20*, 1130.
- (57) Malyarenko, D. I. *Ph.D. Dissertation In Applied Science*; College of William & Mary: Williamsburg, 2001.
- (58) Waugh, J. S., Ed. *Advances in Magnetic Resonance*; Academic Press: New York and London, 1965; Vol. 1.
- (59) Vold, R. R.; Vold, R. L. *Adv. Magn. Opt. Reson.* Academic Press, 1991.
- (60) Tse, T. Y. *Ph.D. Dissertation In Physics*; College of William & Mary: Williamsburg, 1995.
- (61) Rose, M. E. *Elementary Theory of Angular Momentum*; John Wiley & Sons: New York, London, Sidney, 1957.
- (62) Wolf, D. *Spin-Temperature and Nuclear-Spin Relaxation in Matter*; Clarendon Press: Oxford, 1979.
- (63) Fedorchenko, A. M. *Theoretical Physics: Quantum Mechanics and Statistical Physics*; Vyscha shkola: Kiev, UA, 1993; Vol. 2.

- (64) Levy, R. A. *Principles of Solid State Physics*; Academic Press: New York and London, 1968.
- (65) G.E.Asturias; MacDiarmid, A. G. *Synthetic Metals* **1989**, *29*, E157 -E162.
- (66) Wu, Q.; Xue, Z.; Qi, Z.; Wang, F. *Polymer* **2000**, *41*, 2029-2032.
- (67) Pauw, L. J. v. d. *Philips Research Reports* **1958**, *13*, 1-9.
- (68) Marshall, A. G.; Verdun, F. R. *Fourier Transforms in NMR, Optical, and Mass Spectrometry*; Elsevier: Amsterdam-Oxford-New York -Tokyo, 1990.
- (69) Brown, M. J. *Ph.D. Dissertation In Physics*; College of William & Mary: Williamsburg, 1996.
- (70) Heaton, N. J.; Vold, R. R.; Vold, R. L. *Journal of Magnetic Resonance* **1988**, *77*, 572-576.
- (71) Wittebort, R. J. *Journal of Magnetic Resonance* **1989**, *83*, 626-629.
- (72) Spiess, H. W. *Colloid & Polymer Science* **1983**, *261*, 193-209.
- (73) Cholli, A. L.; Dumais, J. J.; Engel, A. K.; Jelinski, L. W. *Macromolecules* **1984**, *17*, 2399-2404.
- (74) Hoatson, G. L.; Vold, R. L. *NMR Basic Principles and Progress* **1994**, *32*, 1-61.
- (75) Usha, M. G.; Peticolas, W. L.; Wittebort, W. J. *Biochemistry* **1991**, *30*, 3955 - 3962.
- (76) Quillard, S.; Louarn, G.; Lefrant, S.; MacDiarmid, A. G. *Physical Review B* **1994**, *50*, 12496.
- (77) Kaplan, S.; Conwell, E. M.; Richter, A. F.; MacDiarmid, A. G. *J. Am. Chem. Soc.* **1988**, *110*, 7647-7651.

- (78) Terao, T.; Maeda, S.; Yamabe, T.; Akagi, K.; Shikarawa, H. *Solid State Communications* **1984**, *49*, 829 - 832.
- (79) Peo, M.; Forster, H.; Hocker, J.; Gardner, J. A.; Roth, S.; Dransfeld, K. *Solid State Communications* **1981**, *38*, 467 - 468.
- (80) Clarke, T. C.; Scott, J. C. *Solid State Communications* **1982**, *41*, 389 - 391.
- (81) Vold, R. L.; Hoatson, G. L.; Tse, T. Y. *Chem. Phys. Lett.* **1996**, *263*, 271.
- (82) Alla, M.; Eckman, R.; Pines, A. *Chemical Physics Letters* **1980**, *71*, 148 - 151.
- (83) Press, W. H.; Teukolsky, S. A.; Vetterling, W. T.; Flannery, B. P. *Numerical Recipes in C*, Second ed.; Cambridge University Press, 1992.

## VITA

Yanina Anatolievna Goddard

Yanina Anatolievna Goddard was born in Kiev, Ukraine on January 16, 1972. She graduated from Kiev High School # 145 in June 1989. Yanina Goddard received her Specialist Physicist (Teacher) degree at Kiev State Taras Shevchenko University in 1994. From September 1994, the author worked as a Research Associate in the Laboratory of Physics of Liquids at Kiev State Taras Shevchenko University.

In 1997, the author entered the graduate program at the College of William & Mary in the Department of Applied Science. She received M. S. in Applied Science in 1999 and completed Ph.D. program requirements under scientific supervision of Dr. Robert L. Vold in March 2004.